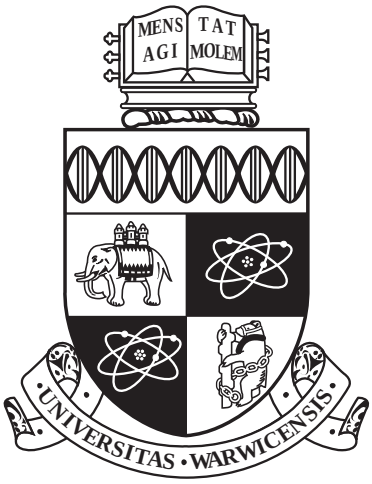

NANOSCALE INTERFACIAL FLOWS WITH THERMAL FLUCTUATIONS AND SLIP

by

Yixin Zhang

Thesis

Submitted to the University of Warwick

for the degree of

Doctor of Philosophy

School of Engineering

June 2021

THE UNIVERSITY OF
WARWICK

Contents

Acknowledgments **iv**

Declarations **v**

Abstract **vi**

List of Figures **vii**

Nomenclature **xii**

Chapter 1 Introduction **1**

1.1 Research background 1

1.2 Thesis overview 3

1.3 Published articles 4

Chapter 2 Literature review **5**

2.1 Thin-film flows 5

2.2 Thermal capillary waves 11

2.3 Liquid-solid slip 13

2.4 Summary of challenges 16

Chapter 3 Stochastic modelling of nanoscale interfacial flows **18**

3.1 Stochastic lubrications equations with slip 18

3.1.1 Thin films on plates 19

3.1.2 Thin films on fibres 25

3.2 Langevin equation: beyond the lubrication paradigm 28

3.2.1 Background: the Ornstein–Uhlenbeck process 29

3.2.2 Capillary wave theory 30

3.2.3 Langevin equation for thermal capillary waves 31

3.3 Summary 33

Chapter 4 Molecular dynamics simulations **34**
4.1 Foundations of MD simulations 35
4.1.1 Equations of motion 35
4.1.2 Intermolecular potentials 36
4.1.3 Thermostatting strategies 36
4.1.4 Boundary conditions in MD simulations 37
4.1.5 Calculating transport properties 37
4.2 Molecular models of liquid films and solid substrates 39
4.3 Extracting free-surface positions 41
4.4 Validation of Laplace pressure at the nanoscale 41
4.5 Summary 44

Chapter 5 Instability of nanofilms on plates **45**
5.1 Classical instability mechanism with disjoining pressure 45
5.2 New instability mechanism accounting for thermal fluctuations . . . 48
5.3 MD simulations of dewetting nanofilms 51
5.4 Results and discussions 54
5.5 Summary 57

Chapter 6 Thermal capillary wave growth and surface roughening **58**
6.1 Time-dependent TCW spectra 58
6.1.1 TCW spectra obtained from SLEs 58
6.1.2 TCW spectra from the Langevin model 59
6.2 MD simulations 60
6.2.1 Settings of films on slippery plates and fibres 60
6.2.2 Measurements of slip length 62
6.3 Results and discussions 64
6.3.1 Spectra of planar films 64
6.3.2 Roughness of planar films and their universality class 66
6.3.3 Spectra of annular films 70
6.3.4 Connections with experiments 72
6.4 Summary 74

Chapter 7 Anisotropic relaxation of capillary wave correlations **75**
7.1 MD simulations 75
7.1.1 Setup for films on anisotropic-slip substrates 75
7.1.2 Measurements of anisotropic slip length 77
7.2 Theoretical approach 78

7.2.1 Langevin model for TCW correlations 78
7.2.2 Anisotropic boundary condition and dispersion relation . . . 81
7.3 Results and Discussions 84
7.3.1 Transient growth of capillary wave spectra 84
7.3.2 Relaxation of capillary wave correlations with varying slip . . 86
7.3.3 Relaxation of capillary wave correlations with anisotropic slip 87
7.4 Summary 89

Chapter 8 Conclusion and future work **91**

Appendix A Simplification of the stochastic integral **95**

Appendix B Stokes dispersion relation for annular films with slip **97**

Appendix C Anisotropic dispersion relation for planar films **101**

Acknowledgments

First and foremost I would like to express my sincere gratitude to my supervisors, Prof. Duncan A. Lockerby and Dr. James E. Sprittles for their invaluable advice, continuous support, and patience during my PhD study. I would like to thank all the members in the MNF group including Dr. Chengxi Zhao, Dr. Livio Gibelli, Dr. Juan C. Padrino, Jacqueline Mifsud, Jingbang Liu, and more. It is their kind help and support that have made my study and life in the UK a wonderful time. My gratitude extends to the University of Warwick for the funding opportunity to undertake my studies. I would like to thank my friends including Lidong Liu, Zhenwen Hu, Wenyi Tang, Zeng Luo, Peng Jiang, and more for making my PhD life more colourful. Finally, I would like to express my gratitude to my family. Without their tremendous understanding and encouragement in the past few years, it would be impossible for me to complete my study.

Declarations

This thesis is submitted to the University of Warwick in support of my application for the degree of Doctor of Philosophy. It has been composed by myself and has not been submitted in any previous application for any degree.

Abstract

In this thesis, we present theoretical studies and molecular dynamics (MD) simulations of nanoscale interfacial flows taking the crucial effects of thermal fluctuations and slip into account.

Adopting a long-wave approximation to Fluctuating Hydrodynamics, we derive stochastic lubrication equations (SLEs) for planar films and annular films with slip modelled. It is found that Navier's slip condition has to be modified by including a random stress at the boundary and relating its covariance with slip.

This 'long-wave' paradigm used to derive the SLEs has the inherent problem of being inaccurate for dynamics of interfacial waves with short wavelengths. We thus propose a Langevin equation to overcome this inadequacy, based on the Ornstein-Uhlenbeck process and classic Capillary Wave Theory (CWT).

Using the SLE, we investigate the effects of thermal fluctuations on the instability of dewetting nanofilms. A linear stability analysis of the SLE allows us to derive a power spectrum for the surface waves, which is quantitatively validated against the spectrum observed in MD. Thermal fluctuations are shown to be critical to the instability of nanoscale films. Compared to the classical instability mechanism, which is driven by disjoining pressure, fluctuations (a) massively amplify the instability, (b) create a time-dependent fastest growing wavenumber, and (c) increase the critical wavenumber so that classically stable films can be ruptured.

The proposed Langevin model can describe both the growth of capillary wave spectra and the relaxation of capillary wave correlations, with the former providing a time scale for the surface to reach thermal equilibrium. The capillary spectra of planar films are found to advance towards a static spectrum described by CWT, with the roughness of the surface W increasing as a power law of time $W \sim t^{1/8}$ before saturation. However, the spectra of an annular film (with outer radius h_0) are unbounded for dimensionless wavenumber $qh_0 < 1$ due to the Rayleigh-Plateau instability. Slip is shown to accelerate the growth of spectra for both kinds of films.

Temporal correlations of interfacial Fourier modes for nanofilms on anisotropic-slip substrates, measured at thermal equilibrium in MD, demonstrate that (i) larger slip lengths lead to a faster decay in wave correlations, and (ii) unlike on isotropic-slip substrates, the time correlations of waves on anisotropic-slip substrates are wave-direction dependent. These findings can be well predicted by the Langevin model with a newly derived dispersion relation considering the anisotropic-slip condition.

List of Figures

1.1 (a) Fluctuating contact lines in a liquid bridge between the two solid plates simulated in MD simulations. Reproduced from [1]. (b) Breakup of nanojets simulated by MD simulations, LE (deterministic lubrication equation) and SLE (stochastic lubrication equation). Reproduced from [3]. 2

2.1 A comparison of thin-film experiments and numerical solutions of LEs. (a) Dewetting of a thin film on a plate. The top panel shows experimental results and the bottom panel shows simulations of the Planar-film LE, reproduced from [4]; (b) Falling of an annular film down a fibre. Experimental results (left) compared to simulations of the Annular-film LE (right); reproduced from [21]. 6

2.2 Three kinds of dewetting mechanisms and the corresponding dewettng patterns. Reproduced from [43]. 7

2.3 Fourier transforms of the surface of dewetting films in two independent experiments. The y-axis in both figures represent the amplitude of surface modes. (a) Reproduced from [35]; (b) Reproduced from [44]. 8

2.4 A comparison of numerical solutions to the Planar-film SLE (Red line) and LE (Blue line) starting with the same initial condition. Reproduced from [46]. 8

2.5 A comparison of experimental spectra (symbols) and analytical spectra (solid-red lines). (a) spectra at early time with a small correlation length. (b) spectra at later time with a large correlation length. Reproduced from [46]. 9

2.6 Time-lapse TEM images showing ionic liquid flowing along two SnO_2 nanowires, reproduced from [34]. 10

2.7 (a) TCWs and roughness on ultra-low surface tension interface. Subfigures are arranged with decreasing surface tension from top to bottom, reproduced from [2]. (b) Decay of the temporal correlations of TCWs for three different wavenumers [55]. 11
2.8 (a) The propagation of wetting fronts in paper [63]. (b) The morphology growth of a bacterial colony [63]. (c) The prediction of surface roughness at increasing time. Before the transition time t_s, the roughness grows as a power-law; it saturates after t_s as a result of the interplay between deterministic and stochastic forces. 13
2.9 (a) Slip length as a function of contact angle [67]. (b) Slip length as a function of shear rates [68]. 15

3.1 Sketch of a liquid film on a plate, where $h = h(x,t)$ is the film thickness, λ is the characteristic length, u is the $x-$component of liquid velocity and ℓ is the liquid-solid slip length. The film has depth L_y in the y direction (into the page). 19
3.2 Sketch of an annular liquid film on a fibre, where $h = h(z,t)$ is the outer radius of the film, λ is the characteristic length and a is the fibre radius. 25

4.1 (a) The meaning of periodic boundary conditions; (b) The meaning of the reflective wall condition. 37
4.2 MD systems to obtain transport properties. (a) a cubic box of liquid for the measurement of viscosity; (b) a bulk of liquid with two free surfaces for the measurement of surface tension. 38
4.3 (a) the decay of the correlation of shear stress; (b) the distribution of $2\psi_{zz} - \psi_{xx} - \psi_{yy}$. 38
4.4 Snapshots of the $\langle 100 \rangle$ and $\langle 110 \rangle$ substrate surface in MD simulations. (a) perspective and top views of the $\langle 100 \rangle$ surface; (b) perspective and top views of the $\langle 110 \rangle$ surface. The light blue color indicates solid atoms in the second layer. 40
4.5 Two kinds of fibres. (a) Fibre 1, cut out from a bulk of platinum with a fcc structure. (b) Fibre 2, consisting of two concentric surfaces. . . 41
4.6 The extraction of the free surface, (a) for planar films and (b) for annular films. The dots are particles and the solid lines are the extracted interface. 42
4.7 Liquid bridges between two plates, (a) $\varepsilon_{ls} = 0.65\varepsilon_{ll}$, (b) $\varepsilon_{ls} = 0.35\varepsilon_{ll}$, (c) $\varepsilon_{ls} = 0.20\varepsilon_{ll}$. 42

4.8 Liquid cylinders on plates simulated in MD simulates (on the left panel) and the extractions of contact angles by fitting the surface shape with a circle (on the right panel), (a) $\varepsilon_{ls} = 0.65\varepsilon_{ll}$, (b) $\varepsilon_{ls} = 0.35\varepsilon_{ll}$, (c) $\varepsilon_{ls} = 0.20\varepsilon_{ll}$. 43

5.1 A sketch of the molecule-substrate interaction. The molecule is located at $(x = 0, y = 0, z = 0)$ and the semi-finite substrate (the shadow area) is located at $z = D$. Image taken from [103]. 46
5.2 Snapshots of a section of a thin liquid film on a substrate simulated in MD; (a) initial configuration, (b) undulation growth, and (c) rupture. L_x is the film length and h is the film thickness (y is into the page). 51
5.3 Spectra of MD simulations (dashed lines) and Eq. (5.29) (solid lines) at different times for (a) h_0=1.18 nm (t =0.086, 0.171, 0.428 ns); (b) h_0=1.57 nm (t =0.086, 0.257, 0.852 ns); and (c) h_0=1.96 nm (t =0.086, 0.857, 3.428 ns). The inset shows the deterministic spectrum for h_0=1.18 nm. 53
5.4 Dominant wavenumber as a function of time for (a) $h_0 = 1.18$ nm, (b) $h_0 = 1.57$ nm, (c) $h_0 = 1.96$ nm. Solid red lines are from the SLE, Eq. (5.29)). Triangular symbols are MD data and dashed black lines are from the deterministic LE, Eq. (5.6). t_r is the film rupture time when first dry-spot appears on the solid, averaged over a number of realisations (70, 50 and 30 times for cases (a)-(c)). 55
5.5 Rupture of three short films with their lengths inside classic critical wavelength λ_c in MD simulations (a) h_0=1.18 nm, (b) h_0=1.57 nm, (c) h_0=1.96 nm. 56

6.1 Snapshots of a thin liquid film (a section) on a substrate in MD. For planar films, (a) initial configuration with a smooth surface; (b) surface roughening. For annular films, (c) initial configuration; (d) beads formed due to the Rayleigh-Plateau instability. Two types of cylindrical substrates are used: (e) Fibre 1, cut out from a bulk of Platinum with fcc structure. (f) Fibre 2, consisting of two concentric surfaces. L_x is the film length, h is the film thickness for a planar film and film radius for an annular film, and a is the fibre radius (y and θ are into the page). 61

6.2 Slip length measured using pressure-driven flows. Figures (a-b) are for planar films with (a) for case P2 and (b) for case P1 and P3. MD calculations of velocity (triangles) are fitted with analytical solutions (black solid lines) with the HB (z_1) at the first valley of MD density (yellow solid line) and FS (z_2) at $0.5n_l^*$. The inset shows slip length as a function of driving force. Figure (c) is for annular films, case A1 and A2. The inset shows the density profile. 63
6.3 Evolution of capillary spectra of a (long) planar film for increasing slip length. A comparison of spectra extracted from MD results (triangles), and Langevin model with Stokes-flow dispersion relation (solid lines) or with long-wave dispersion relation (dash lines) at four different times, along with the static spectrum (dash-dot line). (a) $\ell = 0.68$ nm, (b) $\ell = 3.16$ nm, (c) $\ell = 8.77$ nm. The effective thickness of the film $h_0 = 2.90$ nm and film length is 313.9 nm. 65
6.4 Decrease of the dominant wavenumber as a function of time. 67
6.5 Slip effects on surface roughening of a planar film. The comparison is made among MD results (symbols), Langevin model with Stokes-flow dispersion relation (solid lines) or with long-wave dispersion relation (dash lines). 68
6.6 A complete evolution of the capillary spectra to the static spectrum. The film length is 62.78 nm. 69
6.7 Evolution of capillary spectra for annular films; a comparison between MD results (triangles), the static spectrum (dashed and dotted line) and the Langevin model. Dispersion relations used in the Langevin model assuming Stokes flow (solid lines) and a long-wave approximation (dashed lines). Slip lengths (a) Fibre 1, $\ell = 0$; and (b) Fibre 2, $\ell = 1.18$ nm. The hydrodynamic boundary is at radius $a = 2.60$ nm and the initial surface at $h_0 = 5.74$ nm (see sec.6.2 for measurement details). 70
6.8 Variation of the dispersion relation as a function of a/h_0. The lager a/h_0 means thinner films compared to the fibre radius. 71
6.9 Slip effects on surface roughening of a dewetting planar film. A comparison is made between our Langevin model and previous experiments [52] of a rupturing film without slip but with effects of disjoining pressure. A further experiment with large slip is suggested. . . . 72

7.1 Snapshots of the set-up of a liquid film on a substrate in MD simulation. (a) A perspective view of the whole system. The fluid atoms are orange and the solid atoms are navy blue. The free surface generated by post-processing is coloured olive green. (b) Top view and perspective view of the isotropic $\langle 100 \rangle$ substrate surface. (c) Top and perspective view of the anisotropic $\langle 110 \rangle$ substrate surface. The red dash lines in (b) and (c) denotes the lines of symmetry and the light blue color indicates solid atoms in the second layer. 76

7.2 Slip length measured using a pressure-driven flow past a plate. MD velocity (triangles) are fitted with analytical solutions (olive solid lines) with the HB (z_1) at the first valley of MD density (orange solid line) and FS (z_2) at $0.5n_l^*$. The tangent line (blue dash lines) gives the slip length ℓ^*. (a) the measurement is done for the isotropic $\langle 100 \rangle$ surface; (b) the measurement is done for the anisotropic $\langle 110 \rangle$ surface. 77

7.3 Capillary wave growth for case $C_{\langle 100 \rangle, 2}$. MD spectra after averaging over azimuthal directions are shown by triangles, with different color represents varying time. The analytical solutions are given by solid lines. The inset shows the 2D spectra from the 2D Fourier transform of the free surface at $t = 0.86$ ns. 85

7.4 Effects of varying slip length on temporal correlations of thermal capillary waves. MD results (different symbols) are compared with the analytical solutions Eq. (7.13) (solid lines). Wave vectors are represented by $\boldsymbol{q} = (q_x, q_y) = \frac{2\pi}{L}(n_x, n_y)$, where (n_x, n_y) are pairwise integers, and without loss of generality, we consider waves in the x-direction due to the isotropy. 86

7.5 Effects of anisotropic slip on temporal correlations of thermal capillary waves. MD results (symbols) are compared with analytical solutions (solid lines). Figure (a) and (c) are for the $\langle 100 \rangle$ surface, and figure (b) and (d) are for the $\langle 110 \rangle$ surface. Wave vectors are represented by $(q_x, q_y) = \frac{2\pi}{L}(n_x, n_y)$ where (n_x, n_y) are pairwise integers. 87

7.6 Relaxation time as a function of wavenumbers. MD results (symbols) are compared with analytical solutions (solid lines). 88

B.1 Sketch of a liquid film on a fibre 97

Nomenclature

$\boldsymbol{\tau}$	Three-dimensional random/stochastic stress tensor
$\boldsymbol{\vartheta}$	Hydrodynamic stress tensor
ℓ	Slip length
η	Friction factor
γ	Surface tension
λ	Characteristic film length
λ_c	Critical wavelength
λ_d	Dominant wavelength
μ	Dynamic viscosity
Ω ,ω	Dispersion relation
ϕ	Disjoining pressure
ρ	Mass density
σ	Distance parameter in LJ potential
ε	Energy parameter in LJ potential
A	Hamaker constant
h	Film height
k_B	Boltzmann constant
L	Film length
N	White noise

n_l	Number density of liquid
n_s	Number density of solid
q_c	Critical wavenumber
q_d	Dominant wavenumber
$R_{h_q h_q^*}$	Normalised temporal correlation
S_s	Static spectrum
T	Temperature
t_r	Rupture time
t_s	Transition time
CNT	Carbon nanotube
CWT	Capillary wave theory
fcc	Face centred cubic
FH	Fluctuating hydrodynamics
HB	Hydrodynamic boundary
LE	Lubrication equation
LJ	Lennard-Jones potential
LW	Long wave
MD	Molecular dynamics
NS	Navier-Stokes
OU	Ornstein-Uhlenbeck process
SLE	Stochastic lubrication equation
TCW	Thermal capillary wave

Chapter 1

Introduction

1.1 Research background

The emergence of microfluidic and nanofluidic technologies has focused attention on the nature of liquid flows at the nanoscale. These flows can often behave in a manner that is qualitatively different from those at the macroscale. One important difference is the breakdown of the deterministic description at the nanoscale and the increasingly dominant role of thermal fluctuations of liquid molecules. For example, at the nanoscale, the position of a contact line in equilibrium is not fixed, as deterministic models predict, but instead fluctuates with a Gaussian probability distribution (see Fig. 1.1(a)) [1]; the free surface of a liquid film at rest is not flat, but instead fluctuates due to thermal capillary waves [2]; the breakup of liquid nanojets in molecular dynamics simulations (MD) shows a double-cone rupture profile, in contrast to the long-thread profile predicted by deterministic equations (see Fig. 1.1(b)) [3]; and, deterministic models fail to accurately predict the rupture time of a dewetting polymer nanofilm [4, 5].

Stochastic modelling is thus essential to capture nanoscale flow physics, and broadly there are two options: a model based on Langevin theory or one based on fluctuating hydrodynamics (FH). Langevin theory is based on fluctuation-dissipation theorem and its applications to stochastic modelling include Brownian motion, single-file water transport in carbon nanotubes (CNT) [6], fluctuating contact lines [1, 7], fluctuating contact angles [8], and more. The equations of FH proposed by Landau and Liftshiz [9] are stochastic versions of the Navier-Stokes (NS) equations, with thermal fluctuations modelled by an additional random stress tensor. The applications of FH include the study of fluctuations in a dilute gas [10], fluctuations in diffusively mixing fluids [11], and the rupture of nanoscale liquid jets

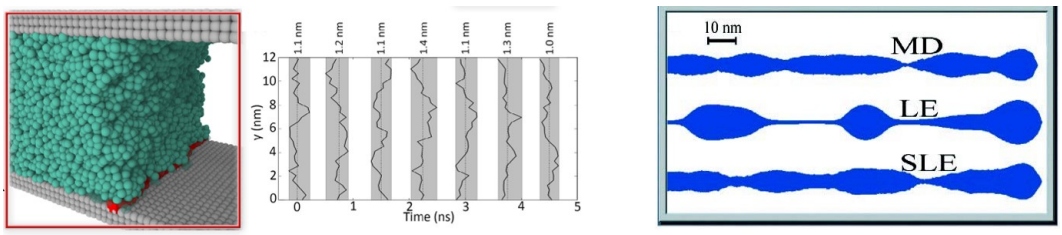

(a) (b)

Figure 1.1: (a) Fluctuating contact lines in a liquid bridge between the two solid plates simulated in MD simulations. Reproduced from [1]. (b) Breakup of nanojets simulated by MD simulations, LE (deterministic lubrication equation) and SLE (stochastic lubrication equation). Reproduced from [3].

and films [3, 5].

Another aspect that makes nanoscale flows differ from macroscale flows is the breakdown of the no-slip condition, and the greater importance of slip effects on flows. For instance, the fast water transport inside CNTs, which is far beyond the predictions of no-slip hydrodynamics, can be attributed to slip at the water-carbon interface [12]. This flow-rate enhancement makes CNTs promising membrane materials for ultrafiltration devices [13, 14]. Thus, incorporating slip condition is key to describing nanoscale flows correctly.

Interfacial flows (in our case, flows involving free surfaces) are commonly encountered at the nanoscale, such as in nanojets [3], nanofilms [4], nanobubbles and nanodroplets [15], with a host of applications in modern technologies, such as nanoprinting and nanocoating [16]. It is of broad interest to investigate the mutual effects of thermal fluctuations and liquid-solid slip on nanoscale interfacial flows, but this remains a challenge, posing difficult questions about how to model them correctly.

This thesis seeks to develop new theories to describe nanoscale interfacial flows with thermal fluctuations and liquid-solid slip, based on the FH equations and Langevin theory. The developed new theories are then used to study the instability of nanofilms on substrates and dynamics of thermal capillary waves. Understanding the instability mechanism of nanofilms is important for preventing film rupture during nanocoating. Studying the dynamics of thermal capillary waves is helpful for establishing a non-invasive technique to measure the properties of soft matter or biological fluids that can be sensitive to external forces.

So far, experimental studies on the effects of thermal fluctuations on nanoscale interfacial flows have been limited due to the technical difficulties associated with

the spatio-temporal scale. As such, MD simulations are a convenient tool to validate all new theories developed, and they are used throughout this thesis.

1.2 Thesis overview

This thesis has the following structure:

- **Chapter 2** gives a literature review of thin-film flows (with or without thermal fluctuations), thermal capillary waves (TCWs), and liquid-solid slip. We outline how thermal fluctuations are modelled in thin-film flows and thermal capillary waves in literature, and the challenges faced in simultaneously considering thermal fluctuations and slip .

- **Chapter 3** develops the new theories used in this thesis. Starting with FH equations, the stochastic lubrication equations (SLE) with slip effects are derived for nanoscale films on both planar and cylindrical substrates (Planar-film SLE and Annular-film SLE, respectively), using a long-wave approximation to FH equations. Knowing that the assumption of long waves may be inaccurate for the dynamics of interfacial waves with short wavelengths, a Langevin model is developed based on the Ornstein-Uhlenbeck process and classic Capillary Wave Theory that overcomes this inadequacy.

- **Chapter 4** introduces the foundations of molecular dynamics (MD) simulations for the general reader. Then, the MD models of liquid films and substrates (plates and fibres in geometry), which are used throughout this thesis to validate new theories, are presented. We also present the method used to extract free-surface positions from MD simulations, and validate the formula of Laplace pressure at the nanoscale.

- **Chapter 5** studies the effects of thermal fluctuations on the instability of nanofilms lying on planar substrates, using MD simulations and the Planar-film SLE developed in Chapter 3. We repeat the classical linear stability analysis of the deterministic Planar-film LE, in which disjoining pressure is thought to be the cause of the dewetting of nanofilms. We then conduct a linear stability analysis of the Planar-film SLE and derive a surface spectrum to reveal the effects of thermal fluctuations on the nanofilm instability. MD simulations of nanofilm dewetting are performed and compared with the surface spectrum derived from the Planar-film SLE.

- **Chapter 6** discusses the evolution of TCW spectra for nanofilms on plates and fibres with initially smooth surfaces. Time-dependent capillary spectra are obtained from the SLEs and Langevin model, which are then compared with MD simulations. Scaling relations are used to analyse the surface roughening of nanofilms on plates. Slip effects on the capillary spectra and surface roughening are also discussed.

- **Chapter 7** investigates the relaxation of TCW correlations on an anisotropic-slip substrate. We discuss how the surface anisotropy modifies the Navier's slip boundary condition. A new dispersion relation for Stokes flow with the anisotropic-slip boundary condition is derived. This dispersion relation is then built into the Langevin model to predict the results from MD simulations of TCWs on anisotropic-slip substrates. We also discuss the applicability of using TCWs to measure anisotropic slip in experiments.

- **Chapter 8** is the concluding chapter of this thesis. We summarise our findings and outline future directions in this chapter.

1.3 Published articles

1. Yixin Zhang, James E. Sprittles, and Duncan A. Lockerby, Molecular simulation of thin liquid films: Thermal fluctuations and instability, Physical Review E 100.2 (2019): 023108. (Editor's suggestion)

2. Yixin Zhang, James E. Sprittles, and Duncan A. Lockerby, Nanoscale thin-film flows with thermal fluctuations and slip, Physical Review E 102.5 (2020): 053105.

3. Yixin Zhang, James E. Sprittles, and Duncan A. Lockerby, Thermal capillary wave growth and surface roughening of nanoscale liquid films, Journal of Fluid Mechanics, 2021, 915.

4. Yixin Zhang, Duncan A. Lockerby, James E. Sprittles, Relaxation of thermal capillary waves for nanoscale liquid films on anisotropic-slip substrates, Langmuir, accepted.

Chapter 2

Literature review

This chapter gives a literature review of two kinds of important and extensively studied interfacial phenomena: thin-film flows (Sec. 2.1) and thermal capillary waves (Sec. 2.2). As both phenomena will involve liquid-solid boundaries in this thesis, the recent advances in the understanding of nanoscale slip is also discussed (Sec. 2.3).

2.1 Thin-film flows

Thin liquid films are ubiquitous in a variety of settings such as lava flows, tear films in the eye, foam films, falling water threads from a tap, and coating layers of a fibre or plate [17].

They are characterised by disparities of length scale in different dimensions, i.e. the ratio of film width to film length is very small: $\epsilon = h/\lambda \ll 1$. This allows the adoption of a long-wave approximation to derive lubrication equations (LE) from the full NS equations, reducing the dimensionality of the problem. In terms of macroscopic thin-film flows, which are well studied, deterministic LEs have been developed from NS: for liquid jets (which we here refer to as the 'Jet LE') to study their breakup [18]; for planar liquid films on plates (the 'Planar-film LE') [17], which has important applications in dewetting of polymer films [4, 19], as shown in Fig. 2.1(a); and for an annular liquid film on a fibre (the 'Annular-film LE') [20–23], which is used to predict the surface morphologies of falling liquid films down a fibre [20, 21] and the dynamics of fibre coating [22, 23], as shown in Fig. 2.1(b). LEs are much simpler to solve than the NS, and can be easily extended to consider many interesting effects, such as electric field forces [24, 25], Marangoni stresses [26, 27] and evaporation [28].

The instability of thin liquid films has been extensively studied using those

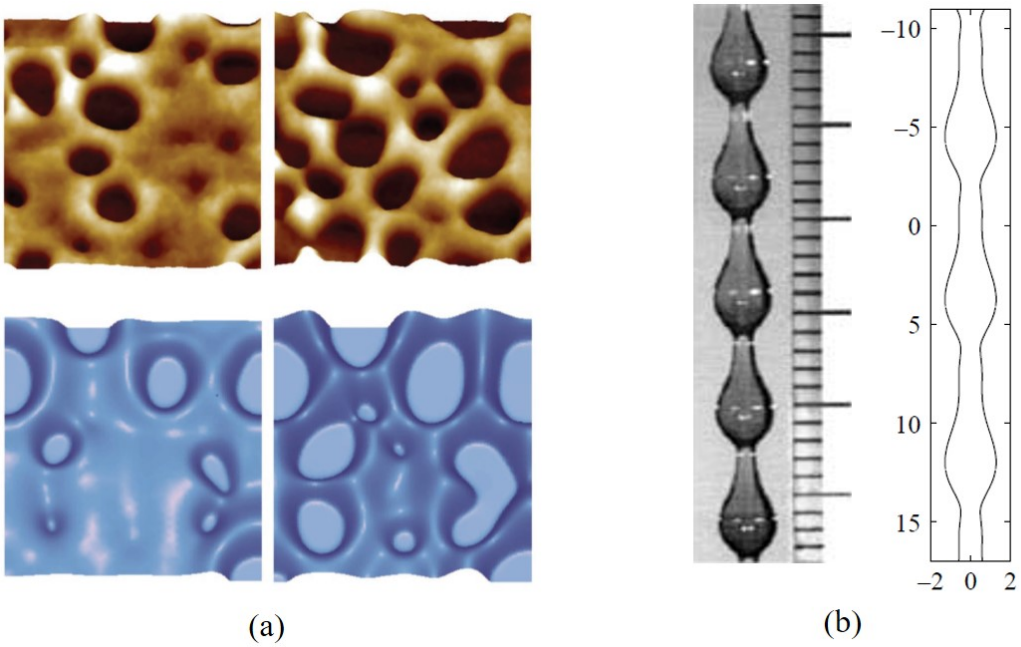

Figure 2.1: A comparison of thin-film experiments and numerical solutions of LEs. (a) Dewetting of a thin film on a plate. The top panel shows experimental results and the bottom panel shows simulations of the Planar-film LE, reproduced from [4]; (b) Falling of an annular film down a fibre. Experimental results (left) compared to simulations of the Annular-film LE (right); reproduced from [21].

LEs. In some circumstances, the instability of films needs to be prevented, such as when coating a fibre or a plate. In other situations, the instability of films is exploited, such as in recently-developed printing technology that relies on the rupture of thin liquid threads [29]. In either case, understanding the instability mechanisms is necessary for making accurate predictions.

The instability of liquid jets or annular films around fibres is due to the well-known Rayleigh-Plateau instability, where the destabilising surface tension force from the circumferential curvature competes with the stabilising surface tension force from the axial curvature, as described by the equations of Jet LE [18] and Annular-film LE [21].

In contrast, the spontaneous dewetting of thin liquid films (< 100 nm) deposited on planar substrates is considerably more complicated, but the study of the responsible instabilities is of broad engineering interest due to a myriad of applications in coatings [30, 31], lubricants [32], chemical sensors [33] and microfluidics [34]. Dewetting experiments of polymeric [35–39] and metal films [40] have revealed three different instability mechanisms [41]: spinodal dewetting due to the

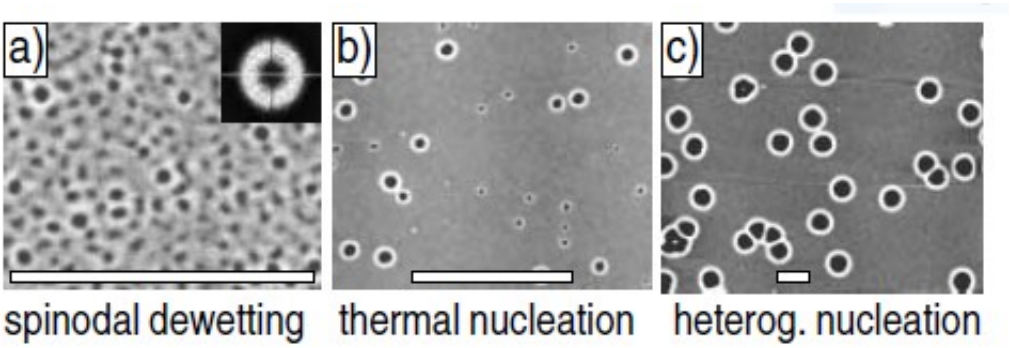

Figure 2.2: Three kinds of dewetting mechanisms and the corresponding dewettng patterns. Reproduced from [43].

undulation growth by disjoining pressure; thermal nucleation of random holes; and heterogeneous nucleation around defects. Varying dewetting mechanisms lead to different dewetting patterns, which are shown in Fig. 2.2. While the rupture of a film can be influenced by all three modes simultaneously [42], the breakup of relatively thin films, where the disjoining pressure is strong, is dominated by the spinodal dewetting mode [35–38]. In this regime, thermal roughness can be amplified by the disjoining pressure, but in competition with the restoring force of surface tension, such that only disturbances above a critical wavelength (λ_c) grow. This can be determined by a linear stability analysis of the Planar-film LE. A dominant wavelength (λ_d), which grows fastest, is also obtained from the linear analysis and it is often used to estimate the rupture time and the number of holes/drops after film rupture [41].

The presence of unstable modes can be used as an indication that spinodal dewetting is the primary dewetting mechanism for a particular liquid film [35, 39, 40, 42], which can be investigated by Fourier transforms of free-surface profiles. For example, Xie *et al.* [35] studied the dewetting of polystyrene films on a silicon substrate with varying thickness. The radially averaged interfacial Fourier modes for films with thickness < 10 nm indeed show that the critical wavenumber q_c ($= 2\pi/\lambda_c$) and dominant wavenumber q_d ($= 2\pi/\lambda_d$) exist (see Fig. 2.3(a)), indicating that the dewetting is spinodal dewetting. Similar observations were also reported in other dewetting experiments of thin films [44] shown in Fig. 2.3(b).

These experimental studies appeared to suggest that the deterministic Planar-film LE is accurate enough to predict the dewetting of nanofilms. However, although the dewetting pattern in experiments performed in [4] agrees with numerical solutions to the LE (see Fig. 2.1(a)), a quantitative analysis of the dewetting time showed that the results from experiments were much faster than the predictions of

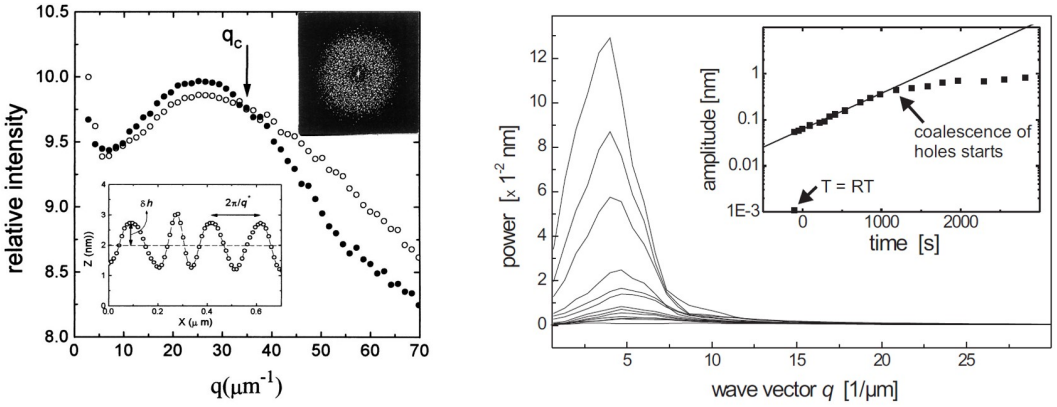

(a) (b)

Figure 2.3: Fourier transforms of the surface of dewetting films in two independent experiments. The y-axis in both figures represent the amplitude of surface modes. (a) Reproduced from [35]; (b) Reproduced from [44].

the Planar-film LE. As dewetting is often observed for films at the nanoscale, one can expect that thermal fluctuations will influence the dewetting. However, pending a theoretical breakthrough in stochastic modelling of interfacial flows using a long-wave approximation to Fluctuating Hydrodynamics (FH) equations, little progress has been made to understand the effects of thermal fluctuations.

Moseler and Landman [3] were pioneers in deriving a stochastic lubrication equation (SLE) from FH using a long-wave approximation. They proposed an SLE for nanojets (the 'Jet SLE') that is able to predict the double-cone rupture profile observed in MD, unlike the deterministic Jet LE (see Fig. 1.1(b)). Later, based on the Jet SLE, Eggers [45] confirmed that thermal noise leads to a symmetric self-similar rupture profile and thermal fluctuations speed up the rupture.

Similarly, Grün *et al.* [5] derived a SLE for planar liquid films on substrates

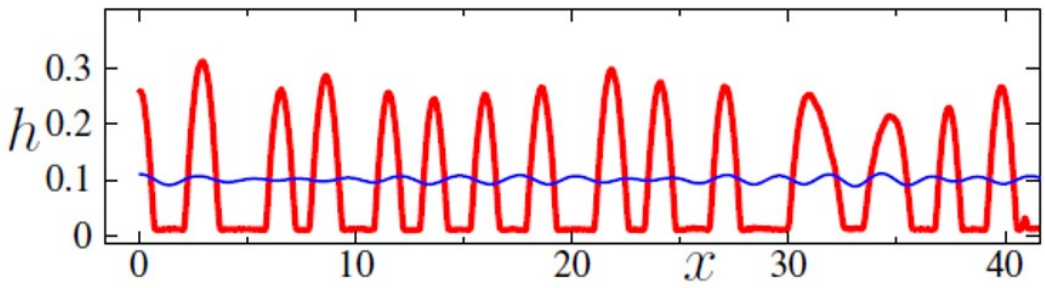

Figure 2.4: A comparison of numerical solutions to the Planar-film SLE (Red line) and LE (Blue line) starting with the same initial condition. Reproduced from [46].

(the 'Planar-film SLE') able to reconcile the aforementioned discrepancy in dewetting time between experiments [4] and solutions to the Planar-film LE. Independently, Davidovitch *et al.* [47] derived the same Planar-film SLE but in a study of nanodroplet spreading where thermal fluctuations are shown to enhance the spreading. The rupture of thin films has subsequently been widely investigated by numerical solutions to the Planar-film SLE [5, 46, 48–50], showing thermal fluctuations do indeed speed up the instability growth. For example, in Fig. 2.4, droplets have already formed after film dewetting from the results of the SLE (red line) but perturbations only start to grow from the results of the LE (blue line) [46].

These numerical solutions to the Planar-film SLE are able to focus on the effects of thermal fluctuations on the rupture of nanofilms, which is at the nonlinear stage of instability of nanofilms. To consider the effects of thermal fluctuations on the linear stability of nanofilms, Mecke and Rauscher [51] analytically derived a spectrum for the surface waves using the Planar-film SLE, and showed that noise can shift the spectrum from exhibiting an exponential to a power law decay with increasing wavenumbers for large wave vectors. This finding was later investigated in experiments on the dewetting of thin polymer films [52]. However, due to experimental limitations, a direct comparison between the theoretical and the experimental spectrum could not be made. Diez *et al.* [48] considered the noise to be spatially correlated and found that to produce close agreement between their theoretical spectrum and experimental data for metal films, different correlation lengths for the non-white noise had to be employed, as shown in Figs. 2.5 (a) and (b), where symbols are experimental results and solid red lines are the analytical solutions. The

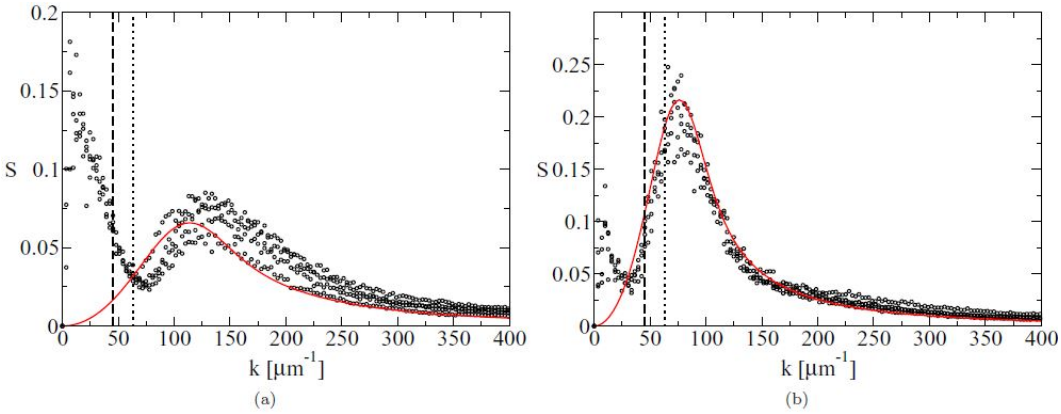

Figure 2.5: A comparison of experimental spectra (symbols) and analytical spectra (solid-red lines). (a) spectra at early time with a small correlation length. (b) spectra at later time with a large correlation length. Reproduced from [46].

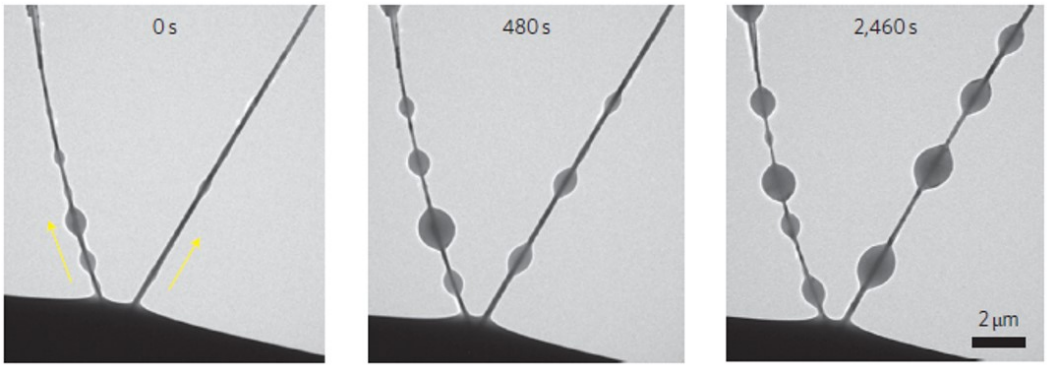

Figure 2.6: Time-lapse TEM images showing ionic liquid flowing along two SnO_2 nanowires, reproduced from [34].

spectra in Figs. 2.5 (a) are obtained at an early time with a small correlation length while the spectra in Figs. 2.5 (b) are at a later time with a large correlation length.

So far, experimental studies on the effects of thermal fluctuations on thin-film flows are extremely limited due to the technical difficulties associated with the spatio-temporal scale. As thermal fluctuations are inherent in MD simulations, they are useful tools to improve our understanding of the effects of thermal fluctuations on thin-film instability. For example, recently Zhao *et al.* [53] derived a spectrum for surface waves of a nanojet using the Jet SLE and found good agreement with MD simulations. In this thesis (Chapter 5), we conduct MD simulations of the dewetting of liquid films on substrates, and focus on the influence of thermal fluctuations on the initiation of instability by comparing the spectra from MD simulations directly with the analytical spectra with or without thermal fluctuations. This allows us to reveal how thermal fluctuations change the classical instability mechanism such as the critical and dominant wavenumbers.

Both the existing Jet SLE and Planar-film SLE can be viewed as extensions of the Jet LE and Planar-film LE with an additional, appropriately-scaled, noise term. However, an extension of the Annular-film LE to a stochastic version (an 'Annular-film SLE') is performed for the first time in this thesis. An analysis of this geometry is timely, being driven by state-of-the-art applications, such as, the use of nanofibres to transport annular films of liquids [34] (see Fig. 2.6) and the manufacture of ultra-smooth optical fibres [54].

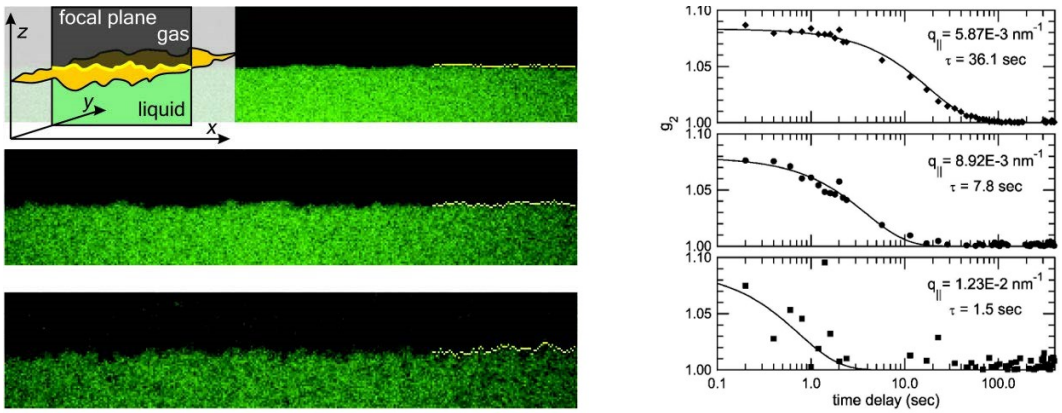

(a) (b)

Figure 2.7: (a) TCWs and roughness on ultra-low surface tension interface. Subfigures are arranged with decreasing surface tension from top to bottom, reproduced from [2]. (b) Decay of the temporal correlations of TCWs for three different wavenumers [55].

2.2 Thermal capillary waves

A well developed topic of nanoscale interfacial flows with thermal fluctuations is thermal capillary waves (TCWs), which lead to the roughness of the free surface of a liquid film at rest. The roughness created by TCWs is usually on the scale of nanometres, but it has also been observed optically at the microscale in ultra-low surface tension mixtures [2], as shown in Fig. 2.7(a).

Traditionally, research in TCWs has been strongly focused on the analysis of their equilibrium states. The classical theory that describes the equilibrium state of TCWs is called as Capillary Wave Theory (CWT), which, from the equipartition theorem, provides the mean amplitude of each surface mode as a function of wavenumber (q). For a planar film, the r.m.s. spectral density is given by:

$$\left\langle \left| \widehat{\delta h}(q,t) \right| \right\rangle \propto \frac{\sqrt{k_B T/\gamma}}{q}\,, \tag{2.1}$$

where $\widehat{\delta h}$ is the Fourier transform of height deviations varying with time t, k_B is the Boltzmann constant, T is temperature, and γ is the surface tension. The $\langle \cdots \rangle$ denotes an ensemble average over time when the free surface is in thermal equilibrium, and $|\cdots|$ the norm of the transformed variable. The $\sqrt{k_B T/\gamma}$ defines a length parameter which is known as the thermal length scale. The root-mean-squared roughness W of the film is related directly to the capillary wave spectrum Eq. (2.1) by Parseval's theorem. For a d-dimensional surface ($d = 1, 2$) with a lateral

size L, the root mean squared roughness is

$$W = \sqrt{\frac{1}{L^d}\langle \int (\delta h)^2 d^d\boldsymbol{x}\rangle} = \sqrt{\frac{1}{(2\pi)^d L^d}\int \langle |\widehat{\delta h}|^2\rangle d^d\boldsymbol{q}}. \tag{2.2}$$

A substitution of Eq. (2.1) into Eq. (2.2) leads to the expression for W, and one can find that a smaller surface tension leads to a larger roughness as validated in Fig. 2.7(a). The CWT expressed by Eq. (2.1) is also widely used to explain the structure of a liquid-vapour interface [56, 57] in the field of chemical physics.

In thermal equilibrium, it is well known that the temporal correlations of surface modes show an exponential decay, with a decay rate given by the dispersion relation of the system $\Omega(q)$ [58]. The temporal correlations of TCWs are thus given by:

$$\left\langle \widehat{\delta h}(q,t)\widehat{\delta h}^*(q,t')\right\rangle \propto \frac{k_B T}{\gamma q^2} e^{-\Omega(q)|t-t'|}, \tag{2.3}$$

where the asterisk denotes a conjugate value. Based on this, x-ray photon correlation spectroscopy (XPCS) or similar techniques, can be used to infer the features of liquid-solid systems such as surface tension, viscoelasticity, and substrate surface structures [55, 59–61]. For example, Kim *et al.* demonstrated that the temporal correlations of TCWs on polymer films decay with time using XPCS (see Fig. 2.7(b)), and by fitting the experimental results with Eq. (2.3), the viscosity of polymer films can be obtained (the viscosity is the fitting parameter in the dispersion relation) in agreement with other independent measurements [55]. This technique has the advantage of being non-invasive since no external forces are applied, which is crucial for soft matter and biological fluids that can be sensitive to external forces.

Importantly, Eq. (2.1) has no time dependence; it cannot reveal the evolution of a non-equilibrium surface to its thermal equilibrium, such as how a smooth surface develops to a rough one, or how sudden changes in material parameters generate evolution towards new spectra – as such, we refer to it as the *static spectrum*. Understanding dynamics is also essential as it allows prediction of the time required for a smooth film to reach its static spectrum, thus determining when the adoption of classical CWT is valid.

In fact, studying non-equilibrium surfaces and their transition to the equilibrium states is of broad interest, since surface roughening due to randomness is ubiquitous in nature, and a problem spanning many disciplines, such as, in the propagation of wetting fronts in porous media (see Fig. 2.8(a)), in the growth of bacterial colonies (see Fig. 2.8(b)), and in atomic deposition during the manufacture of computer chips [62].

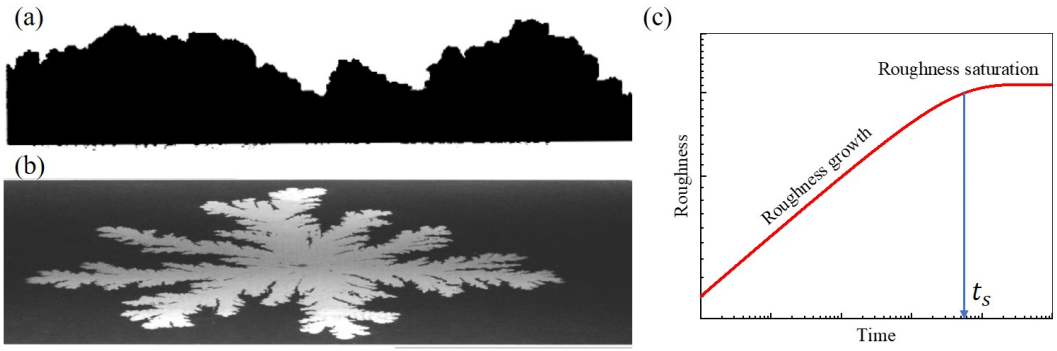

Figure 2.8: (a) The propagation of wetting fronts in paper [63]. (b) The morphology growth of a bacterial colony [63]. (c) The prediction of surface roughness at increasing time. Before the transition time t_s, the roughness grows as a power-law; it saturates after t_s as a result of the interplay between deterministic and stochastic forces.

To allow us to predict and control surface roughening, it is essential to understand how surface morphology develops in time, something usually described by scaling relations [62, 63]. The roughness W is expected to grow as a power law of time ($W \sim t^{\kappa}$) before reaching the saturated roughness W_s, which is a power law of domain length L ($W_s \sim L^m$). The transition of growth and saturation happens at the transition time t_s, which is also a power law of domain length ($t_s \sim L^{\alpha}$). Figure 2.8(c) provides examples of the appearance of this kind of surface roughening.

The three exponents (κ, m, α) define a universality class to connect different physical phenomena which belong to the same universality class. Thus, it is exciting to see whether a universality class exists for the surface roughening of a liquid film where the roughness is due to TCWs.

For the aforementioned dynamic problems, it is natural to seek solutions to SLEs discussed in Sec. 2.2. Indeed, linear stability analyses of the SLEs have provided time-dependent spectra of TCWs for both jets and planar films [51–53, 64]. However, despite their success, the long-wave approximation inherent in each of these SLEs creates restrictions on the wavelengths that can be accurately predicted, which requires the development of a more general method, and this is attempted using the Langevin theory in this thesis.

2.3 Liquid-solid slip

NS or FH equations require boundary conditions at the substrate surface to describe flows. At the nanoscale, the no-slip condition breaks down and slip effects become

important. For example, the fast water transport inside CNTs, which is far beyond the predictions of no-slip hydrodynamics, can be attributed to slip at the water-carbon interface [12].

Navier's slip condition, which describes the scalar proportionality between the slip velocity u_s and shear stress at the hydrodynamic boundary (HB), is commonly used as the boundary condition at the substrate surface to consider slip. The one-dimensional form of Navier's slip condition is:

$$u_s = \ell \frac{\partial u}{\partial z}|_{z=z_{\mathrm{HB}}}, \tag{2.4}$$

where ℓ is the slip length, the distance between the HB and the position where the linear extrapolation of the velocity profile vanishes. Navier's slip condition is also often written as:

$$\eta u_s = \mu \frac{\partial u}{\partial z}|_{z=z_{\mathrm{HB}}}, \tag{2.5}$$

where μ is the viscosity and $\eta = \mu/\ell$ is the friction factor. Equation (2.5) expresses the force balance between the friction force from the wall and the viscous shear stress at the HB. We note that research has shown that the HB is often inside the fluid, separated from the substrate surface by a few molecular diameters [63, 65], which is due to a density layering of liquid molecules near the substrate surface. The misaligning between the HB and the substrate surface has negligible effects for macroscopic flows but is important for nanoflows.

In the literature, the effects of slip have been incorporated into the deterministic Planar-film LE using Navier's slip boundary [66]. However, until this thesis, thermal fluctuations and slip have never been explored simultaneously for thin-film flows, due to the lack of proper tools: the Planar-film SLE proposed in [5, 47] does not model slip. The main challenge is to understand whether Navier's slip condition can accurately describe boundary phenomena at the nanoscale, given the stochastic nature of nanoflows, and given the adoption of the fluctuating bulk NS equations. In this thesis (Chapter 3), this question is investigated, and the no-slip Planar-film SLE is extended to consider slip effects and a new Annular-film SLE is derived, also with slip modelled.

There are extensive MD studies of the nature of slip at the nanoscale. It has been shown to depend on factors such as wettability (contact angle), surface roughness of substrates, and applied shear rates. As shown in Fig. 2.9(a), slip length increases with contact angle [67]. In Fig. 2.9(b), non-equilibrium MD simulations of Couette flows by Thompson and Troian [68] showed that slip length is constant at low-shear rates but grows rapidly at high-shear rates.

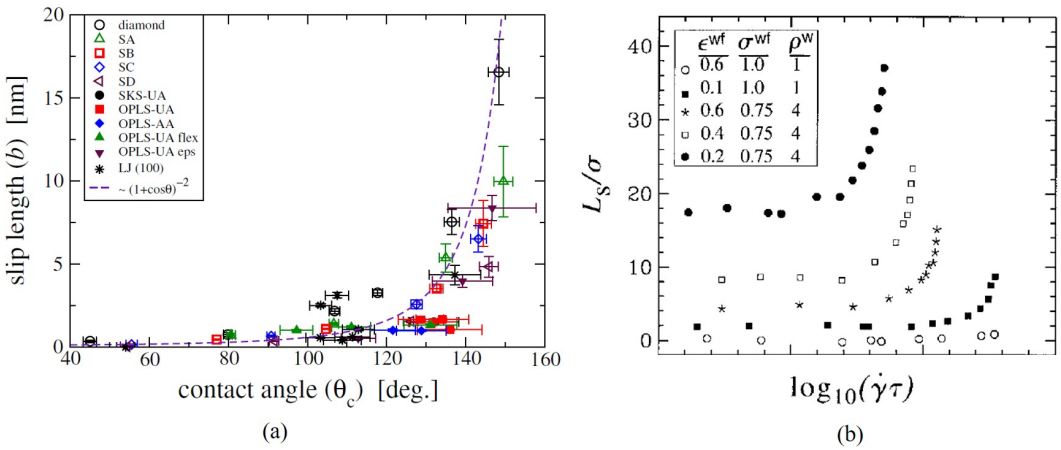

Figure 2.9: (a) Slip length as a function of contact angle [67]. (b) Slip length as a function of shear rates [68].

In thermal equilibrium, transport properties (such as viscosity and heat conductivity) can usually be expressed in terms of integrals of time correlation functions, namely, Green-Kubo relations. Bocquet and Barrat [69] were pioneers in proposing a Green-Kubo-type expression for the friction factor η ($\eta = \mu/\ell$), to identify slip as a property derivable within thermal equilibrium, providing a way to measure slip length in equilibrium simulations. The Green-Kubo expression for the friction factor is

$$\eta = \frac{1}{L_x L_y k_B T} \int_0^\infty \langle F_f(t) F_f(0) \rangle dt, \tag{2.6}$$

where F_f is the friction force at the HB (whose area is $L_x L_y$) along the x direction. Notably, slip length grows rapidly at high-shear rates in non-equilibrium MD simulations. The constant slip at low-shear rates is thus where non-equilibrium MD and equilibrium MD measurements should coincide [70].

Besides those MD studies, seeking accurate methods to measure the slip length experimentally is necessary in real situations. However, this is challenging since such experiments often have to be performed at small scales where invasive techniques are complex. For example, known measurement methods (see the review [71]) include: determining the flow rate at a given pressure drop [72]; measuring the drainage force felt by a submerged sphere approaching the solid using Surface Force Apparatuses and Atomic Force Microscopes [73–75]; finding the flow velocity near the solid directly using Particle Image Velocimetry (PIV) [76], fluorescence recovery and fluorescence cross-correlations [77]. Notably, the aforementioned methods all have to impose a flow in the fluid by external forces, which are difficult to control at small scales and can easily alter the properties of the underlying sys-

tem, e.g. through introducing nanobubbles [78] or deforming soft/biological matter. Therefore, a non-invasive method to measure slip length is needed. Such a method, based on the measurement of the thermal motion of confined colloids, has been proposed and performed experimentally, able to achieve nanometric resolution of the slip length measurement and avoid generating nanobubbles [78].

As mentioned in Sec. 2.2, the correlations of TCWs can be used to infer the properties of liquid-solid systems based on the specific dispersion relation for each system, which has the advantage of being non-invasive. For thin liquid films, the dispersion relation for surface waves depends on the level of slip [58] so that measuring the correlations of thermal capillary waves appears to be a potential method for inferring slip. In fact, it has been recently attempted in experiments for a hexadecane film on a glass [60]. However, the negative slip length obtained is in conflict with the results from other methods [77]. The conflicting result may be due to external forces used in [77] to drive the liquid, potentially leading to a non-linear slip, as pointed out by [60]; though it is clear that further research in this direction is required. On the other hand, the existing experimental study [60] has not considered the exciting possibility that slip is anisotropic.

At larger than nano-scales, it is commonplace to create anisotropic surfaces, with slip becoming flow-direction dependent, which can be used to control drag [79–81]. Such surfaces can be created by patterning micro-ribs and micro-cavities onto a substrate and their effects on flow are measured by the PIV technique [80]. However, at the nanoscale much less is known, partially due to the complexity and the potential problem of invasive methods at these scales. It is thus necessary to investigate how temporal correlations of TCWs behave on anisotropic-slip surfaces and whether measuring correlations of TCWs is a valid and viable way to infer the anisotropic slip.

2.4 Summary of challenges

Through the literature review, one can see that stochastic lubrication equations (SLEs), a long-wave approximation to FH equations, are the tools usually used to study the effects of thermal fluctuations on interfacial flows, but it is an open question how the thermal fluctuations and slip can be modelled simultaneously in thin-film flows. The stochastic nature of flows at the nanoscale may not only change the bulk flow but also change the boundary condition, which calls into question the adoption of Navier's slip condition. The Green-Kubo expression for the friction factor might provide clues on how Navier's slip condition can be modified to accom-

modate these fluctuations.

The 'long-wave' paradigm used to derive SLEs has the inherent problem of being inaccurate for the stochastic dynamics of interfacial waves with short wavelength, and thus may not be applicable to the study of thermal capillary waves. A more general model, beyond the long-wave paradigm, is needed and remains an unknown field to be investigated in this thesis.

Chapter 3

Stochastic modelling of nanoscale interfacial flows

In this chapter, we use both fluctuating hydrodynamics (FH) and Langevin theory to model nanoscale interfacial flows with the effects of thermal fluctuations and liquid-solid slip included. In Sec. 3.1, by virtue of the geometrical assumption for thin films on plates and fibres, we derive stochastic lubrication equations (Planar-film SLE and Annular-film SLE) from FH, with a special treatment for the slip condition. In Sec. 3.2, we propose a Langevin model for the stochastic modelling of interfacial flows, which goes beyond the lubrication paradigm and its long-wave assumption. The theories established in this chapter are used in the work of Chapters 5 to 7.

3.1 Stochastic lubrications equations with slip

The equations of FH for incompressible constant-density flow are given by [9]:

$$\nabla \cdot \boldsymbol{u} = 0\,, \tag{3.1}$$

$$\rho\left(\frac{\partial \boldsymbol{u}}{\partial t} + \boldsymbol{u}\cdot\nabla\boldsymbol{u}\right) = -\nabla p + \mu\nabla^2\boldsymbol{u} + \nabla\cdot\boldsymbol{\tau}. \tag{3.2}$$

Here $\boldsymbol{u}$, ρ, t, p and μ are the velocity field, density, time, pressure and viscosity, respectively. The random stress tensor $\boldsymbol{\tau}$ captures thermal fluctuations, modelled by white noise with zero mean and covariance:

$$\langle \tau_{ij}(\boldsymbol{x},t)\,\tau_{lm}(\boldsymbol{x}',t')\rangle = 2\mu k_B T\left(\delta_{il}\delta_{jm}+\delta_{im}\delta_{jl}\right)\delta\left(\boldsymbol{x}-\boldsymbol{x}'\right)\delta(t-t'), \tag{3.3}$$

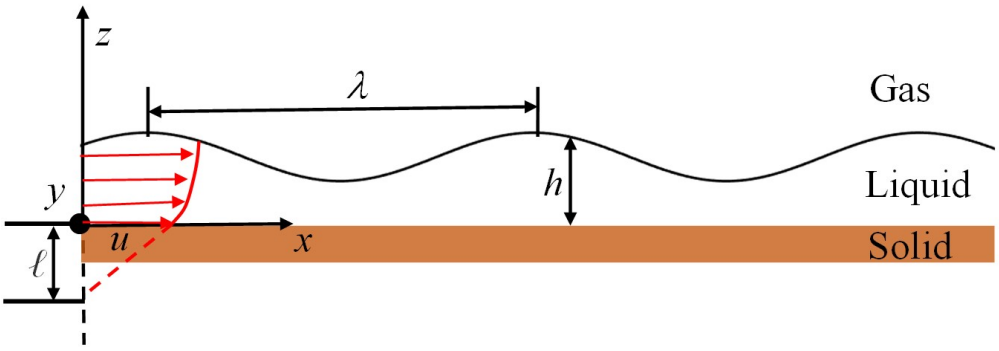

Figure 3.1: Sketch of a liquid film on a plate, where $h = h(x,t)$ is the film thickness, λ is the characteristic length, u is the $x-$component of liquid velocity and ℓ is the liquid-solid slip length. The film has depth L_y in the y direction (into the page).

where $\boldsymbol{x} = (x, y, z)$ and $\langle \cdot \rangle$ is the ensemble average (mean of a random variable over a time interval or a space interval).

3.1.1 Thin films on plates

For a two-dimensional (2D) film on a substrate (Fig. 3.1) with thermal fluctuations and no-slip, Grün *et al.* [5] derived the Planar-film SLE. To do this, a long-wave approximation to the equations of FH was adopted, i.e, $\varepsilon = h_0/\lambda \ll 1$. We extend this analysis to consider the effect of slip at the liquid-solid interface, using a similar long-wave approximation to the equations of FH, but with a special treatment for the slip boundary condition.

In terms of a 2D film on a plate, Eq. (3.1) in Cartesian coordinates is

$$\frac{\partial u}{\partial x} + \frac{\partial w}{\partial z} = 0, \tag{3.4}$$

and Eq. (3.2) is

$$\rho\left(\frac{\partial u}{\partial t} + u\frac{\partial u}{\partial x} + w\frac{\partial u}{\partial z}\right) = -\frac{\partial p}{\partial x} + \mu\left(\frac{\partial^2 u}{\partial x^2} + \frac{\partial^2 u}{\partial z^2}\right) + \frac{\partial}{\partial x}\psi_{xx} + \frac{\partial}{\partial z}\psi_{zx}, \tag{3.5}$$

$$\rho\left(\frac{\partial w}{\partial t} + u\frac{\partial w}{\partial x} + w\frac{\partial w}{\partial z}\right) = -\frac{\partial p}{\partial z} + \mu\left(\frac{\partial^2 w}{\partial x^2} + \frac{\partial^2 w}{\partial z^2}\right) + \frac{\partial}{\partial x}\psi_{xz} + \frac{\partial}{\partial z}\psi_{zz}. \tag{3.6}$$

Here u and w are the x and z components of velocity, and ψ is a 2D random stress tensor with zero mean and covariance given by

$$\langle \psi_{ij}(\boldsymbol{x},t)\, \psi_{lm}(\boldsymbol{x}',t')\rangle = \frac{2\mu k_B T}{L_y}\left(\delta_{il}\delta_{jm} + \delta_{im}\delta_{jl}\right)\delta\left(x-x'\right)\delta\left(z-z'\right)\delta(t-t'). \tag{3.7}$$

The factor $1/L_y$ appears because the planar films we consider here are quasi-2D ($L_y \ll L_x$, L_x and L_y are film length in the x and y directions), allowing all variables of interest to be averaged over the y direction; in particular, $\psi = \frac{1}{L_y}\int_0^{L_y} \tau dy$. For boundary conditions, at $z = h(x,t)$, we have the dynamic condition:

$$(\boldsymbol{\vartheta} + \boldsymbol{\psi}) \cdot \mathbf{n} = -[\gamma \nabla \cdot \mathbf{n} + \phi(h)]\mathbf{n}, \tag{3.8}$$

where $\boldsymbol{\vartheta}$ is the hydrodynamic stress tensor, γ is the surface tension, $\phi(h)$ is the disjoining pressure, and $\mathbf{n}$ is the normal vector at the surface

$$\mathbf{n} = \frac{(-\partial h/\partial x, 1)}{\sqrt{1 + (\partial h/\partial x)^2}}. \tag{3.9}$$

The kinematic condition at $z = h$ is

$$\frac{\partial h}{\partial t} + u\frac{\partial h}{\partial x} = w. \tag{3.10}$$

At $z = 0$, Navier's slip boundary condition is

$$u = \ell \frac{\partial u}{\partial z}, \tag{3.11}$$

where ℓ is the slip length. The substrate is impermeable so that

$$w = 0. \tag{3.12}$$

To get a lubrication equation from governing equations Eq. (3.4-3.12), we need to establish the leading order terms of Eq. (3.4-3.12) by their asymptotic expansion in ε, for which we use the scaling relations suggested by Grün *et al.* [5], before then returning to the dimensional form of the equations for ease of interpretation:

$$\begin{aligned}
&X = x/\lambda, \quad Z = z/h_0, \quad H = h/h_0, \quad T = \frac{u_0}{\lambda}t, \quad U = u/u_0, \\
&W = \frac{w}{\varepsilon u_0}, \quad P = \frac{h_0\varepsilon}{u_0\mu}p, \quad (\Psi_{xx}, \Psi_{zz}) = \frac{\lambda}{u_0\mu}(\psi_{xx}, \psi_{zz}), \\
&(\Psi_{xz}, \Psi_{zx}) = \frac{h_0}{u_0\mu}(\psi_{xz}, \psi_{zx}), \quad \Phi = \frac{h_0\varepsilon}{u_0\mu}\phi, \quad \Gamma = \frac{\varepsilon^3}{u_0\mu}\gamma.
\end{aligned} \tag{3.13}$$

Here non-dimensional variables are upper-case and u_0 is the characteristic velocity.

Using these scaling relations, Eq. (3.5) and Eq. (3.6) become

$$\varepsilon \,\mathrm{Re}\left(\frac{\partial U}{\partial T}+U\frac{\partial U}{\partial X}+W\frac{\partial U}{\partial Z}\right)=-\frac{\partial P}{\partial X}+\varepsilon^2\frac{\partial^2 U}{\partial X^2}+\frac{\partial^2 U}{\partial Z^2}+\frac{\partial \Psi_{zx}}{\partial Z}+\varepsilon^2\frac{\partial \Psi_{xx}}{\partial X}, \tag{3.14}$$

$$\varepsilon^3 \,\mathrm{Re}\left(\frac{\partial W}{\partial T}+U\frac{\partial W}{\partial X}+W\frac{\partial W}{\partial Z}\right)=-\frac{\partial P}{\partial Z}+\varepsilon^2\left(\varepsilon^2\frac{\partial^2 W}{\partial X^2}+\frac{\partial^2 W}{\partial Z^2}+\frac{\partial \Psi_{xz}}{\partial X}+\frac{\partial \Psi_{zz}}{\partial Z}\right). \tag{3.15}$$

Here, the Reynolds number $\mathrm{Re}=\rho u_0 h_0/\mu$ is assumed to be order one or smaller, which is usually valid for nanoscale flows. The leading-order form of the dimensional momentum equations Eq. (3.5) and Eq. (3.6) are thus

$$0=-\frac{\partial p}{\partial x}+\mu\frac{\partial^2 u}{\partial z^2}+\frac{\partial}{\partial z}\psi_{zx}, \tag{3.16}$$

$$0=-\frac{\partial p}{\partial z}. \tag{3.17}$$

On the other hand, the leading-order form of the incompressible condition, Eq. (3.4), remains unchanged.

In the normal direction to the surface, the scaled dynamic condition, Eq. (3.8), is

$$\begin{aligned}P+\Gamma\frac{\partial^2 H/\partial X^2}{\left[1+\varepsilon^2(\partial H/\partial X)^2\right]^{3/2}}=&\varepsilon^2\left\{2\left[1-\left(\frac{\partial H}{\partial X}\right)^2\right]\frac{\partial W}{\partial Z}-2\frac{\partial H}{\partial X}\left(\frac{\partial U}{\partial Z}+\varepsilon^2\frac{\partial W}{\partial X}\right)\right.\\&\left.+\varepsilon^2\left(\frac{\partial H}{\partial X}\right)^2\Psi_{xx}-\frac{\partial H}{\partial X}\left(\Psi_{xz}+\Psi_{zx}\right)+\Psi_{zz}\right\}+\Phi,\end{aligned} \tag{3.18}$$

and the scaled dynamic condition in the tangential direction to the surface is

$$\begin{aligned}&\varepsilon^2\frac{\partial H}{\partial X}\left[2\left(\frac{\partial W}{\partial Z}-\frac{\partial U}{\partial X}\right)+\Psi_{zz}-\Psi_{xx}\right]+\\&\left[1-\varepsilon^2\left(\frac{\partial H}{\partial X}\right)^2\right]\left[\left(\frac{\partial U}{\partial Z}+\frac{\partial W}{\partial X}\varepsilon^2\right)+\Psi_{zx}\right]=0.\end{aligned} \tag{3.19}$$

Therefore, the leading order of the dimensional dynamic boundary conditions in the

normal and tangential direction are seen to be

$$p = -\gamma \frac{\partial^2 h}{\partial x^2} + \phi, \tag{3.20}$$

$$\frac{\partial u}{\partial z} + \psi_{zx} = 0. \tag{3.21}$$

The leading order of the kinematic condition is unchanged. For the slip boundary Eq. (3.11), its scaled form is

$$U = \frac{\ell}{h_0} \frac{\partial U}{\partial Z}. \tag{3.22}$$

Thus, the leading-order slip boundary depends on the ratio ℓ/h_0. In the present work, we consider the slip is at the order of h_0 so that the leading order of the slip boundary condition is unchanged from Eq. (3.11).

To obtain the lubrication equation, Eq. (3.16) is integrated in the z direction, and using Eq. (3.21) gives

$$\frac{\partial u}{\partial z} = \frac{1}{\mu} \left[(z - h) \frac{\partial p}{\partial x} - \psi_{zx} \right]. \tag{3.23}$$

Integrating Eq. (3.23) from 0 to z then gives

$$u - u|_{z=0} = \frac{1}{\mu} \left[\left(\frac{1}{2} z^2 - hz \right) \frac{\partial p}{\partial x} - \int_0^z \psi_{zx}(z') dz' \right], \tag{3.24}$$

and $u|_{z=0}$ is determined by

$$u|_{z=0} = \ell \frac{\partial u}{\partial z}|_{z=0} = -\frac{\ell}{\mu} \left[h \frac{\partial p}{\partial x} + \psi_{zx}|_{z=0} \right]. \tag{3.25}$$

Thus the expression for velocity u is

$$u = \frac{1}{\mu} \left[(\frac{1}{2} z^2 - hz - \ell h) \frac{dp}{dx} - \int_0^z \psi_{zx}(z') dz' - \ell \psi_{zx}|_{z=0} \right]. \tag{3.26}$$

Integrating Eq. (3.4) in z from 0 to h and using the boundary condition Eq. (3.10) and (3.12) gives

$$\frac{\partial h}{\partial t} = -\frac{\partial}{\partial x} \int_0^h u dz. \tag{3.27}$$

By substituting Eq. (3.26) into Eq. (3.27) one can obtain

$$\frac{\partial h}{\partial t} = \frac{1}{\mu} \frac{\partial}{\partial x} \left[M(h) \frac{\partial p}{\partial x} + \int_0^h \int_0^z \psi_{zx}(z') dz' dz + \int_0^h \ell \psi_{zx}\,|_{z=0}\, dz \right], \tag{3.28}$$

where the mobility $M(h) = \frac{1}{3}h^3 + \ell h^2$ takes the usual form obtained in the deterministic setting for the Planar-film LE. For the above double integral, integration by parts leads to

$$\frac{\partial h}{\partial t} = \frac{1}{\mu}\frac{\partial}{\partial x}\left[M(h)\frac{\partial p}{\partial x} + \int_0^h (h-z)\psi_{zx}dz + \ell h\psi_{zx}\,|_{z=0}\right]. \tag{3.29}$$

Before simplifying the noise terms in Eq. (3.29), the covariance of $\psi_{zx}|_{z=0}$ has to be determined, which we will show is given by

$$\left\langle \psi_{zx}|_{z=0}(x,t)\psi'_{zx}|_{z=0}(x',t')\right\rangle = \frac{2\mu k_B T}{\ell L_y}\delta(x-x')\delta(t-t') = \frac{2\eta k_B T}{L_y}\delta(x-x')\delta(t-t'). \tag{3.30}$$

Here $\eta = \mu/\ell$ is the so-called friction factor. Eq. (3.30) is inferred from Bocquet and Barrat's Green-Kubo type expression of friction factor [69], which is

$$\eta = \frac{1}{L_x L_y k_B T}\int_0^\infty \langle F_f(t)F_f(0)\rangle dt, \tag{3.31}$$

where F_f is the friction force at the wall (whose area is L_xL_y) along the x direction. As $F_f = L_xL_y\psi_{zx}|_{z=0}$, Eq. (3.31) leads to

$$\eta = \frac{L_xL_y}{k_BT}\int_0^\infty \langle \psi_{zx}\,|_{z=0}\,(t)\psi_{zx}\,|_{z=0}\,(0)\rangle dt, \tag{3.32}$$

which suggests that the friction factor is related to the stochastic shear stress at the boundary. Notably, this expression for friction factor appears analogous to the Green-Kubo expression for bulk shear viscosity, namely, $\mu = \frac{V}{k_BT}\int_0^\infty \langle \psi_{zx}(t)\psi_{zx}(0)\rangle dt$ (V is the volume of fluid), from which one can obtain the covariance of bulk shear stress $\langle \psi_{zx}\psi'_{zx}\rangle = \frac{2\mu k_BT}{L_y}\delta(x-x')\delta(z-z')\delta(t-t')$ [82]. Thus the covariance of $\psi_{zx}\,|_{z=0}$, namely, Eq. (3.30), is obtained from Eq. (3.32).

Now to simplify the noise terms in Eq. (3.29), we use the method provided in Appendix A for the simplification of the stochastic integral. The two noise terms in Eq. (3.29) are respectively simplified to

$$\int_0^h (h-z)\psi_{zx}dz = \left[\int_0^h (h-z)^2 dz\right]^{1/2}\xi_1 = \sqrt{\frac{1}{3}h^3}\xi_1, \tag{3.33}$$

$$\ell h\psi_{zx}\,|_{z=0} = \sqrt{\ell h^2}\xi_2. \tag{3.34}$$

The $\sqrt{\ell}$ in Eq. (3.34) comes from Eq. (3.30). The ξ_1 and ξ_2 have zero mean and

covariance

$$\left\langle \xi_1(x,t)\xi_1(x',t')\right\rangle = \frac{2\mu k_B T}{L_y}\delta(x-x')\delta(t-t'), \tag{3.35}$$

$$\left\langle \xi_2(x,t)\xi_2(x',t')\right\rangle = \frac{2\mu k_B T}{L_y}\delta(x-x')\delta(t-t'), \tag{3.36}$$

$$\left\langle \xi_1(x,t)\xi_2(x',t')\right\rangle = 0. \tag{3.37}$$

Note that the noise term in the bulk is assumed to be uncorrelated to the value at the surface, Eq. (3.37), so that the two noise terms can be combined together:

$$\int_0^h (h-z)\psi_{zx}dz + \ell h\psi_{zx}\,|_{z=0} = \sqrt{\frac{1}{3}h^3}\xi_1 + \sqrt{\ell h^2}\xi_2 = \sqrt{\frac{1}{3}h^3 + \ell h^2}\xi_3. \tag{3.38}$$

Here ξ_3 has the same covariance as ξ_1 and ξ_2. Thus we derive the Planar-film SLE with slip effects as

$$\frac{\partial h}{\partial t} = \frac{1}{\mu}\frac{\partial}{\partial x}\left\{M(h)\frac{\partial p}{\partial x} + \sqrt{M(h)}\xi\right\}, \tag{3.39}$$

where $p = -\gamma\frac{\partial^2 h}{\partial x^2} + \phi(h)$ is the driving pressure, and the noise ξ (the subscript '3' is omitted) has zero mean and covariance $\langle \xi(x,t)\xi(x',t')\rangle = \frac{2\mu k_B T}{L_y}\delta(x-x')\delta(t-t')$.

Notably, to derive the Planar-film SLE including slip effects, it is essential to include a random friction force at the liquid-solid interface as defined by Eq. (3.30). This finding was also noticed in the study of Brownian motion of solid particles within fluids when slip effects were prominent [83]. We also note that there are several other ways [5, 47, 49, 84] to simplify the stochastic integral in Eq. (3.29). The fluctuation-dissipation theorem is satisfied by the SLE: the variance of the noise (the square of the pre-factor to the noise term) is equal to the mobility, which appears in the diffusion term (the first term of the right-hand side of the SLE). For efficient numerical solutions of stochastic partial differential equations such as this, the reader is referred to the numerical integration schemes discussed in [85, 86].

The generalization of this 2D Planar-film SLE to a 3D version is quite straightforward, and one can obtain

$$\frac{\partial h}{\partial t} = \frac{1}{\mu}\nabla\cdot\left\{Q(h)\nabla p + \sqrt{Q(h)}\boldsymbol{\varsigma}\right\}. \tag{3.40}$$

Here $Q(h) = \frac{1}{3}h^3 + \ell h^2$, $p = -\gamma\Delta h + \phi$, and the noise $\boldsymbol{\varsigma}$ has zero mean and covariance, $\langle \varsigma_i(x,y,t)\varsigma_j(x',y',t')\rangle = 2\mu k_B T\delta_{ij}\delta(x-x')\delta(y-y')\delta(t-t')$, where i and j denote components of the noise vector.

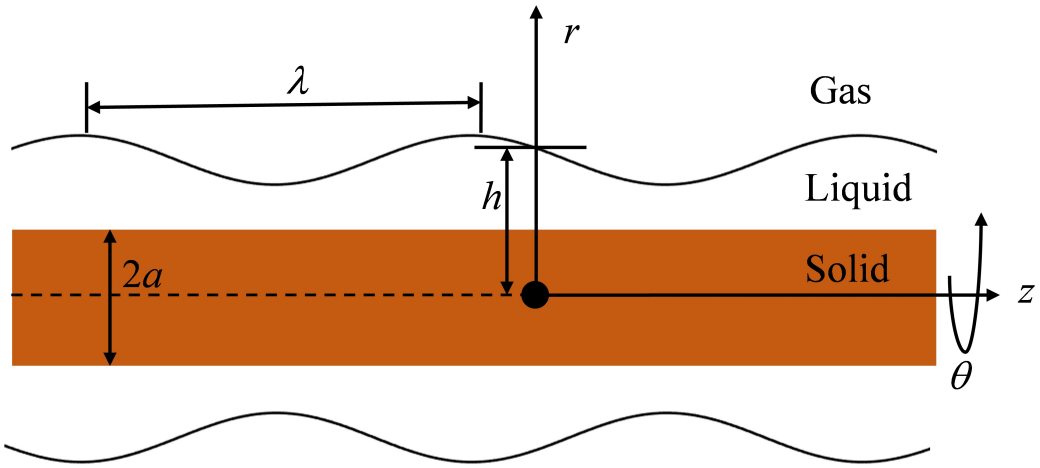

Figure 3.2: Sketch of an annular liquid film on a fibre, where $h = h(z,t)$ is the outer radius of the film, λ is the characteristic length and a is the fibre radius.

3.1.2 Thin films on fibres

Consider now axisymmetric flow of an annular liquid film on a fibre, as shown in Fig. 3.2. Using the same procedure as for the planar thin-film case, at leading order in $\varepsilon = h_0/\lambda \ll 1$, the incompressibility condition in cylindrical coordinates is

$$\frac{\partial w}{\partial z} + \frac{1}{r}\frac{\partial}{\partial r}(ur) = 0\,. \tag{3.41}$$

Here w and u are the axial and radial components of velocity, respectively. The governing momentum equations in cylindrical coordinates (with only leading-order terms) become

$$0 = -\frac{\partial p}{\partial z} + \mu\frac{1}{r}\frac{\partial}{\partial r}\left(r\frac{\partial w}{\partial r}\right) + \frac{1}{r}\frac{\partial}{\partial r}\left(r\zeta_{rz}\right), \tag{3.42}$$

$$0 = -\frac{\partial p}{\partial r}. \tag{3.43}$$

Here ζ_{rz} is the rz component of the random stress tensor ζ, which has zero mean and covariance,

$$\left\langle \zeta_{rz}(r,z,t)\zeta_{rz}(r',z',t')\right\rangle = \frac{\mu k_B T}{\pi r}\delta(r-r')\delta(z-z')\delta(t-t'), \tag{3.44}$$

as we will show now. The covariance of τ in cylindrical coordinates is

$$\begin{aligned}\langle \tau_{ij}(r,\theta,z,t)\, \tau_{lm}(r',\theta',z',t')\rangle =& \frac{2\mu k_B T}{r}\left(\delta_{il}\delta_{jm}+\delta_{im}\delta_{jl}\right)\\ &\times \delta\left(r-r'\right)\delta\left(\theta-\theta'\right)\delta\left(z-z'\right)\delta(t-t'). \end{aligned} \tag{3.45}$$

Due to the axisymmetry of the flow the variables of interest are averaged over the azimuthal direction, e.g., $\zeta = \frac{1}{2\pi}\int_0^{2\pi}\tau d\theta$. Thus the covariance for the azimuthally averaged fluctuating stress tensor is

$$\begin{aligned}\left\langle \zeta_{ij}(r,z,t)\zeta_{lm}(r',z',t')\right\rangle =& \frac{1}{(2\pi)^2}\int_0^{2\pi}\int_0^{2\pi}\left\langle \tau\tau'\right\rangle d\theta d\theta'\\ =& \frac{\mu k_B T}{\pi r}\left(\delta_{il}\delta_{jm}+\delta_{im}\delta_{jl}\right)\delta\left(r-r'\right)\delta\left(z-z'\right)\delta(t-t'). \end{aligned} \tag{3.46}$$

At the free surface $r = h$, the dynamic condition in the normal direction of the surface (at the leading order) is

$$p = -\gamma\left(\frac{\partial^2 h}{\partial z^2}-\frac{1}{h}\right)+\phi\,. \tag{3.47}$$

Notably, the term $\gamma\frac{\partial^2 h}{\partial z^2}$ is not at leading order, but conventionally in this field it is still included in the pressure in an attempt to extend the validity of the model [18, 21]. In the tangential direction (on the $r-z$ plane),

$$\mu\frac{\partial w}{\partial r}+\zeta_{rz}=0. \tag{3.48}$$

The kinematic condition at $r = h$ is

$$\frac{\partial h}{\partial t}+w\frac{\partial h}{\partial z}=u\,. \tag{3.49}$$

At the substrate surface $r = a$, the slip boundary is

$$w=\ell\frac{\partial w}{\partial r}, \tag{3.50}$$

and the impermeability condition is

$$u=0. \tag{3.51}$$

Integrating Eq. (3.42) twice and using two boundary conditions, Eq. (3.48) and

(3.50), leads to an expression for velocity:

$$w = \frac{1}{\mu}\left[\frac{1}{4}\left(r^2-a^2\right) - \frac{1}{2}h^2\log\left(\frac{r}{a}\right) + \left(\frac{1}{2}a - \frac{1}{2}\frac{h^2}{a}\right)\ell\right]\frac{\partial p}{\partial z} - \frac{1}{\mu}\left[\int_a^r \zeta_{rz}(r')dr' + \ell\zeta_{rz}\,|_{r=a}\right]. \tag{3.52}$$

Using Eq. (3.41), Eq. (3.49) and Eq. (3.51), one can obtain

$$h\frac{\partial h}{\partial t} = -\frac{\partial}{\partial z}\int_a^h rw\,dr\,. \tag{3.53}$$

Substituting Eq. (3.52) into Eq. (3.53) results in

$$h\frac{\partial h}{\partial t} = \frac{1}{\mu}\frac{\partial}{\partial x}\left[G(h)\frac{\partial p}{\partial z} + \int_a^h r\int_a^r \zeta_{rz}(r')dr'dr + \int_a^h \ell r\zeta_{rz}|_{r=a}dr\right], \tag{3.54}$$

where the mobility $G(h)$ is

$$G(h) = \frac{-3h^4 - a^4 + 4a^2h^2 + 4h^4\log(h/a) + 4(h^2-a^2)^2\ell/a}{16}. \tag{3.55}$$

A simplification of the double integral in Eq. (3.54) leads to

$$h\frac{\partial h}{\partial t} = \frac{1}{\mu}\frac{\partial}{\partial z}\left[G(h)\frac{\partial p}{\partial x} + \frac{1}{2}\int_a^h (h^2-r^2)\zeta_{rz}(r)dr + \frac{1}{2}\ell\left(h^2-a^2\right)\zeta_{rz}\,|_{r=a}\right]. \tag{3.56}$$

From Bocquet and Barrat's expression of friction factor (in cylindrical coordinates), the covariance of $\zeta_{rz}|_{r=a}$ is found to be

$$\left\langle \zeta_{rz}\,|_{r=a}\,(z,t)\zeta_{rz}\,|_{r=a}\,(z',t')\right\rangle = \frac{\mu k_B T}{\pi a\ell}\delta(z-z')\delta(t-t'). \tag{3.57}$$

Now we are left with the task of finding an equivalent stochastic partial differential equation that does not contain integrals. Using the method in Appendix A, the two noise terms in Eq. (3.56) are simplified respectively to

$$\frac{1}{2}\int_a^h (h^2-r^2)\zeta_{rz}(r)dr = \left[\int_a^h \frac{\left(h^2-r^2\right)^2}{4r}dr\right]^{1/2}\beta_1, \tag{3.58}$$

$$\frac{1}{2}\ell\left(h^2-a^2\right)\zeta_{rz}\,|_{r=a} = \frac{1}{2}(h^2-a^2)\sqrt{\frac{\ell}{a}}\beta_2. \tag{3.59}$$

Here the noise β_1 and β_2 have covariance,

$$\left\langle \beta_1(z,t)\beta_1(z',t')\right\rangle = \frac{\mu k_B T}{\pi}\delta(z-z')\delta(t-t'), \tag{3.60}$$

$$\left\langle \beta_2(z,t)\beta_2(z',t')\right\rangle = \frac{\mu k_B T}{\pi}\delta(z-z')\delta(t-t'), \tag{3.61}$$

$$\left\langle \beta_1(z,t)\beta_2(z',t')\right\rangle = 0. \tag{3.62}$$

Eq. (3.62) results from the assumption that the bulk noise is uncorrelated with the noise at the boundary, allowing the two noise terms to be combined:

$$\begin{aligned}
&\frac{1}{2}\int_a^h (h^2-r^2)\zeta_{rz}(r)dr + \frac{1}{2}\ell\left(h^2-a^2\right)\zeta_{rz}\,|_{r=a} \\
&= \left[\int_a^h \frac{\left(h^2-r^2\right)^2}{4r}dr\right]^{1/2}\beta_1 + \frac{1}{2}(h^2-a^2)\sqrt{\frac{\ell}{a}}\beta_2 \\
&= \sqrt{\int_a^h \frac{(h^2-r^2)^2}{4r}dr + \frac{1}{4}(h^2-a^2)^2\frac{\ell}{a}}\beta_3 \\
&= \sqrt{G(h)}\beta_3.
\end{aligned} \tag{3.63}$$

Here β_3 has the same covariance as β_1 and β_2. Thus the stochastic lubrication equation for an annular film on a fibre with slip effects (the Annular-film SLE) is derived as

$$h\frac{\partial h}{\partial t} = \frac{1}{\mu}\frac{\partial}{\partial z}\left[G(h)\frac{\partial p}{\partial z} + \sqrt{G(h)}\beta\right]. \tag{3.64}$$

Here $p = -\gamma(\frac{\partial^2 h}{\partial z^2} - \frac{1}{h}) + \phi$, and the noise β (the subscript '3' is omitted) has zero mean and covariance $\langle\beta(z,t)\beta(z',t')\rangle = \frac{\mu k_B T}{\pi}\delta(z-z')\delta(t-t')$. Notably, the derived Annular-film SLE can be viewed as an extension of the existing Annular-film LE [21]; an extension that constitutes the addition of an appropriately-scaled noise term.

3.2 Langevin equation: beyond the lubrication paradigm

Central to the derivation of the SLEs above, is the long-wave assumption, which means they cannot accurately predict dynamics of interfacial waves with short wavelengths comparable to that of the film height. To derive the SLEs, we also assumed that the slip length is of the order of the film thickness, which limits their application to relatively small-slip systems. A Langevin model, beyond the current lubrication framework, is thus proposed in this section, to predict the dynamics of capillary waves (at the linear stage) in these more general cases.

3.2.1 Background: the Ornstein–Uhlenbeck process

A basic Langevin equation is the Ornstein–Uhlenbeck (OU) process, which is given by

$$dX_t = -bX_t dt + \Re W_t, \tag{3.65}$$

where X_t is the stochastic variable of interest, W_t is the Wiener process, parameters $b > 0$ and $\Re > 0$. Alternatively, Eq. (3.65) can be written symbolically as

$$\frac{dX_t}{dt} = -bX_t + \Re N(t), \tag{3.66}$$

where $N(t) = dW_t/dt$ is the white noise. The solution of the OU process can be found in many textbooks [87], which is

$$X_t = X_0 e^{-bt} + \Re \int_0^t e^{-b(t-s)} dW_s \,. \tag{3.67}$$

The expectation (mean) of X_t is

$$E(X_t) = X_0 e^{-bt}, \tag{3.68}$$

and the variance of X_t using the Itô isometry is

$$\begin{aligned}
\mathrm{Var}(X_t) =& E\left\{[X_t - E(x_t)]^2\right\} \\
=& E\left\{\left[\Re \int_0^t e^{-b(t-s)} dW_s\right]^2\right\} \\
=& E\left[\Re^2 e^{-2bt} \int_0^t e^{2bs} ds\right] \\
=& \frac{\Re^2}{2b}\left(1 - e^{-2bt}\right).
\end{aligned} \tag{3.69}$$

One useful conclusion can be drawn from the expression of $\mathrm{Var}(X_t)$. At thermal equilibrium, i.e. as $t \to \infty$, the relation between the noise amplitude and the parameter of dissipation can be obtained as follows:

$$\mathrm{Var}(X_t)|_{t=\infty} = \frac{\Re^2}{2b}. \tag{3.70}$$

Equation (3.70) can be used to determine the amplitude of the white noise, since $\mathrm{Var}(X_t)$ and b are often known beforehand; this is known as the fluctuation-dissipation theorem. The famous example is in application to Brownian motion. One can consider that X_t is the velocity of a Brownian particle with a unit mass and b is the

friction exerted on the particle. At thermal equilibrium, $\mathrm{Var}(X_t) = k_B T$ based on the equipartition theorem, so that the noise amplitude is $\Re = \sqrt{2bk_BT}$.

3.2.2 Capillary wave theory

The free surface of a liquid film at rest is rough because of thermal capillary waves (TCWs). At thermal equilibrium, the static spectrum of capillary waves on a planar film can be determined by the equipartition theorem; this forms the basis of classical Capillary Wave Theory (CWT) [56, 88, 89]. For a planar film influenced by the interfacial potential Π, whose derivative is disjoining pressure $\phi = \frac{\partial \Pi}{\partial h}$, the free energy f_1 (henceforth, the subscript '1' denotes that variables are for planar films) due to the change of surface area (in 2D configuration) is

$$f_1 = L_y \gamma \int \left[\sqrt{1 + (\partial h/\partial x)^2} - 1 \right] dx + L_y \int [\Pi(h(x)) - \Pi(h_0)] dx. \tag{3.71}$$

For small deformations ($\partial h/\partial x \ll 1$), $\sqrt{1 + (\partial h/\partial x)^2} - 1 \approx \frac{1}{2}(\partial h/\partial x)^2$ and $\Pi(h) - \Pi(h_0) \approx \frac{\partial \Pi}{\partial h} \mid_{h_0} (h - h_0) + \frac{1}{2} \frac{\partial^2 \Pi}{\partial h^2} \mid_{h_0} (h - h_0)^2$, so that Eq. (3.71) is simplified to

$$f_1 = \frac{L_y}{2} \gamma \int (\partial h/\partial x)^2 dx + \frac{L_y}{2} \frac{\partial^2 \Pi}{\partial h^2} \mid_{h_0} \int [h(x) - h_0]^2 dx. \tag{3.72}$$

Let us define the Fourier transform of $\delta h = h(x) - h_0$ as $\widehat{\delta h} = \int \delta h e^{-iqx} dx$. From Parseval's theorem, we can express Eq. (3.72) in terms of Fourier modes:

$$f_1 = \frac{1}{2} \frac{L_y}{L_x} \gamma \sum q^2 \left| \widehat{\delta h} \right|^2 + \frac{1}{2} \frac{L_y}{L_x} \frac{\partial^2 \Pi}{\partial h^2} \mid_{h_0} \sum \left| \widehat{\delta h} \right|^2. \tag{3.73}$$

As each summand appears quadratically, each mode has the same energy $\frac{1}{2} k_B T$, from equipartition theorem, so that

$$\frac{1}{2} k_B T = \frac{L_y}{L_x} \left(\frac{1}{2} \gamma q^2 + \frac{1}{2} \frac{\partial^2 \Pi}{\partial h^2} \mid_{h_0} \right) \left| \widehat{\delta h} \right|^2. \tag{3.74}$$

Thus, the well-known CWT for a planar film is derived [56, 88, 89]:

$$\left\langle \left| \widehat{\delta h} \right|^2 \right\rangle_1 = \frac{L_x}{L_y} \frac{k_B T}{\gamma q^2 + \partial^2 \Pi / \partial h^2 \mid_{h_0}}. \tag{3.75}$$

It is easy to extend consideration to an axisymmetric annular film. The free energy for an annular film, f_2 (the subscript '2' denotes that variables are for annular

films henceforth), is

$$f_2 = \pi h_0 \int \left\{ \gamma(\partial h/\partial z)^2 - \frac{\gamma}{h_0^2}[h(z) - h_0]^2 \right\} dz + \pi h_0 \int \frac{\partial^2 \Pi}{\partial h^2} \, |_{h_0} [h(z) - h_0]^2 dz, \tag{3.76}$$

so that in Fourier space

$$f_2 = \frac{\pi h_0}{L_x} \sum \left(\gamma q^2 \left| \widehat{\delta h} \right|^2 - \frac{\gamma}{h_0^2} \left| \widehat{\delta h} \right|^2 + \frac{\partial^2 \Pi}{\partial h^2} \, |_{h_0} \left| \widehat{\delta h} \right|^2 \right). \tag{3.77}$$

Applying the equipartition theorem, we obtain the static spectrum of an annular film

$$\left\langle \left| \widehat{\delta h} \right|^2 \right\rangle_2 = \frac{L_x}{2\pi h_0} \frac{k_B T}{\gamma \left(q^2 - 1/h_0^2 \right) + \partial^2 \Pi / \partial h^2 \, |_{h_0}}. \tag{3.78}$$

3.2.3 Langevin equation for thermal capillary waves

For nanoflows, where inertia is usually negligible, Stokes flow governs the flow dynamics. In this regime, for the deterministic setting, linear analyses of free-surface flows are described by equations for the surface perturbation (in Fourier space) of the form:

$$\frac{\partial}{\partial t} \widehat{\delta h} + \Omega \, \widehat{\delta h} = 0 \, , \tag{3.79}$$

where $\Omega(q)$ is the dispersion relation (the decay rate of a particular mode). The dispersion relation for films depends on the domain geometry, the physics at play, and any approximations adopted. For example, for a planar film with slip, no disjoining pressure, and a long-wave approximation, the dispersion relation is

$$\Omega_{\mathrm{LW},1}(q) = \frac{M(h_0)}{3\mu} \gamma q^4, \tag{3.80}$$

from a linear stability analysis of the Planar-film LE [90]. Here 'LW' denotes 'long-wave'. A similar expression is obtained for the annular film from a linear stability analysis of the Annular-film LE, again, adopting a long-wave approximation, which is

$$\Omega_{\mathrm{LW},2}(q) = \frac{G(h_0)}{\mu h_0} \gamma \left(q^4 - q^2/h_0^2 \right), \tag{3.81}$$

For nanoscale liquid films, where the Reynolds number is small, Stokes flow is accurate but the long-wave approximation is less valid, particularly as noise can excite short-wavelength perturbations. For planar films with slip, the Stokes-flow

dispersion relation was obtained in [58],

$$\Omega_{\text{Stokes},1} = \frac{\gamma q}{4\mu} \frac{\sinh(2qh_0) - 2qh_0 + 4q\ell \sinh^2(qh_0)}{\cosh^2(qh_0) + q^2h_0^2 + q\ell\,[2qh_0 + \sinh(2qh_0)]}. \tag{3.82}$$

whilst for annular films with slip, we have derived an expression $\Omega_{\text{Stokes},2}$ for the first time, with details of the relatively standard derivation in Appendix B.

The main idea in this subsection is to establish a framework for taking thermal fluctuations into account in modelling films in the *general* case (i.e. for whichever film geometry, physics, or modelling approximation we adopt). Knowing the restoring pressure due to surface tension is $\beta\widehat{\delta h}$ ($\beta = \gamma q^2$ for planar films and $\beta = \gamma(q^2 - 1/h_0^2)$ for annular films), we can rewrite Eq. (3.79) and add a fluctuating pressure term (white noise) at the same time. This results in a Langevin equation of the form:

$$\frac{\beta}{\Omega}\frac{\partial\widehat{\delta h}}{\partial t} = -\beta\widehat{\delta h} + \zeta\widehat{N}, \tag{3.83}$$

where $\widehat{N}(q,t)$ is a complex Gaussian random variable with zero mean and correlation $\langle|\widehat{N}\widehat{N'}|\rangle = \delta(q-q')\delta(t-t')$, and ζ is the noise amplitude. Since Eq. (3.83) is an OU process, ζ is determined straightforwardly by considering the surface at thermal equilibrium, where $\langle|\widehat{\delta h}|^2\rangle_{\text{s}} = S_{\text{s}}^2 = \frac{\zeta^2\Omega}{2\beta^2}$ ('s' denotes 'static', namely, thermal equilibrium) from Eq. (3.70). Thus, we must have

$$\zeta = \sqrt{\frac{2}{\Omega}}\beta S_{\text{s}}, \tag{3.84}$$

where the static spectrum S_{s} given by CWT in Sec. 3.2.2 (without disjoining pressure) is:

$$S_{\text{s},1} = \sqrt{\frac{L_x}{L_y}\frac{k_BT}{\gamma q^2}}, \tag{3.85}$$

$$S_{\text{s},2} = \sqrt{\frac{L_x}{2\pi h_0}\frac{k_BT}{\gamma(q^2 - 1/h_0^2)}}, \tag{3.86}$$

for planar films and annular films, respectively. The static spectrum for an annular film only works for $qh_0 > 1$. We note that disjoining pressure or gravity can be included in the Langevin model simply by substituting the appropriately modified dispersion relation and static spectrum.

This newly developed Langevin model is one of the key contributions of this thesis, which creates a single theoretical framework under which the dynamics of

thermal capillary waves on films can be studied.

3.3 Summary

In this chapter, to investigate the effects of thermal fluctuations and slip on thin-film flows at the nanoscale, we derive SLEs (Planar-film SLE and Annular-film SLE) for thin films on both plates and fibres using the long-wave approximation to FH equations. To complete the derivation, it is essential to include a random stress at the liquid-solid interface and its covariance is related to the slip length. The derivation process is general, as we demonstrated for films on different substrate geometries, and can be extended to study other thin-film flows at the nanoscale, like free liquid films [91].

In this thesis, the applications of the derived SLEs in Chapters 5 and 6 are linear, with focus on the instability and growth of surface waves at early stages in their development. In the future, it will be interesting, using the developed SLEs, to investigate how thermal fluctuations and slip influence the dynamics during the non-linear stages of film growth, such as on rupture profile, rupture time and droplet distribution. The SLEs developed here also provide useful tools to study nanoscale film dewetting, nanofibre coating and liquid transport using nanofibres [34] where thermal fluctuations and slip are expected to play an important role.

The assumptions made to derive the SLEs (long-waves and small slip) limit their applicability. Thus, we propose a Langevin equation with a Stokes-flow dispersion relation to predict the growth of capillary waves in these more general cases. The applications of this Langevin equation are shown in Chapters 6 and 7.

Chapter 4

Molecular dynamics simulations

With the rapid development of computing power, molecular dynamics (MD) simulations have become a popular tool to explore new physics at the nanoscale, in many different disciplines such as Chemistry and Engineering. As thermal motions of molecules are inherent in MD simulations, performing MD simulations is an excellent method as virtual experiments to study the effects of thermal fluctuations on many physical problems at the nanoscale, such as the motion of contact lines and contact angles [1, 7, 8] and the rupture of nanojets [3].

Most modern codes of MD simulations have been developed relying on the work of Allen and Tildesley [92] and Rapaport [93], where optimised algorithms such as cell lists and Verlet lists are proposed to significantly reduce computational costs. Nowadays, MD codes are well developed and one of the most popular open-source codes is LAMMPS [94], which is adopted in this work to perform MD simulations. LAMMPS has the advantage of running large-scale MD simulations in parallel using message-passing techniques and a spatial-decomposition of the simulation domain, which is needed in our MD simulations where the number of atoms can be up to one million.

In this chapter, Sec. 4.1 introduces the foundations of MD simulations. The MD models of liquid films and solid substrates, used in Chapters 5-7, are presented in Sec. 4.2. Section 4.3 shows the method to extract the free surface of liquid films from MD simulations. The formula of Laplace pressure used in the theoretical modelling is validated in Sec. 4.4, and Sec. 4.5 summarizes the work of this chapter.

4.1 Foundations of MD simulations

In this section, we present the basis of MD simulations including the equations of motion, Lennard-Jones potentials, thermostat strategies, boundary conditions and the calculation of transport properties.

4.1.1 Equations of motion

MD simulation is a particle-based method. The positions and velocities of particles evolve based on Newton's equations of motion, which are

$$\frac{d\boldsymbol{r_i}}{dt} = \boldsymbol{v_i}, \tag{4.1}$$

$$m_i \frac{d\boldsymbol{v_i}}{dt} = \boldsymbol{f_i}, \tag{4.2}$$

where $\boldsymbol{r_i}$, $\boldsymbol{v_i}$, m_i and $\boldsymbol{f_i}$ are positions, velocities, mass and intermolecular forces of the i particles, respectively. The $\boldsymbol{f_i}$ is given by

$$\boldsymbol{f_i} = \sum_{i \neq j} -\nabla U(r_{ij}). \tag{4.3}$$

Here, $U(r_{ij})$ is the intermolecular potential, which depends on the distance of pairwise particles, r_{ij}. The above equations of motion are integrated using the Velocity Verlet algorithm [93], a second-order integrator, to update the positions and velocities of particles. The equations of the Velocity Verlet are:

$$\boldsymbol{r_i}(t + \Delta t) = \boldsymbol{r_i}(t) + \boldsymbol{v_i}(t)\Delta t + \frac{1}{2}(\Delta t)^2 \frac{\boldsymbol{f_i}(t)}{m_i}, \tag{4.4}$$

$$\boldsymbol{f_i}(t + \Delta t) = \boldsymbol{f_i}\left(r_i(t + \Delta t)\right), \tag{4.5}$$

$$\boldsymbol{v_i}(t + \Delta t) = \boldsymbol{v_i}(t) + \frac{1}{2}\Delta t\left(\boldsymbol{f_i}(t) + \boldsymbol{f_i}(t + \Delta t)\right). \tag{4.6}$$

Firstly, we use Eq. (4.4) to update the positions of particles at time $t + \Delta t$, which only depend on velocities and forces at the past time t. Secondly, we use the updated positions of particles to calculate the forces at time $t + \Delta t$, as shown in Eq. (4.5). Thirdly, unlike the way of updating the positions, the velocities at time $t + \Delta t$ depend on both the forces at the past time t and the current time $t + \Delta t$, based on Eq. (4.6).

4.1.2 Intermolecular potentials

The mostly common used potential is the 12-6 Lennard-Jones (LJ) potential and it is also used throughout this thesis, which is given by

$$U(r_{ij}) = \begin{cases} 4\varepsilon \left[\left(\frac{\sigma}{r_{ij}}\right)^{12} - \left(\frac{\sigma}{r_{ij}}\right)^{6} \right] & \text{if } r_{ij} \leq r_c, \\ 0 & \text{if } r_{ij} > r_c, \end{cases} \tag{4.7}$$

where ε is the energy parameter, σ is the length parameter, and r_c is the cut-off distance, beyond which the potential is zero. The choice of ε and σ depends on which liquid is to be simulated. As the computational cost increases significantly with the cut-off distance, a typical cut-off distance is chosen as 5.5σ for a reasonable computation level and good agreements with experimental measurements of transport properties of materials [95].

The force corresponding to this potential is

$$\boldsymbol{f_i} = \frac{48\varepsilon}{\sigma^2} \left[\left(\frac{\sigma}{r_{ij}}\right)^{14} - \frac{1}{2}\left(\frac{\sigma}{r_{ij}}\right)^{8} \right] \boldsymbol{r_{ij}}, \tag{4.8}$$

provided $r_{ij} \leq r_c$, and zero otherwise. The vector $\boldsymbol{r_{ij}} = r_{ij}\boldsymbol{e_{ij}}$, where $\boldsymbol{e_{ij}}$ is the unit vector along pairwise particles. It can be seen that there is no discontinuity for the potential and the force at r_c (since they are not zero at r_c) but this has no real effect on the numerical solutions [93]. One can also find that the force has zero value at $r_{ij} = 2^{1/6}\sigma$ so that the force is purely repulsive for $r_{ij} < 2^{1/6}\sigma$, which can be used to model immiscible liquids.

4.1.3 Thermostatting strategies

In this thesis, all MD simulations are isothermal, which requires a thermostatting method to keep the temperature constant. Popular thermostats include velocity scaling, the Andersen thermostat [96], the Berendsen thermostat [97] and the Nosé-Hoover thermostat [98]. For the current work, the Nosé-Hoover thermostat is adopted as it is one of the most accurate and efficient methods for constant-temperature MD simulations [92]. This method was originally proposed by Nosé and subsequently developed by Hoover [98, 99]. Their central idea is to couple the simulated system to an external heat bath with a fixed temperature.

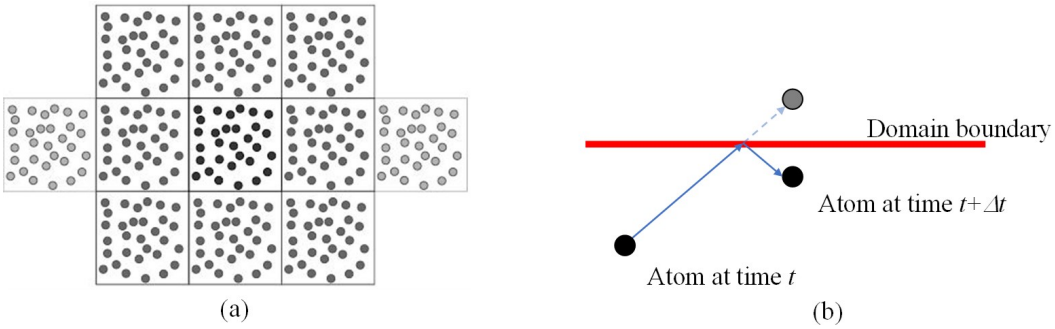

Figure 4.1: (a) The meaning of periodic boundary conditions; (b) The meaning of the reflective wall condition.

4.1.4 Boundary conditions in MD simulations

Periodic boundary conditions are frequently used in MD simulations. Their introduction is equivalent to considering an infinite, space-filling array of identical copies of the simulation region [93], as shown schematically in Fig. 4.1(a). In practice, there are two consequences of this periodicity. The first is that an atom that leaves the simulation region through a particular bounding face immediately re-enters the region through the opposite face but without changing its velocities. The second is that atoms lying within a distance r_c of a boundary interact with atoms in an adjacent copy of the system, or, equivalently, with atoms near the opposite boundary – a wraparound effect. To avoid the interaction between a particle and its own copies in neighbouring boxes, it is necessary to make sure that the cut-off distance r_c is no more than half the smallest region dimension.

Importantly, periodic boundary conditions inhibit the occurrence of any fluctuations with wavelengths longer than the domain length [92]. For example, for a cube of side L, the periodicity will suppress any density waves with a wavelength greater than L. This also applies to surface waves; the smallest wavenumber of interfacial modes is $q = 2\pi/L$.

Another boundary condition used in this thesis is the reflective wall, as sketched in Fig. 4.1(b), which means if an atom moves outside the wall on a timestep by a distance delta, then it is put back inside the face by the same delta, and the sign of the corresponding component of its velocity is flipped.

4.1.5 Calculating transport properties

To compare with the predictions of continuum models, the transport properties (such as dynamic viscosity and surface tension) of molecular liquids need to be

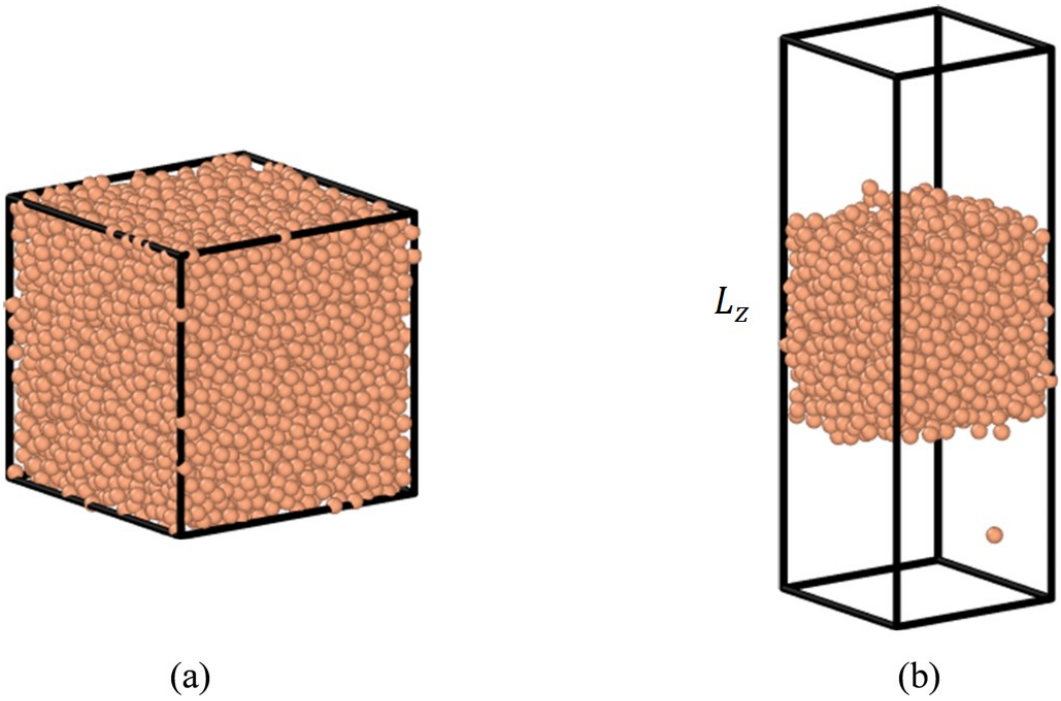

Figure 4.2: MD systems to obtain transport properties. (a) a cubic box of liquid for the measurement of viscosity; (b) a bulk of liquid with two free surfaces for the measurement of surface tension.

obtained. The dynamic viscosity is obtained by the Green-Kubo expression [100]:

$$\mu = \frac{V}{k_B T} \int_0^\infty \langle \psi_{zx}(t) \psi_{zx}(0) \rangle dt, \tag{4.9}$$

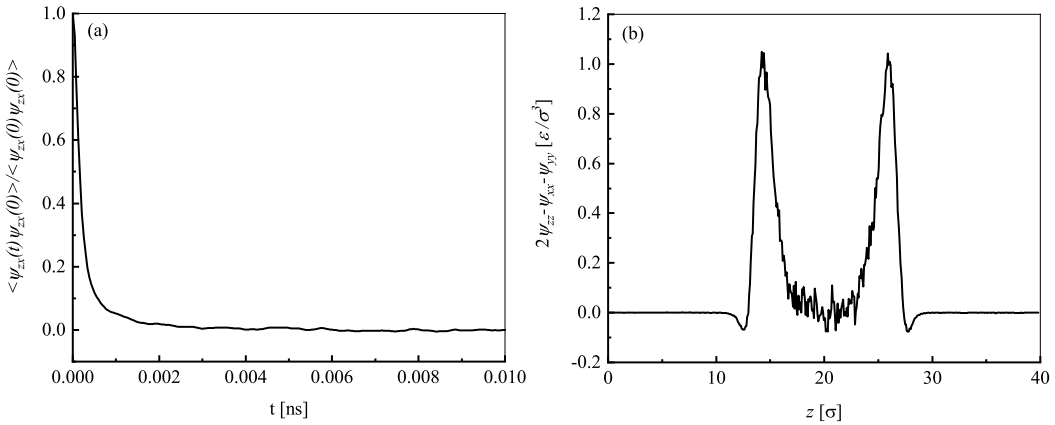

Figure 4.3: (a) the decay of the correlation of shear stress; (b) the distribution of $2\psi_{zz} - \psi_{xx} - \psi_{yy}$.

where V is the volume of the liquid and ψ_{zx} is the shear stress. To calculate the viscosity numerically in MD simulations, a cubic box of molecules undergoing thermal motions is simulated with periodic conditions in all three directions, as shown in Fig. 4.2(a). The temporal correlation of the shear stress, which decays to zero with time, is then obtained from the MD simulation (see Fig. 4.3(a)) and integrated to obtain the viscosity (using trapezoidal rule).

The value of surface tension is obtained by the viral expression [95] in a domain containing two free surfaces (see, Fig. 4.2(b)):

$$\gamma = \frac{1}{4}\int_0^{L_z} (2\psi_{zz} - \psi_{xx} - \psi_{yy})\, dz. \tag{4.10}$$

Here L_z is the length of the MD domain in the vertical direction, z. The integrand of Eq. (4.10) is obtained from the MD simulation (by dividing the domain into bins) and plotted in Fig. 4.3(b), which is then integrated to obtain the value of surface tension.

4.2 Molecular models of liquid films and solid substrates

In this section, the molecular models of liquid films and solid substrates (plates and fibres in geometry) are presented, which are used in Chapters 5–7.

The molecular liquid we use is argon. For argon, the energy parameter ε_{ll} (the subscript ll stands for liquid-liquid interactions), the length parameter σ_{ll}, and atomic mass are 1.67×10^{-21} J, 0.34 nm, and 6.63×10^{-26} kg, respectively. The temperature of this system is kept at $T = 85$ K or $T^* = 0.7\varepsilon_{ll}/k_B$ (* henceforth denotes LJ units). At this temperature, the mass density of liquid argon is 1.40×10^3 kg/m^3 and number density $n^* = 0.83/\sigma_{ll}^3$ [101]. The number density of the vapor phase is $1/400n^*$ [101]. As such, in the continuum models in Chapter 3, the vapor is assumed to be dynamically passive and has no effect on the dynamics of liquid films. The cut-off distance, beyond which the intermolecular interactions are omitted, is chosen as $r_c{}^* = 5.5\sigma_{ll}$. To compare with the predictions of a continuum model, the transport properties of liquid argon are calculated based on the methods described in Sec. 4.1.5. It is found that the surface tension $\gamma = 1.52 \times 10^{-2}$ N/m and the dynamic viscosity $\mu = 2.87 \times 10^{-4}$ kg/(ms).

The substrate is platinum with a face centred cubic (fcc) structure with a mass density 21.45×10^3 kg/m^3 and an atomic mass 3.24×10^{-25} kg. It has been noticed before that the different planes of the fcc lattice lead to varying slip properties due to the difference in interfacial atom structures [102]. In this work,

the ⟨100⟩ surface and ⟨110⟩ are adopted to form plates (planar substrates), which are shown in Fig. 4.4.

In terms of fibres (cylindrical substrates), two different atomic structures are considered: the one in Fig. 4.5(a) is generated by cutting a cylinder from a large cube of platinum; the one in Fig. 4.5(b) consists of two concentric surfaces, of which the cross section consists of two rings with a same number of particles distributed uniformly.

The solid substrate is assumed to be rigid, which saves considerable computational cost compared with flexible walls. Instead, one may use flexible substrates if the computational cost is affordable but previous studies show the two kinds of wall produce very similar results [12]. The liquid-solid interactions are also modelled by the same 12-6 LJ potential with $\varepsilon_{ls} = C\varepsilon_{ll}$ and $\sigma_{ls} = 0.8\sigma_{ll}$. We vary C to obtain different amounts of slip. The value of C is detailed in Chapters 5–7.

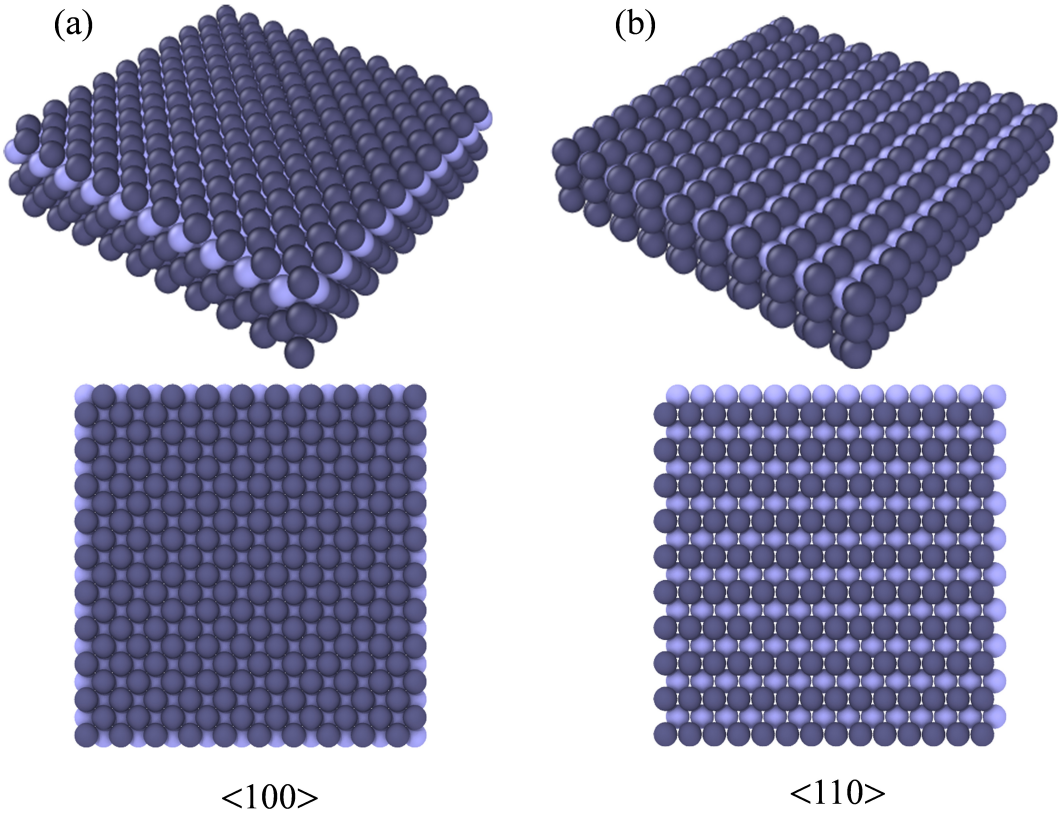

Figure 4.4: Snapshots of the ⟨100⟩ and ⟨110⟩ substrate surface in MD simulations. (a) perspective and top views of the ⟨100⟩ surface; (b) perspective and top views of the ⟨110⟩ surface. The light blue color indicates solid atoms in the second layer.

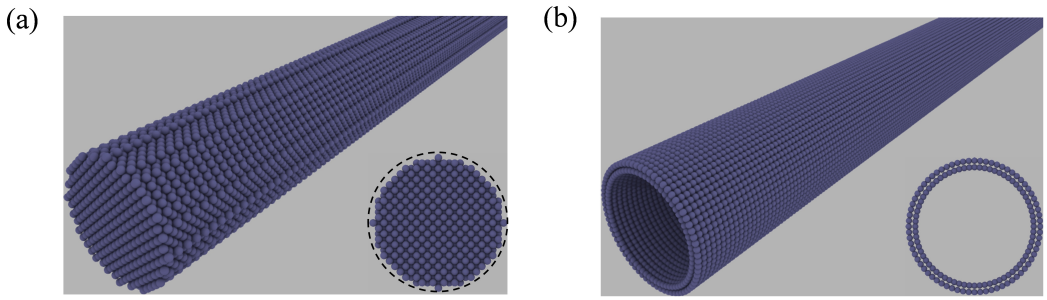

Figure 4.5: Two kinds of fibres. (a) Fibre 1, cut out from a bulk of platinum with a fcc structure. (b) Fibre 2, consisting of two concentric surfaces.

4.3 Extracting free-surface positions

To obtain the position of the liquid-vapour interface, we first locate all liquid molecules by calculating the number density within one spherical radius of each molecule. For example, if the total number of molecules within the d distance from a given molecule is N, the density of this molecule will be $N/(4/3\pi d^3)$. The threshold density for defining a liquid molecule is chosen as $0.5n^*$ as the interface molecules have half of their spherical volume in vapour and half in liquid. For planar films, liquid molecules are then subdivided into columns and the molecules with the highest vertical coordinate in each column are found; this defines the liquid-vapour interface. One example of finding the liquid-vapour interface for planar films is shown by Fig. 4.6(a), where the dots are liquid molecules and the solid line is the extracted interface. Note that the film has a small depth into the page and the solid line is the averaging result over the depth. Similarly, for annular films, liquid molecules are subdivided into circular sectors and the molecules with the largest distance to the center in each sector are found, which forms the liquid-vapour interface, as demonstrated in Fig. 4.6(b).

4.4 Validation of Laplace pressure at the nanoscale

In this section, we are interested in validating the formula of Laplace pressure which is adopted in our theoretical models of interfacial flows. The Laplace pressure is given by

$$\Delta p = -\gamma \left(\frac{1}{R_1} - \frac{1}{R_2} \right), \tag{4.11}$$

where R_1 and R_2 are the two principal radii of curvatures. To validate this expression, we simulate a liquid bridge between two solid plates as shown in Fig. 4.7.

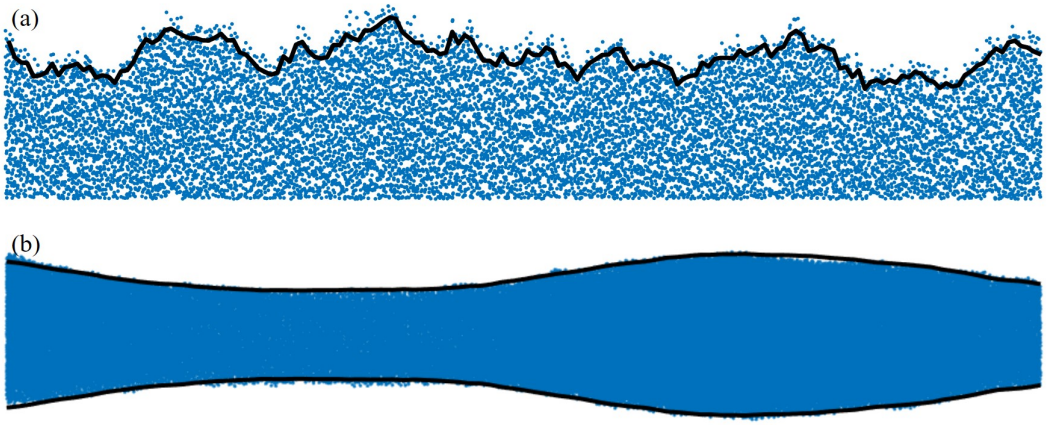

Figure 4.6: The extraction of the free surface, (a) for planar films and (b) for annular films. The dots are particles and the solid lines are the extracted interface.

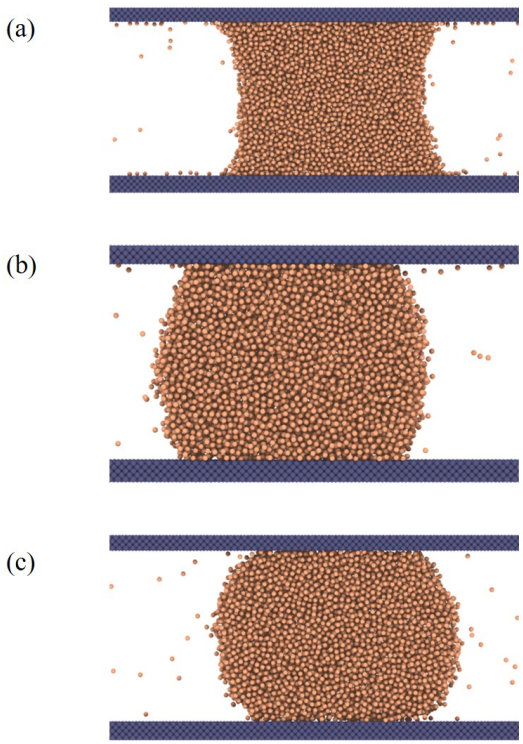

Figure 4.7: Liquid bridges between two plates, (a) $\varepsilon_{ls} = 0.65\varepsilon_{ll}$, (b) $\varepsilon_{ls} = 0.35\varepsilon_{ll}$, (c) $\varepsilon_{ls} = 0.20\varepsilon_{ll}$.

Note that we apply a periodic condition into the page so that those bridges are two-dimensional. The extra pressure in the liquid due to the curvature is

$$\Delta p = -\frac{2\gamma \cos\theta_c}{h}, \tag{4.12}$$

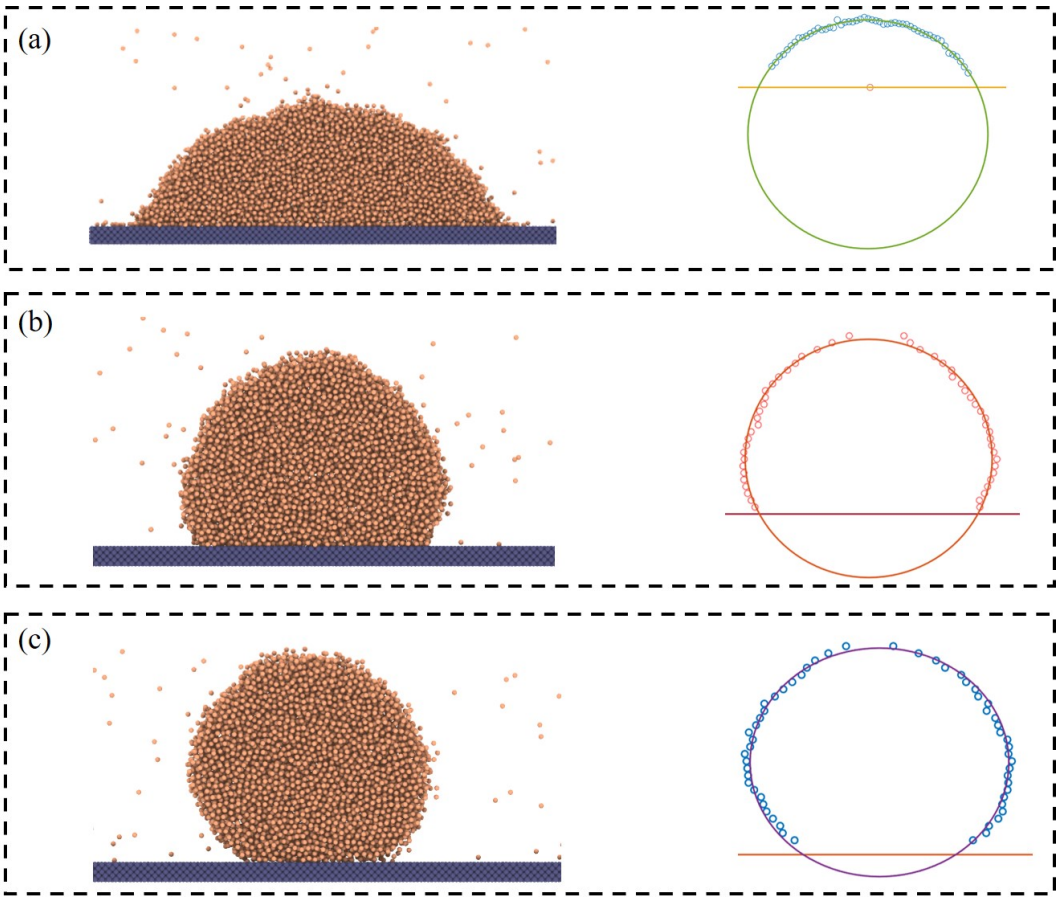

Figure 4.8: Liquid cylinders on plates simulated in MD simulates (on the left panel) and the extractions of contact angles by fitting the surface shape with a circle (on the right panel), (a) $\varepsilon_{ls} = 0.65\varepsilon_{ll}$, (b) $\varepsilon_{ls} = 0.35\varepsilon_{ll}$, (c) $\varepsilon_{ls} = 0.20\varepsilon_{ll}$.

where θ_c is the contact angle and h is the distance between two plates. Figures 4.7(a-c) shows three liquid bridges with different contact angles, which is achieved by changing the liquid-solid interactions ε_{ls}.

To obtain the contact angles of those bridges, we simulate liquid cylinders on plates, as shown in the left panel of Fig. 4.8. We use the method discussed earlier in the previous subsection to extract the free surface and average it over different time instances, and fit it with a circle (the equilibrium profile), see the right panel of Fig. 4.8. Thus, the contact angle is the angle between the tangent line to the circle at the solid surface and the tangent line with the solid surface.

After obtaining the contact angles, we use Eq. (4.12) to predict the values of pressure in those liquid bridges in Fig. 4.7, which are then compared with the pressure measured directly from MD simulations. The comparison between the

predicted pressure and the measured pressure is listed in Table 4.1, and the good agreements between them validate the correctness of the formula of Laplace pressure at the nanoscale (note that the pressure of the vapour is zero).

ε_{ls}	Contact angle (degree)	Pressure inferred	Pressure measured
0.65	65	-0.0308	-0.0311
0.35	117	0.0331	0.0362
0.20	143	0.0582	0.0615

Table 4.1: Validation of the Laplace pressure.

4.5 Summary

In this chapter, the basis of MD simulations is introduced and then extended to describe the MD models of liquid films and solid substrates. We also validate the formula of Laplace pressure. Though these models are simple and ideal, they are sufficient to demonstrate the important physics we find in Chapters 5–7, since experimental studies are extremely limited currently.

Chapter 5

Instability of nanofilms on plates

In this chapter, we consider the spinodal dewetting of nanofilms on substrates caused by disjoining pressure, which is conventionally described by the deterministic Planar-film LE, but here we revisit this problem using the Planar-film SLE developed in Chapter 3 to consider the effects of thermal fluctuations.

This chapter is organized as follows. Sec. 5.1 shows a linear stability analysis of the Planar-film LE. In Sec. 5.2, we present a linear stability analysis of the Planar-film SLE to derive the spectra of surface waves. MD simulations of the dewetting of nanofilms are shown in Sec. 5.3. Sec. 5.4 shows the comparison of MD results and the theoretical predictions. We summary all findings in Sec. 5.5.

5.1 Classical instability mechanism with disjoining pressure

Williams and Davis [19] derived the Planar-film LE with the effects of disjoining pressure. A linear stability analysis of the Planar-film LE equation reveals a fastest growing mode and a critical wavelength (perturbations with a wavelength larger than this value grow) [19]. The critical wavelength is often used to predict whether a film of a particular size is stable, and the fastest growing mode is used to estimate the rupture time and number of holes/drops after film rupture [35, 42]. Here we repeat the process of the classical instability analysis. The Planar-film LE equation, in one-dimensional form is (Eq. (3.39) without the stochastic term and slip length):

$$\frac{\partial h}{\partial t} = \frac{1}{\mu}\frac{\partial}{\partial x}\left[\frac{1}{3}h^3\frac{\partial}{\partial x}\left(\phi - \gamma\frac{\partial^2 h}{\partial x^2}\right)\right]. \tag{5.1}$$

This equation is linearised using $h = h_0 + \delta h$, with the assumption that δh represents small deviations from the initial film thickness h_0, so that one can obtain:

$$\frac{\partial \delta h}{\partial t} = \frac{1}{3\mu} h_0^3 \frac{\partial}{\partial x} \left[-\gamma \frac{\partial^3 \delta h}{\partial x^3} + \frac{\partial \phi}{\partial h} |_{h=h_0} \frac{\partial \delta h}{\partial x} \right]. \tag{5.2}$$

The stability of Eq. (5.2) is examined using normal modes:

$$\delta h = \widehat{\delta h}\, e^{\omega(q)t + iqx}. \tag{5.3}$$

A substitution of Eq. (5.3) into Eq. (5.2) leads to the dispersion relation

$$\omega(q) = \frac{h_0^3}{3\mu} \left(-\gamma q^4 + q^2 \frac{\partial \phi}{\partial h} |_{h=h_0} \right). \tag{5.4}$$

The critical wavenumber q_c is when $\omega(q) = 0$, and the dominant wavnumber q_d is when $\omega(q)$ has its maximum, so that one can obtain:

$$q_c = \sqrt{-\frac{1}{\gamma} \frac{\partial \phi}{\partial h} |_{h=h_0}}, \tag{5.5}$$

$$q_d = \frac{\sqrt{2}}{2} q_c. \tag{5.6}$$

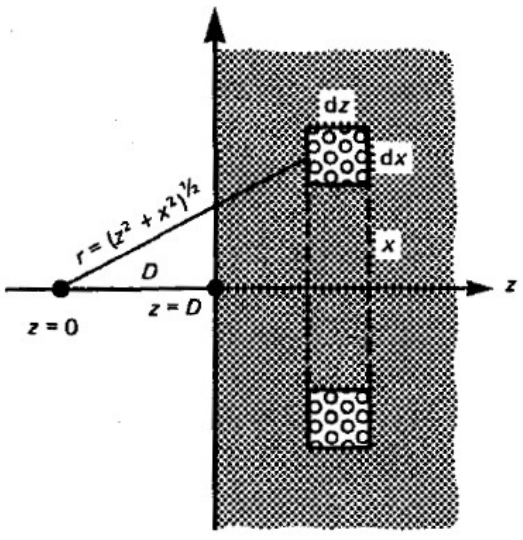

Figure 5.1: A sketch of the molecule-substrate interaction. The molecule is located at $(x = 0, y = 0, z = 0)$ and the semi-finite substrate (the shadow area) is located at $z = D$. Image taken from [103].

On the other hand, the surface spectra (amplitude of surface modes) is

$$\left|\widehat{\delta h}(q,t)\right| = \left|\widehat{\delta h}(q,0)\right| e^{\omega(q)t}, \tag{5.7}$$

from the assumption of normal modes. Here $\left|\widehat{\delta h}(q,0)\right|$ is the initial condition of the surface.

To continue the analysis, one has to specify the expression of disjoining pressure. There are many forms of disjoining pressure reported in the literature and different choices of disjoining pressure cause different flow behaviour in a thin film [104, 105]. The disjoining pressure for the work considered here is based on our molecular simulation of a thin film on a substrate. As shown in Fig. 5.1, the total interaction energy exerted on a molecule by a semi-infinitely extended substrate with density n_s is

$$\begin{aligned} f(D) &= \int_{z=D}^{z=\infty}\int_{x=0}^{x=\infty}\left[\frac{4\varepsilon_{ls}\sigma^{12}}{r^{12}} - \frac{4\varepsilon_{ls}\sigma^{6}}{r^{6}}\right] 2\pi x n_s \, dx \, dz \\ &= \int_{z=D}^{z=\infty} dz \int_{x=0}^{x=\infty}\left[\frac{4\varepsilon_{ls}\sigma^{12}}{\left(z^2+x^2\right)^6} - \frac{4\varepsilon_{ls}\sigma^{6}}{\left(z^2+x^2\right)^3}\right] 2\pi x n_s dx \\ &= \frac{4\varepsilon_{ls} n_s \sigma^{12}}{45 D^9} - \frac{4\varepsilon_{ls} n_s \sigma^{6}}{6 D^3}, \end{aligned} \tag{5.8}$$

where D is the distance between the molecule and the solid surface, and $2\pi x \, dx \, dz$ is the volume of the circular ring (its cross-sectional area is $dx \, dz$ and radius is x shown in Fig. 5.1). Thus, for a unit volume of liquid at the free surface of a film with thickness h, the interaction energy is

$$\begin{aligned} \phi(h) &= f(h)\, n_l \\ &= \frac{4\varepsilon_{ls} n_s n_l \sigma^{12}}{45 h^9} - \frac{4\varepsilon_{ls} n_s n_l \sigma^{6}}{6 h^3}. \end{aligned} \tag{5.9}$$

With the classic definition of the Hamaker constant $A_{ls} = 4\pi^2 \varepsilon_{ls} \sigma_{ls}^6 n_l n_s$, one can rewrite Eq. (5.9) as

$$\phi(h) = \frac{A_{ls}}{6\pi}\frac{2}{15}\sigma^6 \left(\frac{1}{h}\right)^9 - \frac{A_{ls}}{6\pi}\left(\frac{1}{h}\right)^3. \tag{5.10}$$

In the static case, the NS equation reduces to a simple pressure balance:

$$\nabla p = \nabla \phi, \tag{5.11}$$

so that the disjoining pressure in the film surface due to the solid is

$$p = \phi(h). \tag{5.12}$$

From Eq. (5.10), the ratio of the attractive part of LJ potential (the h^{-3} term) to the repulsive part (the h^{-9} term) is $\frac{15}{2}\left(\frac{h}{\sigma}\right)^6$. Therefore, as σ has the size of one molecule, and given the film thickness h in this work is chosen to contain several molecules, the repulsive part of the LJ potential makes a negligible contribution to the linear stability analysis and will be ignored. Furthermore, considering that a free liquid film will rupture itself due to the attraction of its two surfaces, the Hamaker constant A_{ls} in Eq. (5.10) is replaced by the difference between the Hamaker constant of the liquid film itself A_{ll} and the liquid-solid Hamaker constant, i.e. $A_{ll} - A_{ls}$ [106, 107], so that Eq. (5.10) becomes

$$\phi = \frac{A_{ll} - A_{ls}}{6\pi h^3}. \tag{5.13}$$

Here, $A_{ll} = 4\pi^2 \varepsilon_{ll} \sigma_{ll}^6 n_l^2$. Finally, due to the finite thickness of the substrate in MD simulations, the disjoining pressure takes the form

$$\phi = \frac{A_{ll} - A_{ls}}{6\pi h^3} + \frac{A_{ls}}{6\pi (h + h_s)^3}. \tag{5.14}$$

This is because the top surface of a liquid film, which is located at h from a semi-infinite substrate, has the pressure $\phi_1 = A_{ls}/(6\pi h^3)$ and if located at $h + h_s$ away from the substrate, the pressure is $\phi_2 = A_{ls}/[6\pi(h + h_s)^3]$. Thus the contribution from a substrate with thickness h_s should be $\phi_1 - \phi_2$. Added to the disjoining pressure of the liquid film itself, we arrive at Eq. (5.14).

5.2 New instability mechanism accounting for thermal fluctuations

As the thickness of thin liquid films reaches the nanoscale, thermal fluctuations may play an important role in the instability process. Recently Zhao *et al.* [53] derived a spectrum for growing surface waves of a nanojet due to the Rayleigh-Plateau instability, with the inclusion of the effects of thermal fluctuations, and found good agreement with MD simulations, which cannot be predicted by the classical instability analysis.

Here, the effects of thermal fluctuations on the instability of thin films on

plates are considered using the Planar-film SLE. In this problem, we ignore slip so that the Planar-film SLE is reduced to

$$\frac{\partial h}{\partial t} = \frac{1}{\mu}\frac{\partial}{\partial x}\left[\frac{1}{3}h^3\frac{\partial}{\partial x}\left(\phi - \gamma\frac{\partial^2 h}{\partial x^2}\right)\right] + \sqrt{\frac{2k_BT}{\mu L_y}}\frac{\partial}{\partial x}\left(\sqrt{\frac{1}{3}h^3}N\right). \tag{5.15}$$

We linearise Eq. (5.15) using $h = h_0 + \delta h$, with the assumption that δh represents small deviations from the initial film thickness h_0 and the noise amplitude is also assumed to be small, as explained in [51]. By expanding Eq. (5.15) to first order, the linearised SLE equation is

$$\frac{\partial \delta h}{\partial t} = \frac{1}{3\mu}h_0^3\frac{\partial}{\partial x}\left[-\gamma\frac{\partial^3 \delta h}{\partial x^3} + \frac{\partial \phi}{\partial h}|_{h=h_0}\frac{\partial \delta h}{\partial x}\right] + \sqrt{\frac{2k_BTh_0^3}{3\mu L_y}}\frac{\partial N}{\partial x}. \tag{5.16}$$

Taking the Fourier transform of Eq. (5.16) using

$$\widehat{\delta h} = \int_{-\infty}^{\infty} \delta h(x,t)e^{-iqx}dx, \tag{5.17}$$

$$\widehat{N} = \int_{-\infty}^{\infty} N(x,t)e^{-iqx}dx, \tag{5.18}$$

leads to

$$\frac{\partial \widehat{\delta h}}{\partial t} = \omega(q)\widehat{\delta h} + i\sqrt{\frac{2k_BTh_0^3}{3\mu L_y}}q\widehat{N}. \tag{5.19}$$

Here $\omega(q)$ is the same dispersion relation as that of the deterministic LE equation, Eq. (5.4).

The solution of Eq. (5.19) can be represented as the linear superposition of two contributions

$$\widehat{\delta h} = \widehat{\delta h}_{\text{det}} + \widehat{\delta h}_{\text{flu}}, \tag{5.20}$$

where $\widehat{\delta h}_{\text{flu}}$ is the contribution purely caused by thermal fluctuations and $\widehat{\delta h}_{\text{det}}$ is the solution to the deterministic part of Eq. (5.19), i.e., $\frac{\partial \widehat{\delta h}}{\partial t} = \omega(q)\widehat{\delta h}$; obtained as below

$$\widehat{\delta h}_{\text{det}}(q,t) = \widehat{\delta h}(q,0)e^{\omega(q)t}, \tag{5.21}$$

where the initial disturbance is $\widehat{\delta h}(q,0)$; here this is the Fourier transform of the liquid surface found in MD simulations at $t = 0$. This result can be directly obtained by assuming the surface has the normal modes for the Planar-film LE, see Eq. (5.7).

To find the contribution of the fluctuating component to the spectrum, we

determine the impulse response of the linear system $\frac{\partial\widehat{\delta h}}{\partial t} = \omega(q)\widehat{\delta h}$ through:

$$\frac{\partial\widehat{\delta h}}{\partial t} = \omega(q)\widehat{\delta h} + \delta\left(t\right). \tag{5.22}$$

Performing a Laplace transform of Eq. (5.22) using $g(q,s) = \int_0^\infty \widehat{\delta h}(q,t)e^{-ts}dt$ with zero initial disturbance $\widehat{\delta h}(q,0) = 0$ gives

$$g = \frac{1}{s-\omega(q)}, \tag{5.23}$$

so that from the inverse Laplace transform, the impulse response is simply

$$H = \widehat{\delta h} = e^{\omega(q)t}. \tag{5.24}$$

Now with thermal fluctuations $i\sqrt{\frac{2k_BTh_0^3}{3\mu L_y}}q\widehat{N}$ as the input, we find

$$\widehat{\delta h}_{\text{flu}} = i\sqrt{\frac{2k_BTh_0^3}{3\mu L_y}}q\int_0^t \widehat{N}\left(q,t-\tau\right)H(q,\tau)d\tau. \tag{5.25}$$

As $\widehat{\delta h}$ is both a random and complex variable, the root mean square (rms) of its norm is sought, which, from Eq. (5.20), is given by

$$\left|\widehat{\delta h}\right|_{\text{rms}} = \sqrt{\overline{\left|\widehat{\delta h}_{\text{det}} + \widehat{\delta h}_{\text{flu}}\right|^2}} = \sqrt{\left|\widehat{\delta h}_{\text{det}}\right|^2 + \overline{\left|\widehat{\delta h}_{\text{flu}}\right|^2}}, \tag{5.26}$$

(as the average of $\widehat{\delta h}_{\text{flu}}$ is zero) where from Eq. (5.21)

$$\left|\widehat{\delta h}_{\text{det}}\right|^2 = \left|\widehat{\delta h}(q,0)\right|^2 e^{2\omega(q)t}, \tag{5.27}$$

and from Eq. (5.25)

$$\begin{aligned}
\overline{\left|\widehat{\delta h}_{\text{flu}}\right|^2} &= \frac{2k_BTh_0^3q^2}{3\mu L_y}\overline{\left|i\int_0^t \widehat{N}\left(q,t-\tau\right)H(q,\tau)d\tau\right|^2} \\
&= \frac{2k_BTh_0^3q^2}{3\mu L_y}\int_0^t \overline{\left|\widehat{N}\left(q,t-\tau\right)\right|^2}H(q,\tau)^2d\tau \\
&= \frac{2k_BTh_0^3q^2}{3\mu L_y}L_x\int_0^t H^2d\tau \\
&= \frac{k_BTh_0^3q^2}{3\mu L_y\omega(q)}L_x[e^{2\omega(q)t}-1].
\end{aligned} \tag{5.28}$$

Here we have used $\overline{\left|\widehat{N}\left(q,t\right)\right|^2} = L_x$, due to the finite length of the discrete Fourier transform used in MD simulations. Thus, we derive the spectrum of surface waves of bounded film flows as follows:

$$S = \left|\widehat{\delta h}\right|_{\text{rms}} = \sqrt{|\widehat{\delta h}(q,0)|^2 e^{2\omega(q)t} + \frac{k_B T h_0^3 q^2}{3\mu\omega(q)} \frac{L_x}{L_y}\left[e^{2\omega(q)t} - 1\right]}. \tag{5.29}$$

Here we use S to represent the spectra for notational simplicity. A similar expression for the surface wave spectrum can be found in Ref. [48, 51], but the derivation provided here is potentially more intuitive.

5.3 MD simulations of dewetting nanofilms

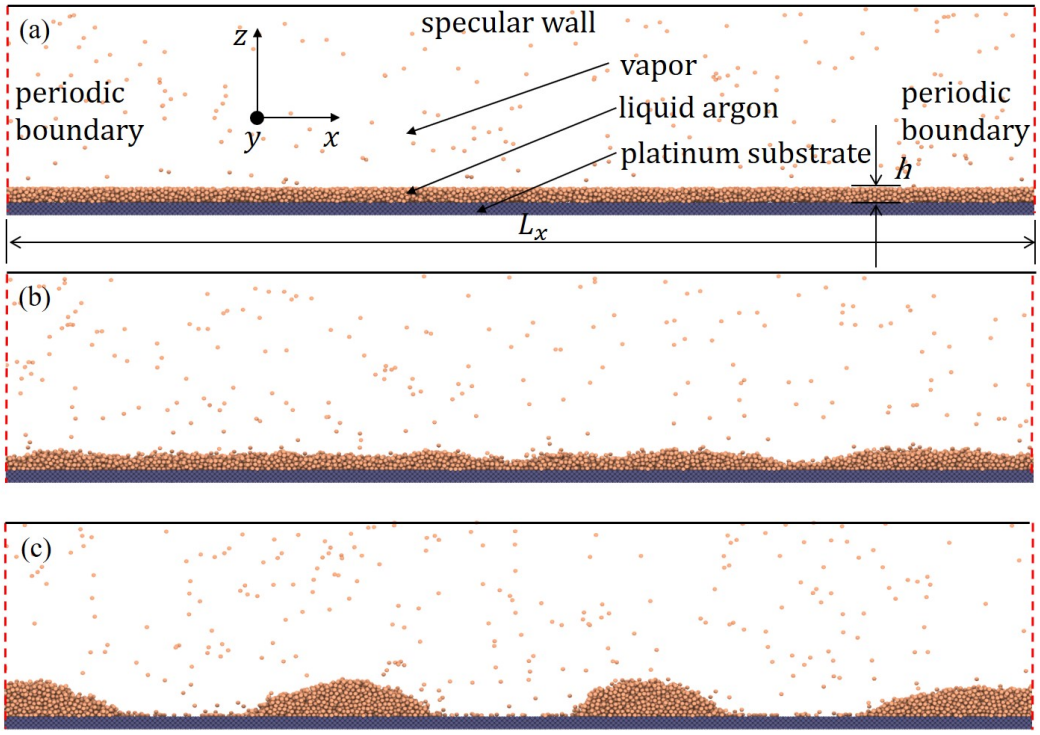

Figure 5.2: Snapshots of a section of a thin liquid film on a substrate simulated in MD; (a) initial configuration, (b) undulation growth, and (c) rupture. L_x is the film length and h is the film thickness (y is into the page).

MD simulations are used to simulate the rupture of a liquid film on a substrate. The domain contains three phases with the liquid bounded by the vapor above and the solid below, as shown in Fig. 5.2(a). The liquid of the film is ar-

gon and the substrate is platinum with a face centred cubic (fcc) structure and its $\langle 100 \rangle$ surface in contact with the liquid. The parameters of argon and platinum are detailed in Chapter 4. The liquid-solid interactions are modelled by the 12-6 LJ potential with $\varepsilon_{ls} = 0.7\varepsilon_{ll}$ and $\sigma_{ls} = 0.8\sigma_{ll}$, which creates partial wetting of argon on the substrate. After specifying the values of interactions, the Hamaker constants can be calculated. The A_{ll} is evaluated to be 4.5×10^{-20} J, from the expression $4\pi^2\varepsilon_{ll}\sigma_{ll}^6 n_l^2$ and A_{ls} is 2.61×10^{-20}J, from the expression $4\pi^2\varepsilon_{ls}\sigma_{ls}^6 n_l n_s$.

The initial dimensions of the liquid film (L_x, L_y, h_0) in Fig. 5.2(a) are chosen so that $L_x \gg L_y$, with $L_x = 313.90$ nm and $L_y = 3.13$ nm, making the 3D MD simulations quasi-2D, which allows us to consider large aspect ratio films and compare to 2D theories. Three cases with different film thickness $h_0 =$ (a) 1.18 nm, (b) 1.57 nm and (c) 1.96 nm are considered. Thus, L_x is also much larger than h, enabling the system to be described by lubrication (long-wave) theory. The lateral size of the substrate is the same as that of the liquid film and has a thickness $h_s = 0.78$ nm (composed of five layers of platinum atoms). The vapour above the liquid film has a thickness of 15.70 nm.

Based on the classical theory of instability (Eq. (5.5) & (5.6)), the critical wavelength ($\lambda_c = 2\pi/q_c$) and fastest growing wavelength ($\lambda_d = 2\pi/q_d$) are $\lambda_c = \sqrt{-4\pi^2\gamma/(\partial\phi/\partial h)}$ and $\lambda_d = \sqrt{-8\pi^2\gamma/(\partial\phi/\partial h)}$, respectively [19]. For the thickest film (case (c)) which has the largest critical wavelength and fastest growing wavelength, λ_c is evaluated to be 48.33 nm and $\lambda_d = 68.35$ nm. Thus the chosen length of the film L_x is long enough to contain multiple waves of the fastest growing wavelength for all the cases, and the chosen width of the film L_y is small enough to suppress any wave growth in the y direction for all the cases; ensuring the simulations remain quasi-2D.

We initialise each MD simulation as follows. Firstly, the liquid film and vapour are equilibrated separately in periodic boxes at $T^* = 0.7\varepsilon_{ll}/k_B$. The liquid film is then deposited on the substrate and the vapour on top of the film. After assembly, the positions and velocities of the liquid and vapour atoms are updated with a Nosé-Hoover thermostat. Periodic boundary conditions are applied in the x and y directions of the system whilst vapour particles are reflected specularly in the z direction at the top boundary of the system (see Fig. 5.2).

The position of the liquid-vapour interface is obtained using the method in Chapter 4. After determining the 2D interface, we average over the y direction (since these simulations are expected to be quasi-2D). Thus, the final interface is 1D and allows comparison with the 1D Planar-film SLE. After defining the interface $h(x,t)$, the undulations δh are obtained by subtracting the initial thickness h_0 from

h. Then we perform a discrete Fourier transform of the data and average over a number of realisations (70, 50 and 30 times for cases (a)-(c)) to obtain the spectra

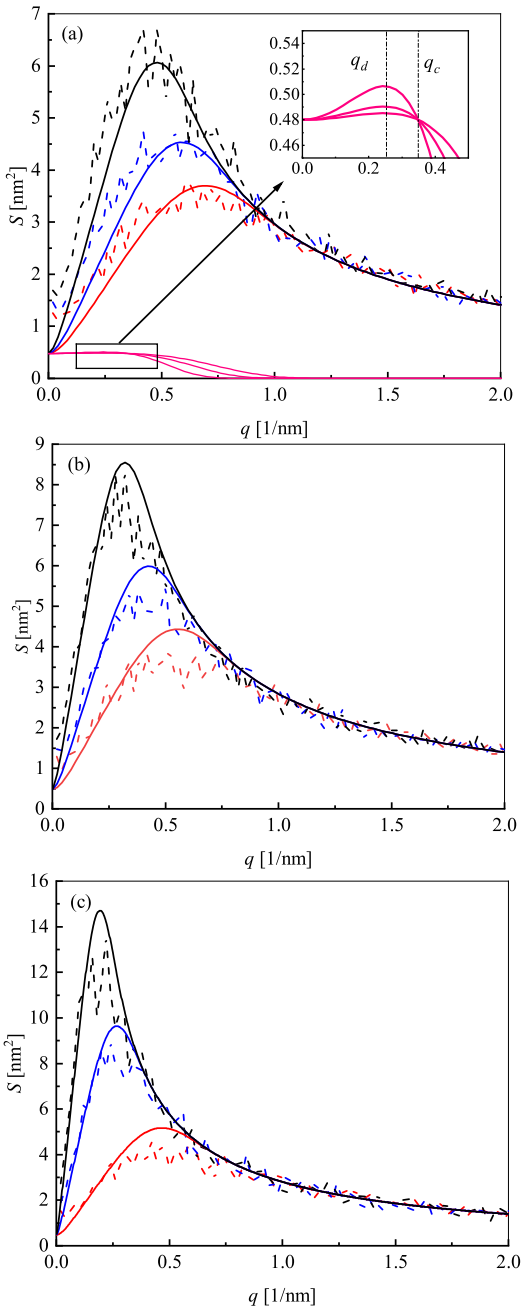

Figure 5.3: Spectra of MD simulations (dashed lines) and Eq. (5.29) (solid lines) at different times for (a) h_0=1.18 nm (t =0.086, 0.171, 0.428 ns); (b) h_0=1.57 nm (t =0.086, 0.257, 0.852 ns); and (c) h_0=1.96 nm (t =0.086, 0.857, 3.428 ns). The inset shows the deterministic spectrum for h_0=1.18 nm.

presented in Sec. 5.4.

5.4 Results and discussions

In this section, the surface undulation spectrum obtained from MD simulations is compared with the analytical spectrum derived above.

Figure 5.2 shows an MD simulation of a flat liquid film (case (a)), in which perturbations spontaneously grow (Fig. 5.2(b)) and subsequently rupture the film (Fig. 5.2(c)).

Figure 5.3 shows the rapidly growing amplitude of certain low wavenumber disturbances in MD simulations, which suggests that the rupture of these liquid films is mainly due to the spinodal instability. Notably, the analytical spectra (solid red lines in Fig. 5.3) compare very well with MD simulations. In Fig. 5.3(a), the inset shows the deterministic spectrum for $h_0 = 1.18$ nm. As can be seen, the amplitude of waves in the deterministic spectrum is far below that of MD results, showing that conventional models cannot be relied on at such scales. On the other hand, the stochastic spectrum agrees well with MD, suggesting thermal fluctuations substantially amplify the underlying instability and promote the rupture process.

The deterministic spectrum in the inset of Fig. 5.3(a) indicates that the dominant wavenumber q_d (wavenumber with peak amplitude) is constant over time, while both MD simulations and the stochastic spectra show clearly that this evolves. The dominant mode at different times is extracted from MD simulations and plotted in Fig. 5.4 (triangles) along with values obtained from the stochastic spectrum (solid red lines) and the deterministic spectrum (dashed black lines). The results demonstrate that thermal fluctuations induce a dominant wavenumber much higher than classical predictions and that this gradually decreases to the classical result over time; but in these cases, not before rupture of the film. It is also interesting to note that, while the stochastic spectra are strictly only valid in the early linear stages of the rupture process, the dominant wavenumber matches well with MD results even close to rupture.

Apart from wave amplitude and the dominant wavenumber, thermal fluctuations can also affect the critical wavenumber below which waves grow. From the classic theory, the critical wavenumber (wavelength) for the bounded film studied here is given by Eq. (5.5) and it is 0.35×10^9 (17.95 nm), 0.2×10^9 (31.41 nm), and 0.13×10^9 (48.33 nm) for cases (a)-(c) respectively. We perform here MD simulations with a film length considerably smaller (i.e conventionally stable): 13 nm, 24 nm and 36 nm for cases (a)-(c), respectively. Interestingly the result in Fig. 5.5, shows

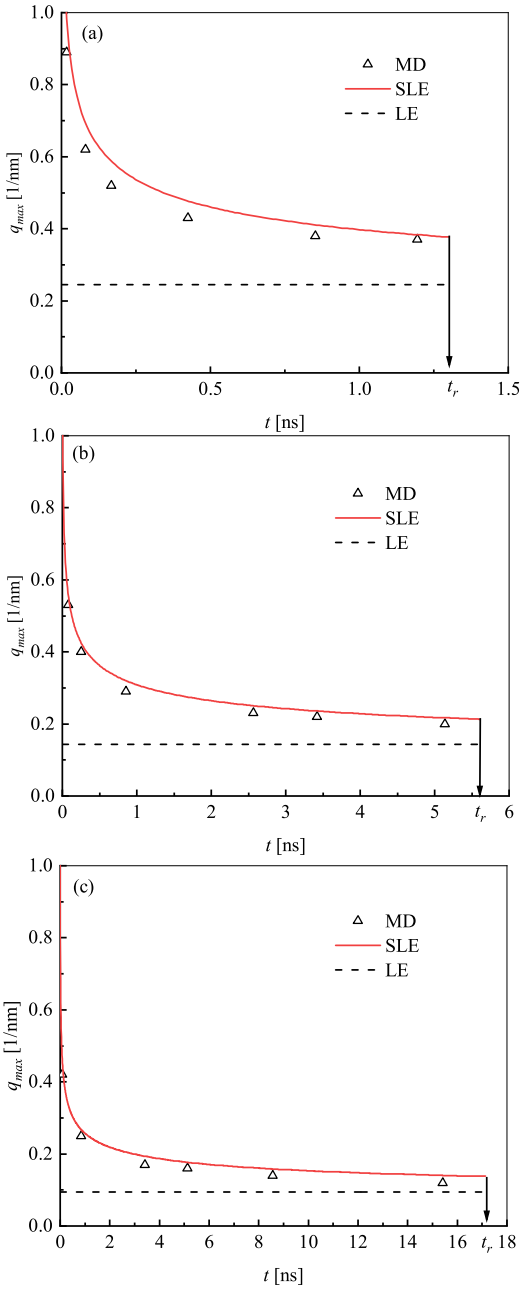

Figure 5.4: Dominant wavenumber as a function of time for (a) $h_0 = 1.18$ nm, (b) $h_0 = 1.57$ nm, (c) $h_0 = 1.96$ nm. Solid red lines are from the SLE, Eq. (5.29)). Triangular symbols are MD data and dashed black lines are from the deterministic LE, Eq. (5.6). t_r is the film rupture time when first dry-spot appears on the solid, averaged over a number of realisations (70, 50 and 30 times for cases (a)-(c)).

that a spontaneous rupture still occurs so that the critical wavenumber has been significantly altered. For example, the amplitude of q_c is not constant as expected

conventionally, but rather grows algebraically in time as

$$S_{q=q_c}(t) = \sqrt{\left\langle \left| \widehat{\delta h}(q_c, 0) \right|^2 \right\rangle + \frac{2}{3} \frac{L_x}{L_y} \frac{k_B T}{\mu} h_0^3 q_c^2 t}. \tag{5.30}$$

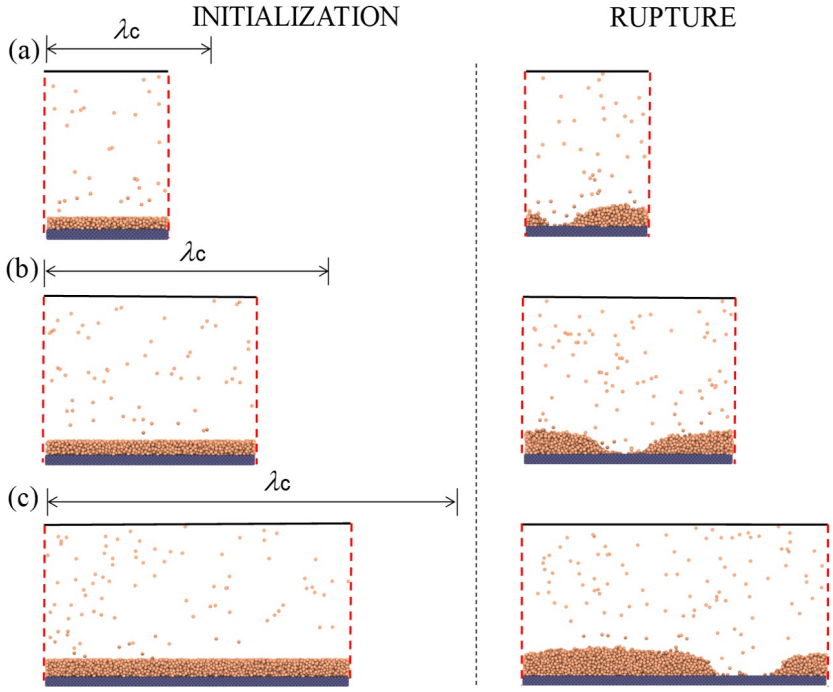

Figure 5.5: Rupture of three short films with their lengths inside classic critical wavelength λ_c in MD simulations (a) h_0=1.18 nm, (b) h_0=1.57 nm, (c) h_0=1.96 nm.

To identify wavenumbers which grow in time we consider the critical wavenumber $q_c^{'}$ to be defined by $\frac{\partial S}{\partial t}|_{q=q_c'} = 0$, i.e. the position at which the spectra are constant, and find that

$$q_c^{'2} = {q_c}^2 + \frac{k_B T}{\gamma} \frac{L_x}{L_y |\widehat{\delta h}(q, 0)|^2}, \tag{5.31}$$

where $|\widehat{\delta h}(q,0)|^2$ is from the initial condition of the film and $\frac{k_B T}{\gamma}$ is the square of the thermal length which premultiplies the new term due to thermal fluctuations. The expression indicates that, as observed in Fig. 5.5, thermal noise will increase the critical wavenumber, making liquid films of a certain thickness more susceptible to rupture by shorter-wave undulations. The parameters $|\widehat{\delta h}(q,0)| = 0.0977 \times 10^{-18}$ m^2, 0.1328×10^{-18} m^2, and 0.1625×10^{-18} m^2 are directly obtained from MD simulations for cases (a)-(c), respectively to find that $q_c' = 5.80 \times 10^9$ ($\lambda_c' = 1.08$ nm),

5.79×10^9 ($\lambda_c' = 1.08$ nm), and 5.79×10^9 ($\lambda_c' = 1.08$ nm). Therefore, it is seen that at the nanoscale the critical wavenumber can become independent of film height as thermal fluctuations (second term in Eq. (5.31)) overwhelm the conventional instability mechanism of disjoining pressure (first term in Eq. (5.31)). In this case, the new critical wavenumber depends on thermal fluctuations and the initial disturbance. Given the consistency between the MD results and the theoretical analysis, we can have some confidence that thermal fluctuations have the potential to rupture conventionally-stable film geometries.

5.5 Summary

Thermal fluctuations play an important role in different types of free-surface flow at the nanoscale. In this chapter, we investigate their effects on the instability of a thin liquid film on a substrate using MD simulations as an experimental probe, and analytically by solving stochastic thin film equation, to provide a deeper insight into the underlying physics. While thermal fluctuations are intrinsically captured in MD simulations, the SLE equation models these fluctuations using an appropriately scaled white noise. To facilitate the comparison between MD simulations and the SLE equation, we derive a stochastic spectrum of surface waves, and show close agreement between the analytical result and MD. By comparison with a deterministic (fluctuation-free) result, we conclude that thermal fluctuations are critical to the nature of the instability of nanoscale thin-film flows: they significantly intensify the amplitude of undulations, render the dominant wavenumber time-dependent, and decrease the critical wavelength. Thus, our work indicates that the consideration of thermal fluctuations is essential when investigating the behaviour of liquid films at the nanoscale.

A potentially related phenomenon occurs in the study of water transport in carbon nanotubes, where recent experiments show continuous flowing water in a channel tends to breakup and form a consecutive void-water structure [108], which may be due to thermal fluctuations. The current work reveals the effects of thermal fluctuations on the initial stages of instability growth. However, there are also abundant interesting flow dynamics in the later stages of the process where thermal fluctuations could play a role. For example, future research could consider the coarsening dynamics after the film has ruptured into droplets [109, 110].

Chapter 6

Thermal capillary wave growth and surface roughening

The well-known Capillary Wave Theory (CWT), which describes the capillary spectrum of the free surface of a liquid film at thermal equilibrium, does not reveal the transient dynamics of surface waves, e.g., the process through which a smooth surface becomes rough. Here, we use the SLEs and Langevin model developed in Chapter 3 to resolve this problem and study the effects of slip on the evolution of thermal capillary waves (TCWs).

This chapter is organised as follows. In Sec. 6.1, the time-dependent spectra obtained from the SLEs and the Langevin model are presented. In Sec. 6.2, the molecular configuration for nanoscale liquid films on substrates (plates and fibres) is presented; these simulations will be used as virtual nanoscale experiments, against which new theories will be validated. The slip length used in the analytical solutions is obtained from independent MD simulations, and details of how these are performed are also given. Sec. 6.3 compares the new theories with MD results and previous experiments, and discusses new findings. In Sec. 6.4, we summarise the main contributions of the chapter and outline exciting future directions for this research.

6.1 Time-dependent TCW spectra

6.1.1 TCW spectra obtained from SLEs

Using the linear stability analysis method in Chapter 5, we obtain time-dependent spectra from the Planar-film SLE and Annular-film SLE (both with slip). We do not consider disjoining pressure here as disjoining pressure will lead to the rupture

of films, which is beyond the scope of the classic CWT, where films are expected to be stable at rest (at least for planar films).

With the Planar-film SLE (Eq. (3.39)), the transient spectrum for planar films is

$$S_1(q,t) = \sqrt{\left\langle \left|\widehat{\delta h}(q,0)\right|^2 \right\rangle e^{-2\Omega_{\mathrm{LW},1}(q)t} + \frac{L_x}{L_y}\frac{k_BT}{\gamma q^2}\left[1 - e^{-2\Omega_{\mathrm{LW},1}(q)t}\right]}. \tag{6.1}$$

The explicit expression for Ω is shown earlier in Chapter 3. As we are interested in how thermal fluctuations roughen a surface (i.e., the evolution of a non-equilibrium surface to its thermal equilibrium), the initial condition of the surface is assumed to be smooth $\langle\left|\widehat{\delta h}(q,0)\right|^2\rangle = 0$. As we will see, a smooth interface allows us to extract the maximum time for a non-equilibrium liquid surface to reach its thermal equilibrium, which provides a useful guideline either for computational or experimental investigation of non-equilibrium surfaces. Assuming the initial surface is smooth, Eq. (6.1) is simplified to

$$S_1(q,t) = \sqrt{\frac{L_x}{L_y}\frac{k_BT}{\gamma q^2}\left[1 - e^{-2\Omega_{\mathrm{LW},1}(q)t}\right]}. \tag{6.2}$$

For an annular film, the time-dependent spectrum derived from the Annular-film SLE (Eq. (3.64)) is

$$S_2(q,t) = \sqrt{\left\langle \left|\widehat{\delta h}(q,0)\right|^2 \right\rangle e^{-2\Omega_{\mathrm{LW},2}(q)t} + \frac{L_x}{2\pi h_0}\frac{k_BT}{\gamma(q^2 - 1/h_0^2)}\left[1 - e^{-2\Omega_{\mathrm{LW},2}(q)t}\right]}. \tag{6.3}$$

With an initially smooth surface, Eq. (6.3) becomes

$$S_2(q,t) = \sqrt{\frac{L_x}{2\pi h_0}\frac{k_BT}{\gamma(q^2 - 1/h_0^2)}\left[1 - e^{-2\Omega_{\mathrm{LW},2}(q)t}\right]}. \tag{6.4}$$

6.1.2 TCW spectra from the Langevin model

From the Langevin model, Eq. (3.83), the TCW spectra can also be immediately obtained using the linear-stability-analysis method in Chapter 5, since a SLE is a type of Langevin equation after linearisation (see Eq. (5.19)). The transient TCW spectrum from the Langevin model is

$$S(q,t) = \sqrt{\left\langle \left|\widehat{\delta h}(q,0)\right|^2 \right\rangle e^{-2\Omega(q)t} + S_{\mathrm{s}}^2\left(1 - e^{-2\Omega t}\right)}. \tag{6.5}$$

Again, we assume the initial condition for the surface is smooth so that Eq. (6.5) becomes

$$S(q,t) = S_{\mathrm{s}}\sqrt{1-e^{-2\Omega t}}. \tag{6.6}$$

Thus, one can see that the power of this Langevin model is its generality: to find the time-dependent spectrum for the linear treatment of any Stokes-flow film, all that is required is to substitute the appropriate static spectra and dispersion relation into Eq. (6.6). For example, substituting Eq. (3.80) and Eq. (3.85) into Eq. (6.6) generates exactly the spectra derived from the Planar-film SLE, namely, Eq. (6.2). It also offers the opportunity of improving on such SLE predictions by adopting more accurate dispersion relations, such as those utilising Stokes flow (see Appendix B for the derivation of the Stokes dispersion relation for annular films), or adding additional physics without having to always return to the full equations of FH, and performing an asymptotic analysis.

6.2 MD simulations

6.2.1 Settings of films on slippery plates and fibres

To demonstrate the growth of TCWs, MD simulations of films on plates and fibres are performed, as shown in Fig. 6.1. The film is composed of liquid argon and kept at a constant temperature $T = 85$ K. For a planar substrate, the solid is platinum made of five layers of atoms, with a face centred cubic (fcc) structure and its $\langle 100 \rangle$ surface in contact with the liquid. For cylindrical substrates, Fibre 1 and Fibre 2 are used, which are described in Chapter 4. The liquid-solid interactions are modelled by the 12-6 LJ potential with $\sigma_{ls} = 0.8\sigma_{ll}$ for the length parameter. For planar films, three different values of the energy parameter are used, in order to generate varying slip lengths: Case (P1) $\varepsilon_{ls} = 0.65\varepsilon_{ll}$, Case (P2) $\varepsilon_{ls} = 0.35\varepsilon_{ll}$ and Case (P3) $\varepsilon_{ls} = 0.20\varepsilon_{ll}$. For annular films and Fibre 1, Case (A1) $\varepsilon_{ls} = 0.7\varepsilon_{ll}$; for Fibre 2, Case (A2) $\varepsilon_{ls} = 0.6\varepsilon_{ll}$.

The initial dimensions of a planar liquid film (see Fig. 6.1(a)) are $L_x = 313.90$ nm, $L_y = 3.14$ nm and $h_0 = 3.14$ nm; the MD simulations are quasi-2D ($L_x \gg L_y$) allowing comparison with 2D theory. The initial size of the annular film (see Fig. 6.1(c)) has film length $L_x = 229.70$ nm and outer radius $h_0 = 5.74$ nm. The radius of Fibre 1 is defined by the radius of cylinder, $a_1 = 2.35$ nm, used to cut the fibre out of a bulk cube of platinum. Fibre 2 has an outer radius $a_2 = 2.17$ nm, with spacing 0.22 nm from the inner ring. Solid particles are distributed uniformly with 5° spacing.

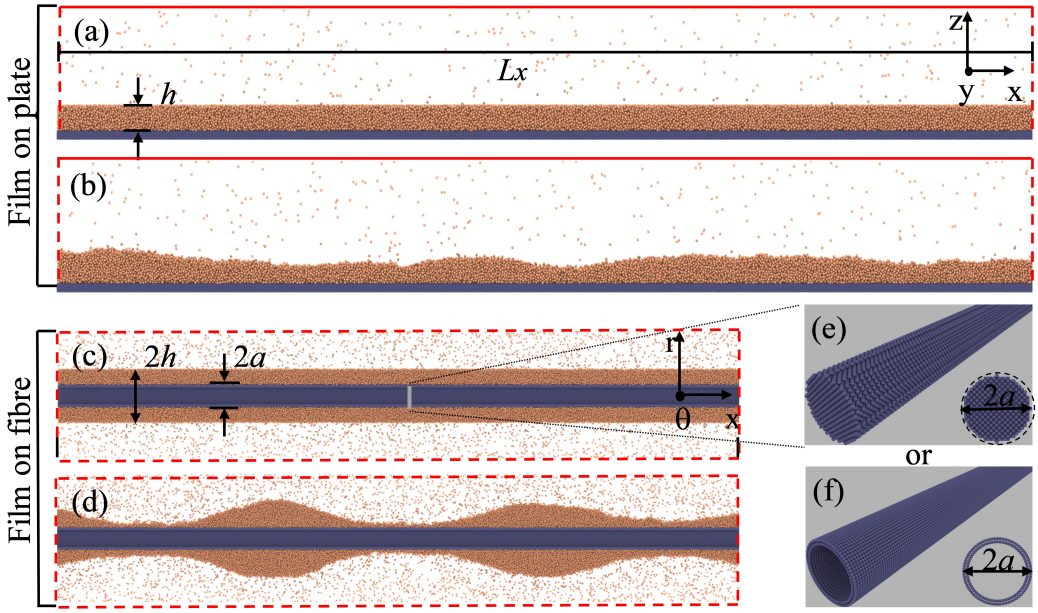

Figure 6.1: Snapshots of a thin liquid film (a section) on a substrate in MD. For planar films, (a) initial configuration with a smooth surface; (b) surface roughening. For annular films, (c) initial configuration; (d) beads formed due to the Rayleigh-Plateau instability. Two types of cylindrical substrates are used: (e) Fibre 1, cut out from a bulk of Platinum with fcc structure. (f) Fibre 2, consisting of two concentric surfaces. L_x is the film length, h is the film thickness for a planar film and film radius for an annular film, and a is the fibre radius (y and θ are into the page).

Notably, the film thickness for both planar films and annular films are chosen to be much larger than the cut-off distance so that disjoining pressure can be ignored [111].

For the planar case, we separately equilibrate a liquid film with thickness $h_0 = 3.14$ nm and a vapour in periodic boxes at $T = 85$ K. The film is then deposited above the substrate and the vapour is placed on top of the film. Because there exists a gap (a depletion of liquid particles) between the solid and liquid, arising from the repulsive force in the LJ potential, it is necessary to deposit the liquid above the substrate by some distance. The thickness of the gap is found to be about 0.2 nm after the liquid-solid system reaches equilibrium so that we choose a deposit distance $d = 0.2$ nm. This makes the initial position of the film surface at $z = h_0 + d = 3.34$ nm if the substrate surface has position at $z = 0$.

For an annular film, cuboid boxes of liquid and vapour are equilibrated separately in periodic boxes at $T = 85$ K. Then an annular film is cut out from the cuboid box with the outer radius at 5.74 nm and inner radius above the fibre radius

with an interval 0.2 nm. Then the fibre is put into the annular film and vapour is placed to surround the film. Notably, in this case, the position of film surface is still at $h_0 = 5.74$ nm, initially.

Periodic boundary conditions (PBC) are applied in the x and y directions of a planar system whilst vapour particles are reflected specularly in the z direction at the top boundary of the planar system. For annular films, PBC are applied in all three directions. After initialisation of the simulated systems, the positions and velocities of the liquid and vapour atoms are updated with a Nosé-Hoover thermostat (keeping the temperature at $T = 85$K) and the boundary conditions detailed above.

6.2.2 Measurements of slip length

Slip length is measured from independent configurations by simulating pressure-driven flow past a substrate surface as shown by the MD snapshots in the top-left corner of Fig. 6.2(a) (for a planar film) and Fig. 6.2(c) (for an annular film). The pressure gradient is created by applying a body force g to the fluid. The generated velocity distribution is $u(z) = \frac{\rho g}{2\mu}(z - z_1)(2z_2 - z_1 - z) + u_s$ for a planar film. Here z_1 and z_2 are positions of the hydrodynamic boundary (HB) and free surface (FS) for a planar film, respectively, and u_s is the slip velocity at the HB. For an annular film, the axisymmetric velocity profile is $u(r) = -\frac{\rho g}{4\mu}\left[r^2 - r_1^2 - 2r_1^2 \log(r/r_2)\right] + u_s$, where r_1 and r_2 are positions of the HB and FS for this system.

The precise location of two boundary positions for each system is not trivial since there is an interfacial zone between the two different phases (solid-liquid and liquid-vapour) as demonstrated by the density distribution (the orange line in Fig. 6.2(a) and the inset of Fig. 6.2(c)). For the HB, research has shown that it is located inside the liquid, between first-peak density and second-peak density rather than being located at the solid surface [65, 69]; this is found by comparing the analytical solution and MD measurements of the correlations of momentum density. In line with this finding, we choose the position of HB at the first valley of density distribution: $z_1^* = 1.3\sigma$ for a planar film and $r_1^* = 7.65\sigma$ for an annular film (see Figs. 6.2(a) and 6.2(c)). The position of FS is determined in the standard way by the location of equimolar surface where density is $0.5n_l^*$, with $z_2^* = 9.8\sigma$ for a planar film and $r_2^* = 16.55\sigma$ for an annular film (see Figs. 6.2(a) and 6.2(c)).

After locating the boundary, the slip velocity is obtained by fitting velocity profiles of MD data (symbols) with analytical expressions of velocity (solid black lines) as shown in Fig. 6.2(a). The slip length ℓ is the distance between the HB and the position where the the linear extrapolation of the velocity profile vanishes. Figure 6.2(a) is, in particular, for case P2 where the slip length is measured to be

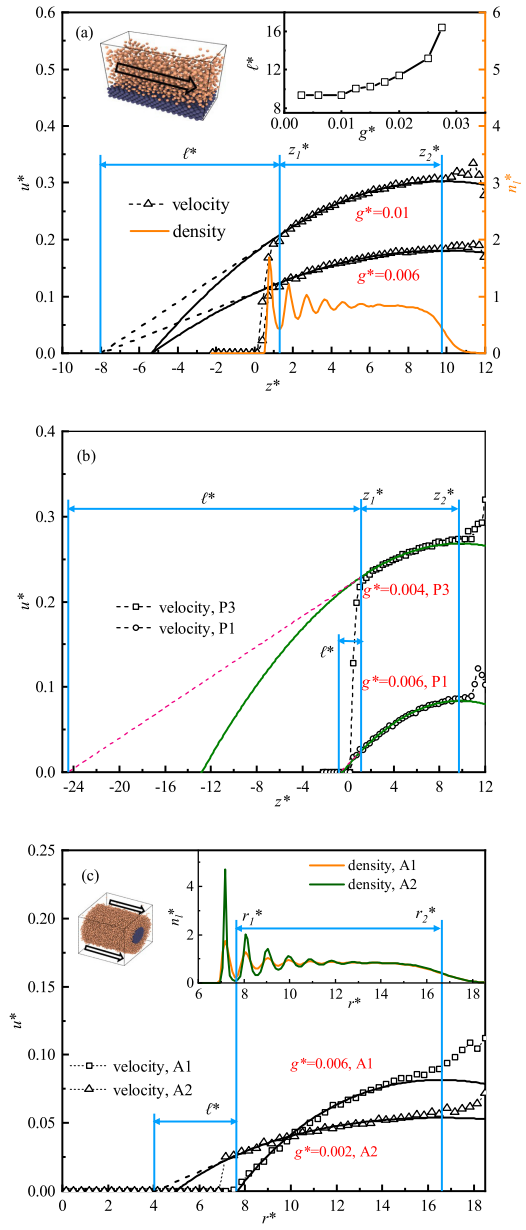

Figure 6.2: Slip length measured using pressure-driven flows. Figures (a-b) are for planar films with (a) for case P2 and (b) for case P1 and P3. MD calculations of velocity (triangles) are fitted with analytical solutions (black solid lines) with the HB (z_1) at the first valley of MD density (yellow solid line) and FS (z_2) at $0.5n_l^*$. The inset shows slip length as a function of driving force. Figure (c) is for annular films, case A1 and A2. The inset shows the density profile.

$\ell^* = 9.3\sigma$ (3.16 nm) ($\ell = 0.68$ nm for P1 and $\ell = 8.77$ nm for P3, see Fig. 6.2(b)). In Fig. 6.2(a), two different values of driving forces $g^* = 0.01$ and $g^* = 0.006$ are used

to prove that the measured slip length is a constant independent of driving forces ($g^* \leq 0.01$). However, as the inset shows, the slip length becomes shear-dependent for $g^* \geq 0.01$, which is beyond current consideration [68]. As the driving forces in the free-surface flows studied for capillary waves are small, the assumption of a constant slip length holds.

For annular films, as shown in Fig. 6.2(c), the slip lengths are $\ell = 0$ nm (no-slip) for case A1 and $\ell = 1.18$ nm for A2. Similar to the planar cases, we make sure that the slip lengths for annular cases are constant independent of driving force strength.

We note that as the HB does not align with the edge of the solid, the effective thickness of the fluid domain simulated for capillary waves is different to its initial thickness. For a planar film, as the position of the initial free-surface is at 3.34 nm and the HB is at $z_1 = 0.44$ nm, the effective thickness of a planar film is 2.9 nm. For an annular film, this means $a = r_1 = 2.6$ nm and outer radius h_0 is 5.74 nm.

6.3 Results and discussions

As the film thickness is larger than the cut-off distance, there is no disjoining pressure at the free surface. According to classical theory, the surface of the initially smooth planar film, Fig. 6.1(a), should thus remain smooth indefinitely. However, thermal fluctuations generate surface roughness over a period of time, see Fig. 6.1(b), and it is the evolution of this roughness that we study here. The situation for the annular film is more complex, since, as seen in Fig. 6.1(d), it can be prone to a Rayleigh-Plateau instability, due to the 'pinching' surface tension force generated by the circumferential curvature.

6.3.1 Spectra of planar films

We now compare the proposed Langevin model directly to MD data. Figures 6.3(a-c) show spectra of (long) planar films with three different slip lengths. The first thing we note is that the spectra are, indeed, time dependent, and only gradually approach the static spectrum. One can see that the transient characteristics of the spectra are strongly influenced by the slip length, which is controlled in the MD indirectly by the solid-liquid interaction potential (Sec. 6.2 provides details on how this parameter, and the effective film thickness, are extracted from independent MD simulations for use in the Langevin model, see the caption of Fig. 6.3 for values).

From Figs. 6.3(a-c), the MD spectra compare remarkably well with the Langevin model when a Stokes-flow approximation to the dispersion relation is

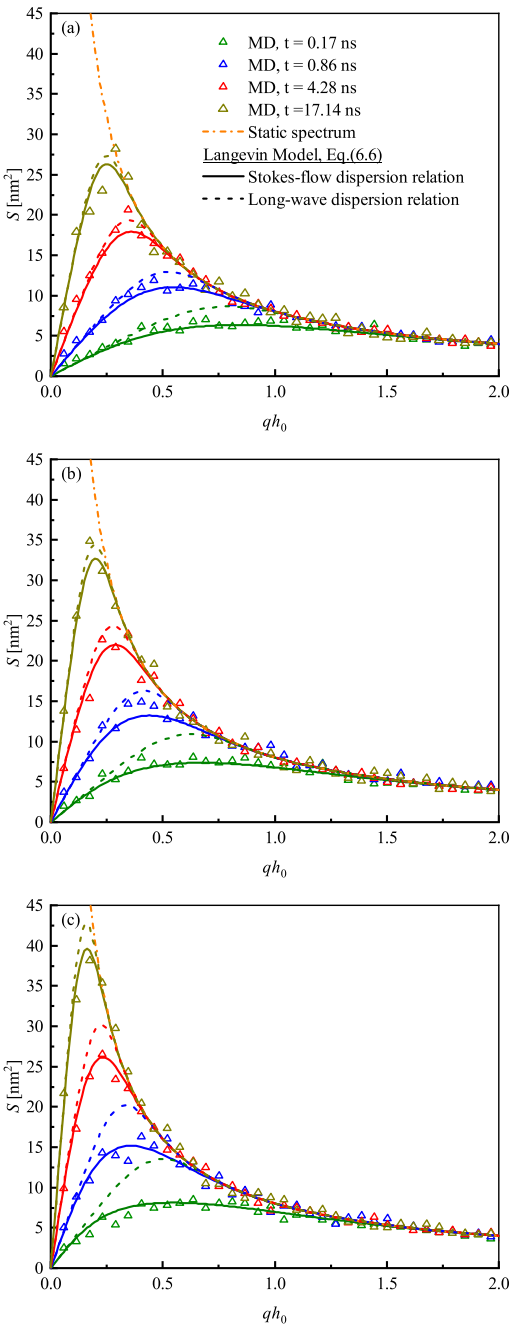

Figure 6.3: Evolution of capillary spectra of a (long) planar film for increasing slip length. A comparison of spectra extracted from MD results (triangles), and Langevin model with Stokes-flow dispersion relation (solid lines) or with long-wave dispersion relation (dash lines) at four different times, along with the static spectrum (dash-dot line). (a) $\ell = 0.68$ nm, (b) $\ell = 3.16$ nm, (c) $\ell = 8.77$ nm. The effective thickness of the film $h_0 = 2.90$ nm and film length is 313.9 nm.

adopted (solid lines) for all slip lengths and at all times. In contrast, the Langevin model with a dispersion relation derived from a long-wave approximation (dashed lines) – equivalent to the Planar-film SLE – is only accurate (i) when slip lengths are small relative to the film thickness (i.e. not for the case in Fig. 6.3(c)) and (ii) only in the later stages of capillary wave growth where the dominant (dimensionless) wavenumber $q_d h_0$ (the one with peak amplitude) becomes much smaller than unity (i.e. when the wavelength becomes large), as discovered and detailed in [90]. Thus, the new Langevin model developed here allows us to go beyond the long-wave paradigm.

The dominant wavenumber is seen to decrease with time and q_d can be estimated from the dynamic spectrum Eq. (6.6), by finding the spectrum's maximum, $\partial S/\partial q|_{q=q_d} = 0$:

$$1 - e^{-2\Omega(q)t} - q\frac{d\Omega\left(q\right)}{dq}te^{-2\Omega(q)t} = 0. \tag{6.7}$$

Adopting the long-wave approximation for the dispersion relation Eq. (3.80), one can obtain

$$1 - e^{-2\Omega_{\mathrm{LW},1}(q)t} - 4\Omega_{\mathrm{LW},1}\left(q\right)te^{-2\Omega_{\mathrm{LW},1}(q)t} = 0. \tag{6.8}$$

The non-zero root of Eq. (6.8) is

$$\Omega_{\mathrm{LW},1}\left(q\right)t \approx \frac{15}{8} \tag{6.9}$$

Using the explicit expression for the $\Omega_{LW,1}$ allows analytical results to be obtained:

$$q_d \cong \left[\frac{15}{8}\frac{\mu}{\gamma(3\ell h_0^2 + h_0^3)}\right]^{\frac{1}{4}} t^{-\frac{1}{4}}. \tag{6.10}$$

As can be seen from Fig. 6.4, this prediction agrees well with the MD results.

6.3.2 Roughness of planar films and their universality class

For the free surface considered here, the roughness of the film, W, can be defined in terms of the evolving surface spectrum from Parseval's theorem:

$$W(t) = \sqrt{\frac{1}{L_x}\left\langle \int_0^{L_x} (\delta h)^2\, dx \right\rangle} = \sqrt{\frac{1}{2\pi L_x}\int_{q_{min}}^{q_{max}} S^2\, dq}\,, \tag{6.11}$$

where $q_{min} = 2\pi/L_x$ is usually defined by the domain size L_x. The $q_{max} = 2\pi N_b/L_x$ and N_b is the number of bins used to extract the surface profile from MD simulations, which provides an upper bound on the wavenumbers that can be extracted.

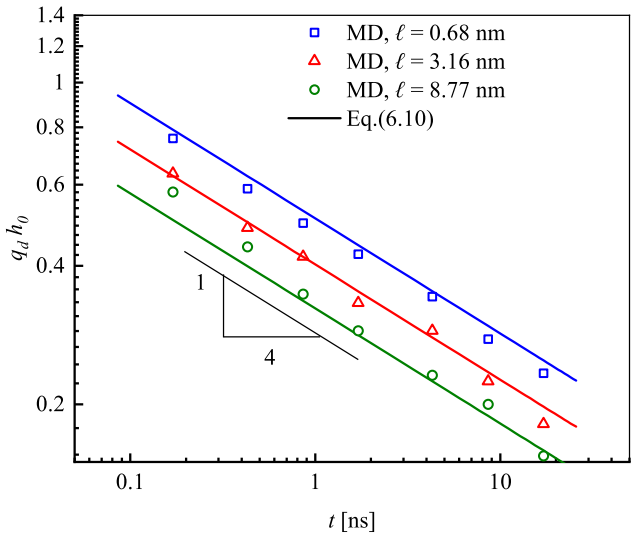

Figure 6.4: Decrease of the dominant wavenumber as a function of time.

A quick inspection of the MD results presented in Fig. 6.5 (symbols) reveals that, approximately, the roughness grows with some power law in time, which motivates the use of scaling relations (see the literature review in Chapter 2) to study surface roughening, as considered previously for the interface roughening between two immiscible inviscid gases [112]. In other words, this opens up the remarkable possibility of obtaining a simple parametrisation for this complex roughening process that aligns the process to seemingly unrelated physical phenomena.

Scaling relations for surface roughness can be summarized by [63]

$$W \sim L^{\alpha} f(t/L^{m}), \tag{6.12}$$

where L is the system size, $f(v) = v^{\kappa}$ for $v \ll 1$ (during roughness growth), and $f(v) = 1$ for $v \gg 1$ (at roughness saturation; which is not reached in the MD results of Fig. 6.5). The time to transition, between roughness growth and saturation, scales with $t_s \sim L^m$. The three exponents (α, m and κ) define a universality class, and are here related by $\kappa = \alpha/m$.

For the planar film, α can be obtained by considering the surface at saturation, i.e. from the static spectrum given in Eq. (3.85). Substituting Eq. (3.85) into Eq. (6.11) leads to

$$W_s = \sqrt{\frac{1}{2\pi L_y}\frac{k_B T}{\gamma}\left(\frac{L_x}{2\pi} - \frac{L_x}{2\pi N_b}\right)}. \tag{6.13}$$

For large N_b, which is the case in our MD simulations, W_s becomes independent of

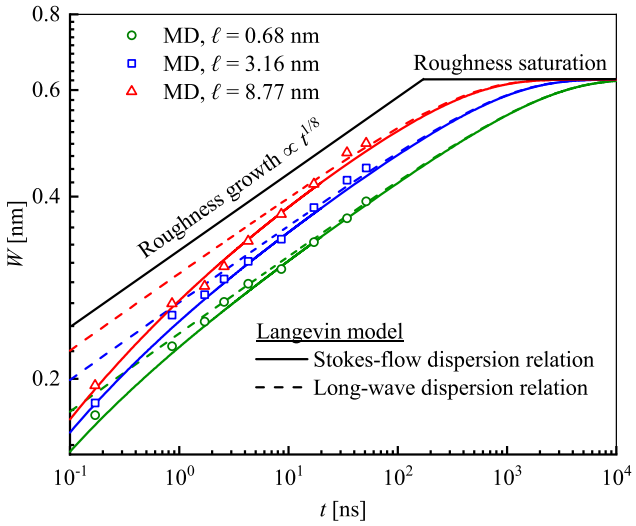

Figure 6.5: Slip effects on surface roughening of a planar film. The comparison is made among MD results (symbols), Langevin model with Stokes-flow dispersion relation (solid lines) or with long-wave dispersion relation (dash lines).

N_b, and one can find that $W_s = \sqrt{\frac{L_x}{4\pi^2 L_y}\frac{k_B T}{\gamma}} \sim {L_x}^{1/2}$ assuming L_y is fixed.

An upper estimate on the transition time, between growth and saturation, can be estimated from the inverse of the dispersion relation at the largest permissible wave length ($q = 2\pi/L_x$). For this it is reasonable to use the long-wave approximation, Eq. (3.80), to find

$$t_s = \frac{3\mu L_x^4}{16\pi^4\gamma(h^3 + 3\ell h^2)}, \tag{6.14}$$

so that $t_s \sim {L_x}^4$, and thus $W(t) \sim t^{1/8}$. In summary, we find the exponents $\alpha = 1/2$, $m = 4$ and $\kappa = 1/8$, assuming, as we have done, long-wave dominated roughness.

The MD results in Fig. 6.5 indicate that, indeed, $W \sim t^{1/8}$; this scaling is more apparent at later times, but before saturation, when the roughness is characterised by long wavelengths. This precise scaling, as well as the anticipated roughness saturation, is confirmed by the Langevin model with a long-wave approximation to the dispersion relation (dashed lines). A closer agreement with MD at earlier times, when the roughness has a shorter characteristic wavelength, is provided by a Stokes-flow dispersion relation (solid lines), but this model does not permit the simple extraction of power laws. The results also show that enhanced slip accelerates the roughening of the surface, but does not alter the final saturated value.

Interestingly, the new analysis enables us to see that the exponents we find for the surface roughening of a planar film using the long-wave dispersion relation

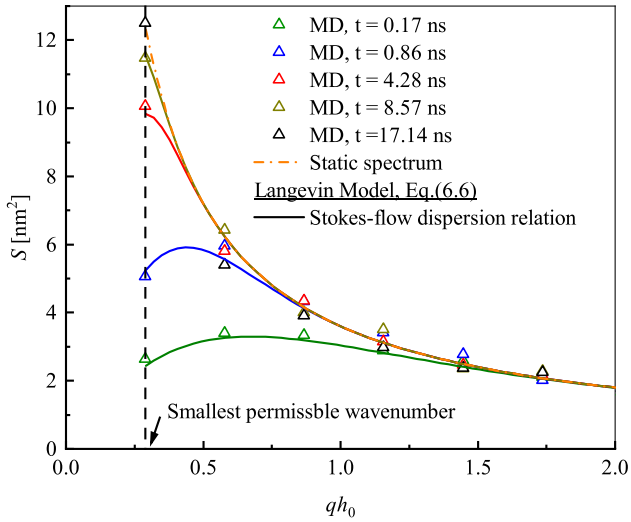

Figure 6.6: A complete evolution of the capillary spectra to the static spectrum. The film length is 62.78 nm.

(i.e. the planar-film SLE by [5, 90]) are the same with those for surface roughening of atomic depositions in molecular beam epitaxy (MBE) [63]. Thus the two distinct physical problems belong to the same universality class (1/2, 4, 1/8).

The strong dependency of the transition time on domain length ($t_s \sim L_x^4$) which we have uncovered, explains why in our simulations for a film length $L_x = 313.9$ nm this time is of the order of microseconds (see Fig. 6.5) and is thus impossible to resolve in MD. For example, for case P2, the transition time $t_s = 1/|\Omega| = 3389.3$ ns using the long-wave dispersion relation and $t_s = 3458.5$ ns using the Stokes-flow dispersion relation, evaluated at the smallest permissible wavenumber, $q = 2\pi/L_x$. However for a shorter film with film length 62.78 nm (other parameters are the same with P2), the transition time is $t_s = 5.4$ ns with the long-wave dispersion relation and $t_s = 8.2$ ns with the Stokes-flow dispersion relation (with better accuracy). Note that the growth of wave amplitude means the increase of surface free energy, which comes from the constant-temperature used in MD simulations. Thus, the complete evolution of capillary waves to the static capillary wave can be realised in MD simulations, which is shown in Fig. 6.6, but our results have highlighted that care should be taken when interpreting results for larger film lengths where reaching thermal equilibrium (the static spectrum) for the surface is often computationally intractable.

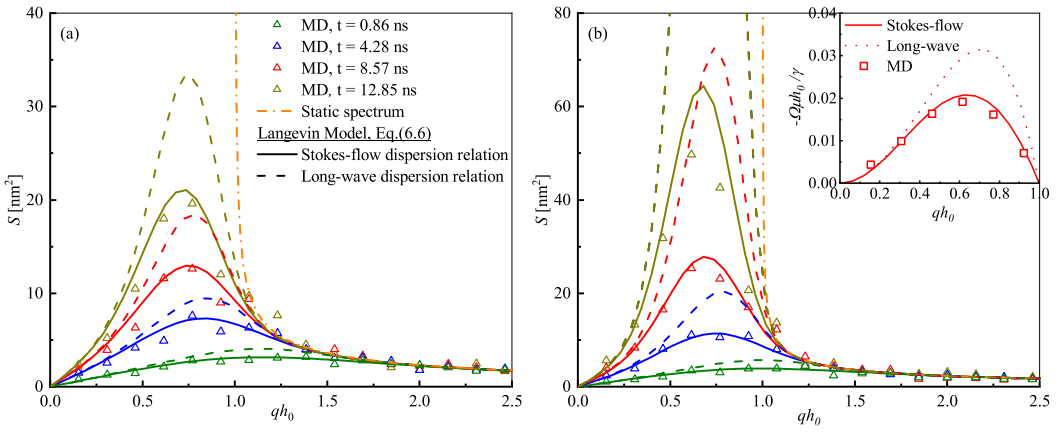

Figure 6.7: Evolution of capillary spectra for annular films; a comparison between MD results (triangles), the static spectrum (dashed and dotted line) and the Langevin model. Dispersion relations used in the Langevin model assuming Stokes flow (solid lines) and a long-wave approximation (dashed lines). Slip lengths (a) Fibre 1, $\ell = 0$; and (b) Fibre 2, $\ell = 1.18$ nm. The hydrodynamic boundary is at radius $a = 2.60$ nm and the initial surface at $h_0 = 5.74$ nm (see sec.6.2 for measurement details).

6.3.3 Spectra of annular films

Figure 6.7 shows the evolving spectra of the capillary waves of annular films. For wavenumber $qh_0 > 1$, the MD spectra (triangles) of different times collapse onto the static spectrum, Eq. (3.86). However, for $qh_0 < 1$, the Laplace pressure from the circumferential curvature results in a negative dispersion relation such that the amplitude grows unboundedly until the film ruptures and beads are formed (seen in Fig. 6.1(d)).

The surprise finding discussed earlier is that the noise amplitude in the Langevin model appears independent of whether CWT (which assumes disturbances are saturated) or a long-wave approximation (which does not) is adopted. It is therefore interesting to see that the Langevin model compares closely to the MD simulation for the annular film, particularly in unstable regions of the spectra. Note, while the noise amplitude seems independent of the long-wave approximation, the dispersion relation is not, see the inset of Fig. 6.7(b); hence the improved agreement when adopting the Stokes-flow dispersion relation, particularly in Fig. 6.7(b), which is rather dramatic in the annular case.

Though the Annular-film SLE (equivalent to the Langevin model with a long-wave dispersion relation) overpredicts the spectra amplitude currently, its accuracy can be improved for larger a/h_0 (the ratio of the fibre radius to the total thickness),

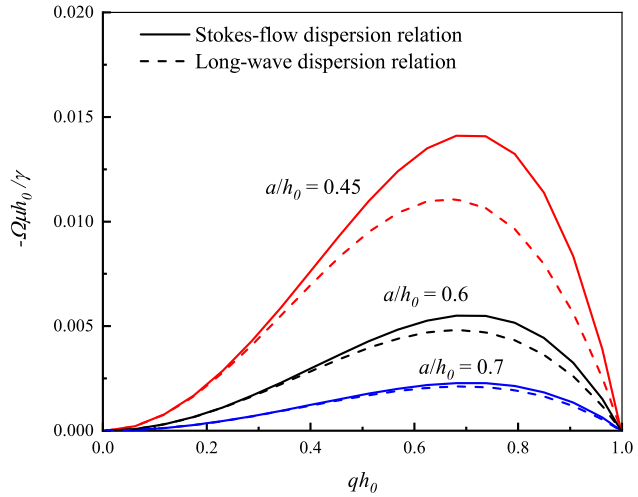

Figure 6.8: Variation of the dispersion relation as a function of a/h_0. The lager a/h_0 means thinner films compared to the fibre radius.

namely thinner films compared to the fibre radius. Currently, $a/h_0 = 0.45$. For the no-slip case, we plot the dependence of the dispersion relation (Stokes and long-wave) on a/h_0 in Fig. 6.8, which shows that the long-wave dispersion relation compares well with the Stokes-flow dispersion relation for $a/h_0 \geq 0.6$. Thus, the Annular-film SLE with large a/h_0 is a good model to predict the stochastic dynamics of annular films.

As with the dominant wavenumber for a planar film, the dominant wavenumber for an annular film also decreases with time but approaches a constant value which is $q_{dc}h_0 = \sqrt{2}/2$ from a linear stability analysis of the Annular-film LE. It is interesting to know at what time scale the q_d reaches the constant value q_{dc}. By requiring $\frac{\partial S_2}{\partial t} = 0$ from Eq. (6.4), we obtain

$$2e^{2\Omega_{LW,2}(q_d)t}\Omega_{LW,2}(q_d)t\left[2 - 1/(q_d h_0)^2\right] + 1 - e^{2\Omega_{LW,2}(q_d)t} = 0. \tag{6.15}$$

When $q_d h_0$ is close to $\sqrt{2}/2$, this expression is simplified to

$$(q_d h_0)^2 \cong (q_{dc}h_0)^2 + \frac{\mu h_0^5}{2\gamma G(h_0)}\frac{1}{t}. \tag{6.16}$$

Thus, the time scale for the dominant wavenumber to reach $q_{dc}h_0 = \sqrt{2}/2$ is $\frac{\mu h_0^5}{\gamma G(h_0)}$. However, it is not feasible to extract the dominant wavenumber from current MD simulations to confirm Eq. (6.16), as the number of data points is too sparse, as shown in Fig. 6.7. One would need to simulate a much longer film to have data

dense enough to verify Eq. (6.16), and the computational cost of this is currently prohibitively high.

6.3.4 Connections with experiments

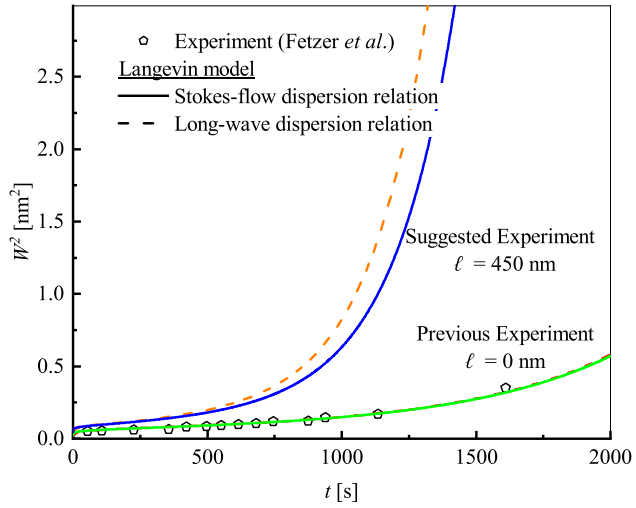

Figure 6.9: Slip effects on surface roughening of a dewetting planar film. A comparison is made between our Langevin model and previous experiments [52] of a rupturing film without slip but with effects of disjoining pressure. A further experiment with large slip is suggested.

Using the parameters found in experiments of polymer systems considered in [59–61] where a static spectrum has to be presupposed, we calculate the transition time to be hours long – it is therefore not immediately clear that the assumption of saturation is justified, and this should be confirmed before analysing experimental data.

Fetzer *et al.* [52] presented experiments of dewetting polymer films and compared the experimental data with the *no-slip* Planar-film SLE [5, 51] to investigate the effects of thermal fluctuations on thin-film dewetting. The high viscosity of experimental liquids makes the time scales for instability growth so slow that AFM can be used to provide spatio-temporal observations. One of the variables they analysed is the roughness of the film surface in experiments, with which we can compare our developed Langevin model.

In their experiments, the dewetting is influenced by disjoining pressure so that the capillary spectrum from Langevin model is slightly modified to consider

disjoining pressure ϕ:

$$S(q,t) = \sqrt{S^2(q,0)e^{-2\Omega t} + L^2 \frac{k_B T}{\gamma q^2 + d\phi/dh\,|_{h_0}} (1 - e^{-2\Omega t})}. \tag{6.17}$$

Here $\phi = \frac{A}{6\pi h_0^3}$ and A is the Hamaker constant. The long-wave dispersion relation considering slip and disjoining pressure is

$$\Omega'_{\mathrm{LW},1} = \frac{M(h_0)}{\mu} \left(\gamma q^4 + \frac{d\phi}{dh}\,|_{h_0} q^2 \right), \tag{6.18}$$

while the Stokes-flow dispersion relation considering slip and disjoining pressure is

$$\Omega'_{\mathrm{Stokes},1} = \frac{\gamma q^2 + (d\phi/dh)|_{h_0}}{4\mu q} \frac{\sinh(2qh_0) - 2qh_0 + 4q\ell \sinh^2(qh_0)}{\cosh^2(qh_0) + q^2 h_0^2 + q\ell\,[2qh_0 + \sinh(2qh_0)]}. \tag{6.19}$$

The surface roughness W is thus determined by the spectrum with

$$W = \sqrt{\frac{1}{L^2} \int_0^L \int_0^L (\delta h)^2 \, dxdy} = \sqrt{\frac{1}{2\pi L^2} \int_{q_{\min}}^{q_{\max}} Sq \, dq}. \tag{6.20}$$

Here one has to think of the spectrum as radially symmetric in the wavenumber space for a two-dimensional surface.

We use the data of roughness from Experiment 1 (Exp. 1) presented in the figure 2 of [52]. To evaluate Eq. (6.20), the values of parameters (film thickness, surface tension, Hamaker constant, viscosity, q_{min}, q_{max} and initial condition $S(q,0)$) have to be known. Some of them (q_{min}, q_{max}, $S(q,0)$) are unavailable from [52]. For others, reference [52] provided referenced values but did not provide the fitting values of parameters used to align with experimental data. Therefore, we have to adjust some values of the parameters to have best match with the fitting curve in the figure 2 of [52] to infer what values may have been used by [52]. In summary, the values we use are $h_0 = 3.9$ nm, $\gamma = 0.045$ N/m, $\mu = 2 \times 10^4$ kg/(ms), $A = 2 \times 10^{-20}$ J, $S(q,0) = 0$, $q_{min} = 0.42$ nm^{-1} and $q_{max} = 0.1 q_d$, where q_d is the dominant wavenumber and $q_d = \sqrt{\frac{1}{\gamma} \frac{A}{2\pi h_0^4}}$.

The modified Langevin model compares well (see Fig. 6.9) with no-slip experiments of dewetting polymer films [52], where disjoining pressure plays a role. However, polymer films usually have a large slip (up to 1μm) [113, 114] on certain substrates. We thus suggest a experiment using the same polymer film mentioned above, but for a film with thickness $h_0 = 9$ nm and a large slip length $\ell = 450$ nm, to investigate the effects of slip on the dewetting of polymer films. We predict,

for future experiments, large slip would greatly accelerate the roughening and thus dewetting as shown in Fig. 6.9, and highlight the importance of using the Langevin model with Stokes-flow dispersion relation.

6.4 Summary

We have investigated the dynamic capillary waves of both planar and annular liquid films at the nanoscale. A Langevin model with a Stokes-flow dispersion relation is able to accurately predict the growth of capillary waves with slip effects, as validated by MD simulations. Our work provides grounds for carefully evaluating future experiments of thin films that currently rely on Capillary Wave Theory. The quantitative analysis of spontaneous roughening, which is connected to the theory of Universality Classes, allows better understanding of the instability of liquid-vapour or liquid-liquid interfaces [115]. The established relation between capillary spectra and slip also provides a method to measure large slip length such as water films on graphene where a shear-driven method shows considerable statistical errors [116].

Chapter 7

Anisotropic relaxation of capillary wave correlations

In this chapter, the relaxation dynamics of TCW correlations for nanoscale liquid films lying on anisotropic-slip substrates are studied using both MD simulations and the Langevin model developed in Chapter 3.

This chapter is organised as follows. In Sec. 7.1, we present the molecular dynamics setup adopted for simulating nanoscale liquid films on anisotropic-slip substrates. A description of how we obtain slip lengths from independent molecular dynamics is also provided. In Sec. 7.2, we extend the Langevin model introduced in Chapter 3 to consider anisotropic dynamics of TCWs and derive the dispersion relation for Stokes flow with anisotropic slip effects. Sec. 7.3 shows the comparison of MD simulations with theoretical models and discusses the effects of anisotropic-slip boundary conditions. We conclude our findings and outline future directions for this research in Sec. 7.4.

7.1 MD simulations

7.1.1 Setup for films on anisotropic-slip substrates

In this chapter, MD simulations are used to simulate TCWs of planar films on isotropic-slip and anisotropic-slip substrates. Unlike the simulations presented in earlier chapters, where the simulated films were quasi-2D with a very long length in the x-direction, the system here is fully 3D. Of course, this comes at considerable computational cost, and so the films considered here have a largest dimension that is smaller than those considered in Chapters 5 and 6. The domain contains three phases, with the liquid bounded by the vapor above and the solid below, as shown

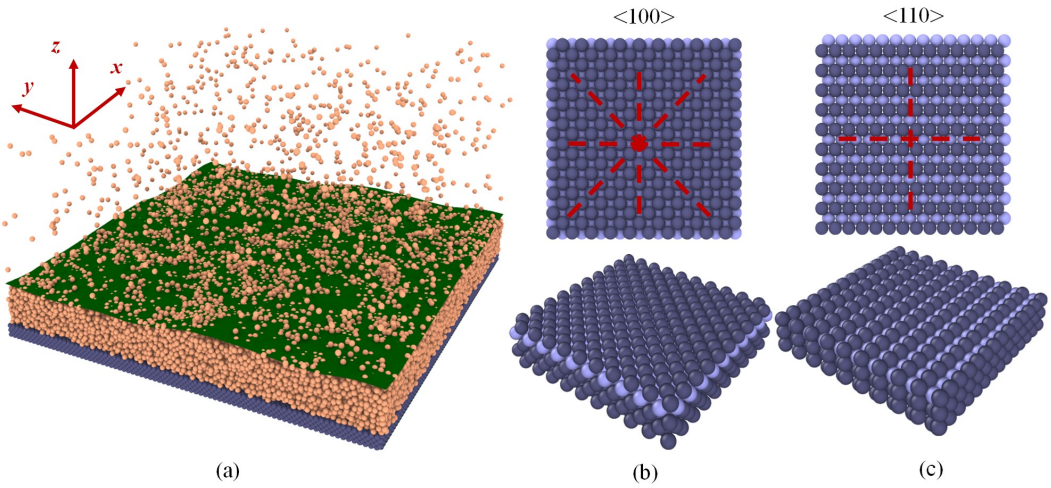

Figure 7.1: Snapshots of the set-up of a liquid film on a substrate in MD simulation. (a) A perspective view of the whole system. The fluid atoms are orange and the solid atoms are navy blue. The free surface generated by post-processing is coloured olive green. (b) Top view and perspective view of the isotropic $\langle 100 \rangle$ substrate surface. (c) Top and perspective view of the anisotropic $\langle 110 \rangle$ substrate surface. The red dash lines in (b) and (c) denotes the lines of symmetry and the light blue color indicates solid atoms in the second layer.

in Fig. 7.1(a). The liquid of the film is argon and the substrate is platinum with a face centred cubic (fcc) structure.

It has been noticed before that the different planes of the fcc lattice lead to varying slip properties due to the difference in interfacial atom structures [102], see Fig. 7.1(b) and (c). For example, the $\langle 100 \rangle$ surface has four lines of reflectional symmetry, and so is for practical purposes isotropic: a unidirectional flow in the x or y direction generates the same slip velocity at the hydrodynamic boundary, see Fig. 7.2(b). However, the $\langle 110 \rangle$ surface is evidently anisotropic with only two lines of symmetry (see Fig. 7.2(c)), since these unidirectional flows generate different slip velocities. Therefore, in this work, we use the $\langle 100 \rangle$ surface to represent a good approximation to an isotropic-slip substrate and the $\langle 110 \rangle$ surface to represent an anisotropic-slip substrate. We note that the slip anisotropy of the $\langle 110 \rangle$ surface was first discovered by Soong *et al.* [102]. However, their description of the resulting macroscopic slip boundary condition is incorrect, see the discussion in Sec. 7.2.

The liquid-solid interactions are modelled by the 12-6 LJ potential with $\varepsilon_{ls} = C\varepsilon_{ll}$ and $\sigma_{ls} = 0.8\sigma_{ll}$. We vary C to obtain different amounts of slip. For the $\langle 100 \rangle$ surface, we choose case 1: $C_{\langle 100 \rangle, 1} = 0.7$ and case 2: $C_{\langle 100 \rangle, 2} = 0.35$. For the $\langle 110 \rangle$ surface, we choose case $C_{\langle 110 \rangle} = 0.7$.

The initial dimensions of the liquid film (L_x, L_y, h) in Fig. 7.1(a) are chosen

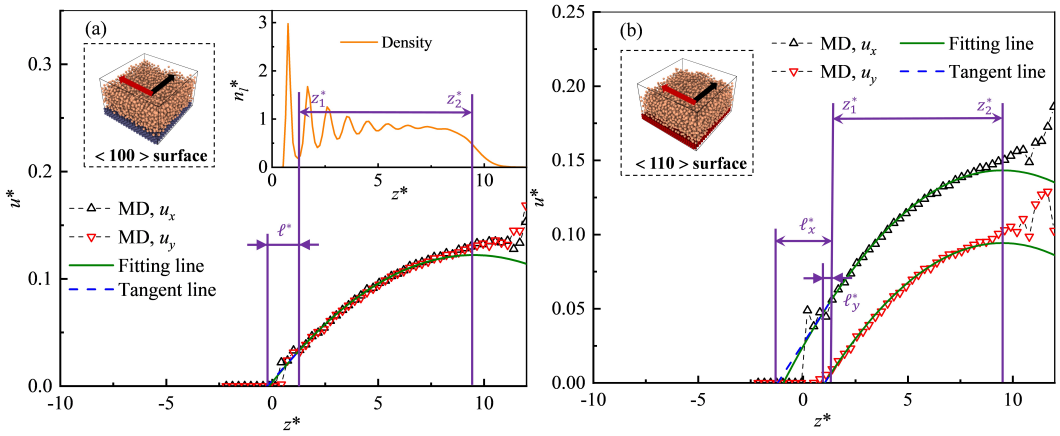

Figure 7.2: Slip length measured using a pressure-driven flow past a plate. MD velocity (triangles) are fitted with analytical solutions (olive solid lines) with the HB (z_1) at the first valley of MD density (orange solid line) and FS (z_2) at $0.5n_l^*$. The tangent line (blue dash lines) gives the slip length ℓ^*. (a) the measurement is done for the isotropic $\langle 100 \rangle$ surface; (b) the measurement is done for the anisotropic $\langle 110 \rangle$ surface.

as, $L_x = 31.4$ nm, $L_y = 31.4$ nm, and $h_0 = 3.14$ nm. The lateral size of the substrate is the same as that of the liquid film and it has a thickness $h_s = 0.78$ nm.

The initialization of MD simulations are the same with the one in Chapter 6. The initial position of the film surface is at $h_0 + d = 3.34$ nm.

The free surface position is defined as the usual equimolar surface. The way to extract the surface profile $h(x, y, t)$ from MD simulations is detailed in Chapter 3. Then two-dimensional Fourier transforms of the surface profile are performed to obtain the amplitude of interfacial Fourier modes.

7.1.2 Measurements of anisotropic slip length

Slip length is measured from independent configurations by simulating unidirectional (x or y direction) pressure-driven flow past a substrate surface as shown by the MD snapshots in the top-left corner of Figs. 7.2(a) and (b). The pressure gradient is created by applying a body force g (along x or y direction) to the fluid. The generated velocity distribution is parabolic: $u_{x,y}(z) = \frac{\rho g_{x,y}}{2\mu}(z - z_1)(2z_2 - z_1 - z) + u_s$. Here z_1 and z_2 are positions of the hydrodynamic boundary (HB) and free surface (FS), respectively, and u_s is the slip velocity at the HB.

As discussed earlier in Chapter 6, the HB is not at the solid surface. We choose the position of HB at the first valley of density distribution: $z_1^* = 1.2\sigma$ (see Fig. 7.2(a)). The position of the FS is determined in the standard way by the

location of equimolar surface where density is $0.5n_l^*$, with $z_2^* = 9.5\sigma$ (see Fig. 7.2(a)). After locating the boundary, the slip velocity is obtained by fitting velocity profiles of MD data (symbols) with analytical expressions of velocity (solid green lines) as shown in Fig. 7.2. The slip length ℓ is the distance between the HB and the position where the the linear extrapolation of the velocity profile vanishes, see the dashed blue lines (since the slip length is small for each case, the tangent line is close to the fitting line).

Figure 7.2(a) is for the measurement of slip length of case $C_{\langle 100\rangle,1}$. The individually applied body forces are $g_x^* = 0.01$ and $g_y^* = 0.01$. It can be seen that the velocity profiles u_x and u_y are nearly the same, indicating that the $\langle 100\rangle$ surface is isotropic in terms of slip. The slip length is thus characterised by a scalar value $\ell^* = 1.41\sigma$ (0.48 nm). In the same way, the slip length $\ell = 3.34$ nm for case $C_{\langle 100\rangle,2}$ is obtained. We note that applying larger body forces may lead to a shear-dependent slip length [90], but here we have ensured that we remain in the regime where the measured slip length is constant independent of driving force magnitude.

For the $\langle 110\rangle$ surface, the individually applied body forces are also $g_x^* = 0.01$ and $g_y^* = 0.01$. There is a clear difference between u_x and u_y (see Fig. 7.2(b)), indicating that the $\langle 110\rangle$ surface exhibits significant anisotropy. The slip length in the x and y direction is measured to be $\ell_x = 0.80$ nm and $\ell_y = 0.05$ nm respectively, for the case $C_{\langle 110\rangle}$.

We note that as the HB does not align with the edge of the solid, the effective thickness of the fluid domain simulated for capillary waves is different from its initial thickness. As the position of the initial free-surface is at 3.34 nm and the HB is at $z_{\mathrm{HB}} = 0.41$ nm, the effective thickness of a planar film is 2.93 nm.

7.2 Theoretical approach

7.2.1 Langevin model for TCW correlations

As shown in Chapter 3, the dynamics of capillary waves can be described by a Langevin equation:

$$\frac{\gamma q^2}{\Omega(q_x, q_y)} \frac{\partial}{\partial t} \widehat{\delta h} = -\gamma q^2 \widehat{\delta h} + \zeta \widehat{N}. \tag{7.1}$$

Here the Langevin model is extended to consider waves that are vectors instead of scalars, as presented before, and where q is the magnitude of a wave vector $\boldsymbol{q} = (q_x, q_y)$ with $q = \sqrt{q_x^2 + q_y^2}$. The $\Omega(q_x, q_y)$ is the wave-direction dependent dispersion relation, $\widehat{N}(\boldsymbol{q}, t)$ is a complex Gaussian random variable with zero mean and covariance $\langle |\widehat{N}\widehat{N'}| \rangle = \delta(\boldsymbol{q} - \boldsymbol{q'})\delta(t - t')$, and ζ is the noise amplitude.

Using the equipartition theorem, the static spectra of a 2D surface are

$$S_{\mathrm{s,2D}} = \sqrt{\langle |\widehat{\delta h}|^2 \rangle_s} = \sqrt{\frac{L^2 k_B T}{\gamma q^2}}. \tag{7.2}$$

As discussed in Chapter 3, the noise amplitude ζ can be found from the static spectrum

$$\zeta = \sqrt{\frac{2}{\Omega}} \gamma q^2 \, S_{\mathrm{s,2D}} \, . \tag{7.3}$$

To obtain the temporal correlations of interfacial Fourier modes from the Langevin equation, we use the Itô integral [48, 51]. Substituting Eq. (7.3) into Eq. (7.1) leads to

$$\frac{\partial}{\partial t} \widehat{\delta h} = -\Omega \widehat{\delta h} + \sqrt{2\Omega} S_{\mathrm{s,2D}} \widehat{N}. \tag{7.4}$$

The solution to Eq (7.4) is

$$\widehat{\delta h}\,(q_x, q_y, t) = \widehat{\delta h}\,(q_x, q_y, 0)\, e^{-\Omega t} + \sqrt{2\Omega} S_{\mathrm{s,2D}} \int_0^t e^{-\Omega(t-s)} d\widehat{W}\,(q_x, q_y, s)\,, \tag{7.5}$$

where $\widehat{W} = \int \widehat{N}\, dt$ is the Wiener process with covariance

$$\left\langle \widehat{W}\,(\boldsymbol{q}, t)\, \widehat{W}^*\,(\boldsymbol{q}, t') \right\rangle = \min(t, t'). \tag{7.6}$$

Here the asterisk denotes a conjugate value.

The temporal correlations of surface modes are thus obtained from Eq. (7.5) as

$$\left\langle \widehat{\delta h}(q_x, q_y, t) \widehat{\delta h}^*(q_x, q_y, t') \right\rangle = B_1 + B_2, \tag{7.7}$$

where B_1 is given by

$$\begin{aligned} B_1 &= \left\langle \widehat{\delta h}\,(q_x, q_y, 0)\, \widehat{\delta h}^*\,(q_x, q_y, 0) \right\rangle e^{-\Omega(q_x, q_y)t} e^{-\Omega(q_x, q_y)t'} \\ &= \left\langle \left| \widehat{\delta h}\,(q_x, q_y, 0) \right|^2 \right\rangle e^{-\Omega(q_x, q_y)(t+t')}, \end{aligned} \tag{7.8}$$

and B_2 is given by

$$\begin{aligned} B_2 &= 2\Omega S_{s,2D}^2 \left\langle \int_0^t e^{-\Omega(t-s)} d\widehat{W}\left(q_x, q_y, s\right) \int_0^{t'} e^{-\Omega(t'-s')} d\widehat{W}^*\left(q_x, q_y, s'\right) \right\rangle \\ &= 2\Omega S_{s,2D}^2 \int_0^t e^{-\Omega(t-s)} \int_0^{t'} e^{-\Omega(t'-s')} \left\langle d\widehat{W}\left(q_x, q_y, s\right) d\widehat{W}^*\left(q_x, q_y, s'\right) \right\rangle \\ &= 2\Omega S_{s,2D}^2 \int_0^{\min(t,t')} e^{-\Omega(t+t'-2s)} ds \\ &= -S_{s,2D}^2 \left[e^{-\Omega(t+t')} - e^{-\Omega|t-t'|} \right]. \end{aligned} \tag{7.9}$$

By putting B_1 and B_2 together we obtain the final expression for temporal correlations of TCWs

$$\begin{aligned} \left\langle \widehat{\delta h}(q_x, q_y, t) \widehat{\delta h}^*(q_x, q_y, t') \right\rangle = &\left\langle \left| \widehat{\delta h}(q_x, q_y, 0) \right|^2 \right\rangle e^{-\Omega(q_x,q_y)(t+t')} \\ &- L^2 \frac{k_B T}{\gamma q^2} \left[e^{-\Omega(q_x,q_y)(t+t')} - e^{-\Omega(q_x,q_y)|t-t'|} \right], \end{aligned} \tag{7.10}$$

A similar expression is presented in [48, 51], but, is limited to the application in thin liquid films without slip.

Equation (7.10) can describe two important aspects of capillary wave dynamics. The first aspect is the growth of capillary wave spectra to the static spectra (using $t = t'$ to obtain the equal-time correlations), namely, the process of surface roughening, which is studied in Chapter 6. For our case, one can assume that the free surface is smooth, $\langle |\widehat{\delta h}(q_x, q_y, 0)|^2 \rangle = 0$, so that Eq. (7.10) is simplified to

$$\left\langle \left| \widehat{\delta h}(q_x, q_y, t) \right|^2 \right\rangle = L^2 \frac{k_B T}{\gamma q^2} \left[1 - e^{-2\Omega(q_x,q_y)t} \right]. \tag{7.11}$$

Thus, the time scale for a smooth surface to reach the static spectra, i.e. thermal equilibrium, is $t_s = \max\left[1/\Omega(q_x, q_y)\right]$. In the following, we use $S\left(q_x, q_y, t\right) = \sqrt{\langle |\widehat{\delta h}(q_x, q_y, t)|^2 \rangle}$ for notational simplicity.

The second aspect is the relaxation of capillary wave correlations after a free surface reaches the static spectra. In this case, the initial condition $\langle |\widehat{\delta h}(q_x, q_y, 0)|^2 \rangle = L^2 k_B T / \left(\gamma q^2\right)$ so that Eq. (7.10) is reduced to

$$\left\langle \widehat{\delta h}(q_x, q_y, t) \widehat{\delta h}^*(q_x, q_y, t') \right\rangle = L^2 \frac{k_B T}{\gamma q^2} e^{-\Omega(q_x,q_y)|t-t'|}. \tag{7.12}$$

Thus, the Langevin equation bridges the gap between the growth of capillary wave spectrum and the relaxation of capillary wave correlations, allowing them to be

described in a single framework. We note that Eq. (7.12) can be derived alternatively using fluctuation-dissipation theorem shown by Henle *et al.* [58], which, however, is unable to predict the growth of capillary waves at the same time. Also, the work in [58] only considers isotropic-slip effects so that the dispersion relation in Eq. (7.12) is $\Omega(q)$ instead of $\Omega(q_x, q_y)$. In the following, we define a dimensionless variable

$$\begin{aligned} R_{h_q h_q^*}\left(q_x, q_y, \left|t-t'\right|\right) &= \left\langle \widehat{\delta h}(q_x, q_y, t)\widehat{\delta h}^*(q_x, q_y, t')\right\rangle / \left(L^2 \frac{k_B T}{\gamma q^2}\right) \\ &= e^{-\Omega(q_x, q_y)|t-t'|}, \end{aligned} \tag{7.13}$$

to normalise Eq. (7.12) with the static spectrum.

7.2.2 Anisotropic boundary condition and dispersion relation

To derive the required dispersion relation, we perform a linear stability analysis of three-dimensional Stokes flow. We outline the governing equations for this problem and keep the details of the derivations in Appendix C. The liquid is assumed to be incompressible and the vapour is dynamically passive. Incompressibility requires that

$$\nabla \cdot \mathbf{u} = 0, \tag{7.14}$$

where $\mathbf{u} = (u_x, u_y, u_z)$, and u_x, u_y, u_z are the velocities in x, y, z directions, respectively. The momentum equation with the assumption of Stokes flow is:

$$\mu \nabla^2 \mathbf{u} = \nabla p, \tag{7.15}$$

where μ is the liquid viscosity and p is the liquid's pressure with respect to that of the vapour. For the boundary conditions, at the position of free surface $z = h(x, y, t)$, we have the dynamic condition:

$$\boldsymbol{\vartheta} \cdot \mathbf{n} = -\left(\gamma \nabla \cdot \mathbf{n}\right)\mathbf{n}, \tag{7.16}$$

where $\boldsymbol{\vartheta}$ is the hydrodynamic stress tensor, $\vartheta_{ij} = -p\delta_{ij} + \mu\left(\partial u_i/\partial x_j + \partial u_j/\partial x_i\right)$; γ is the surface tension; and $\mathbf{n}$ is the outward normal to the free surface:

$$\mathbf{n} = \frac{(-\partial h/\partial x, -\partial h/\partial y, 1)}{\sqrt{1 + (\partial h/\partial x)^2 + (\partial h/\partial y)^2}}. \tag{7.17}$$

Under the assumption of small perturbations ($\frac{\partial h}{\partial x}, \frac{\partial h}{\partial y} \ll 1$), the dynamic boundary condition is reduced to (in the normal direction):

$$-p + \mu \frac{\partial u_z}{\partial z} = \gamma \left(\frac{\partial^2 h}{\partial x^2} + \frac{\partial^2 h}{\partial y^2} \right), \tag{7.18}$$

and in the tangential directions to the surface

$$\frac{\partial u_x}{\partial z} + \frac{\partial u_z}{\partial x} = 0\,, \tag{7.19}$$

$$\frac{\partial u_y}{\partial z} + \frac{\partial u_z}{\partial y} = 0\,. \tag{7.20}$$

The kinematic condition at the free surface is given by

$$u_z = \frac{\partial h}{\partial t} + u_x \frac{\partial h}{\partial x} + u_y \frac{\partial h}{\partial y}. \tag{7.21}$$

At the substrate surface, the no penetration condition is,

$$u_z = 0, \tag{7.22}$$

and the anisotropic-slip boundary condition is,

$$u_x = \ell_x \frac{\partial u_x}{\partial z}\,, \tag{7.23}$$

$$u_y = \ell_y \frac{\partial u_y}{\partial z}\,, \tag{7.24}$$

as we will explain now.

The Navier-slip boundary condition describes the proportionality of wall shear stress (τ) to velocity slip (u) so that for a two-dimensional flow (and one-dimensional boundary) in the x-direction we have:

$$u_x = \beta \tau_x\,, \tag{7.25}$$

where $\beta = \ell/\mu$. Extending Eq. (7.25) to two-dimensional surfaces is straightforward when the surface is isotropic (i.e. when β is scalar):

$$\mathbf{u}_{||} = \beta \boldsymbol{\tau}_{||}\,. \tag{7.26}$$

Here the subscript $||$ after a vector denotes its parallel components to the solid surface. At first thoughts, one could consider incorporating anisotropy into the Navier-slip condition by maintaining the form of Eq. (7.26), but making the slip

length dependent on direction (e.g. $\beta(\theta)$)[102]. However, this is incorrect, since it assumes that velocity slip is always in the direction of the wall shear stress. Consider, for example, the case $\beta_y = 0$ (i.e. no-slip in this direction) and $\beta_x > 0$: the y-component of slip (u_y) is zero irrespective of the direction of the wall shear stress, and therefore slip velocity and shear stress can easily be misaligned (apart from when $\boldsymbol{\tau}_{||}$ is in the x direction).

In other words, surface anisotropy breaks the simple scalar proportionality described by Eq. (7.26). To generalise the boundary condition requires the introduction of a slip-coefficient (second-order) tensor:

$$\mathbf{u}_{||} = \boldsymbol{\beta} \cdot \boldsymbol{\tau}_{||} \,. \tag{7.27}$$

For isotropic surfaces $\boldsymbol{\beta} = \beta \boldsymbol{I}$, where $\boldsymbol{I}$ is the identity tensor. In this article we consider slip on *orthotropic* surfaces; surfaces that have two axes of symmetry (see Fig. 7.1), which are orthogonal (unlike isotropic surfaces, which have an infinite number). In the case of orthotropic surfaces:

$$\boldsymbol{\beta} = \begin{pmatrix} \beta_1 & 0 \\ 0 & \beta_2 \end{pmatrix} , \tag{7.28}$$

where β_1 and β_2 are slip related parameters along the two lines of symmetry (e.g. with the grain and against the grain). Thus, the slip boundary for the $\langle 110 \rangle$ is obtained as Eq. (7.23) and Eq. (7.24).

Notably the slip boundary condition obtained by combining Eq. (7.27) and Eq. (7.28) assumes that the coordinate system is aligned to the axes of symmetry of the orthotropic surface. More generally, if this is not the case, we would have:

$$\boldsymbol{\beta} = \begin{pmatrix} \beta_x & \beta_{xy} \\ \beta_{yx} & \beta_y \end{pmatrix} = \begin{pmatrix} \beta_1 \cos\alpha & \beta_2 \sin\alpha \\ -\beta_1 \sin\alpha & \beta_2 \cos\alpha \end{pmatrix} , \tag{7.29}$$

where α is the angle between the cartesian coordinate system and the orthotropic axes, but henceforth we do not consider this possibility as for our case we know $\alpha = 0$.

With above Eqs. (7.14-7.24), the linear stability analysis gives the dispersion

relation (see Appendix C):

$$\Omega\left(q_x, q_y\right) = \frac{\gamma q}{4\mu} \frac{\sinh\left(2qh_0\right) - 2qh_0 + 4J\sinh^2\left(qh_0\right)}{q^2h_0^2 + \cosh^2\left(qh_0\right) + J\left[2qh_0 + \sinh\left(2qh_0\right)\right]},$$
$$J = q\ell_x - q\frac{\ell_x - \ell_y}{1 + \frac{q_x^2[q\ell_y \sinh(qh_0)+\cosh(qh_0)]}{q_y^2[q\ell_x \sinh(qh_0)+\cosh(qh_0)]}}. \tag{7.30}$$

If $\ell_x = \ell_y$, Eq. (7.30) is reduced to the existing dispersion relation for films on isotropic substrates[58, 117, 118].

Notably, one may solve the fluctuating hydrodynamics equations to predict capillary wave dynamics [52, 53, 64, 90, 119] instead of the Langevin model presented here. However, to do so analytically, previous works [52, 53, 64, 90, 119] have had to exploit the long-wave approximation, which limits their application to thin liquid films and slender jets. In particular, they are not suitable for the work considered here where the film length (compared to the film thickness) is not large. Direct solution to fluctuating hydrodynamics without the long-wave approximation is needed to apply to more general cases such as the problem considered here.

7.3 Results and Discussions

In this section, we present and discuss our MD simulation results and their comparison to analytical solutions. Firstly, we show the transient growth of capillary wave spectra to the static spectrum. Secondly, using the isotropic-slip $\langle 100 \rangle$ substrate, we explore the effects of different slip length on the relaxation of capillary wave correlations. Thirdly, the effects of anisotropic slip on the relaxation of capillary wave correlations are demonstrated using the $\langle 110 \rangle$ substrate.

7.3.1 Transient growth of capillary wave spectra

The growth of capillary waves to the static spectrum, from an initially smooth interface, is shown in Fig. 7.3 for case $C_{\langle 100 \rangle, 2}$ where slip length $\ell_x = \ell_y = 3.34$ nm. As the simulation starts, the free surface becomes rough, and the Fourier transform of the free surface shape is performed at various intervals to obtain the evolving spectra. As shown by the inset of the Fig. 7.3, the spectra of surface waves from MD simulations is radially symmetric, which is expected from Eq. (7.11) and Eq. (7.30) due to the isotropic slip length. Thus, the spectra can be averaged over the azimuthal direction and represented in terms of $q = \sqrt{q_x^2 + q_y^2}$, with the results shown by triangles in Fig. 7.3. The spectra are also ensemble averaged over

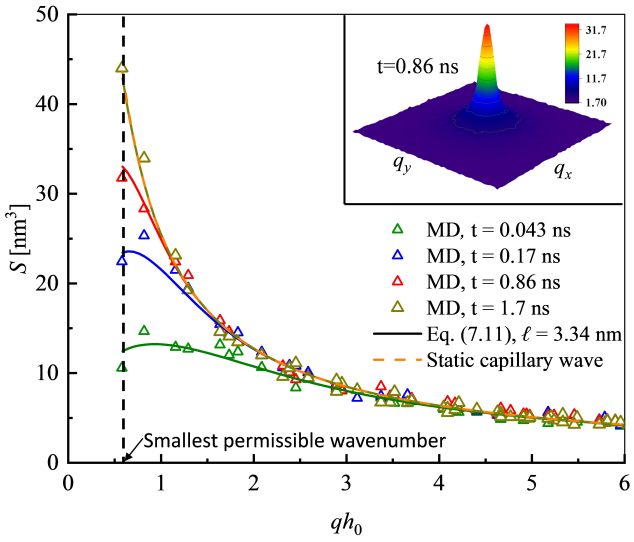

Figure 7.3: Capillary wave growth for case $C_{\langle 100\rangle,2}$. MD spectra after averaging over azimuthal directions are shown by triangles, with different color represents varying time. The analytical solutions are given by solid lines. The inset shows the 2D spectra from the 2D Fourier transform of the free surface at $t = 0.86$ ns.

40 independent realizations. It can be seen that the spectra evolve with time but the static spectrum given by the capillary wave theory forms an upper limit. The transition time for the smooth surface to reach the static spectrum is $1/\Omega(q = q_{min})$, where $q_{min} = 2\pi/L$ is based on the longest wavelength on the periodic surface, and it is evaluated to be about $t_s = 1$ ns. This is confirmed by the positions of the dark yellow symbols in Fig. 7.3, at time $t = 1.7$ ns, which show the surface has safely reached the static spectrum.

To measure the correlation of capillary waves presented in the next subsections, it is important to make sure the surface has the state of thermal equilibrium characterised by the static spectrum. As shown, the transition time found from our knowledge of the growth of capillary waves provides a useful guideline. In the long-wave approximation, $2\pi h_0/L \ll 1$, one can find the transition time scales with L^4 from the Stokes dispersion relation [90], which means that care should be taken when interpreting results for larger film lengths where reaching thermal equilibrium (the static spectrum) for the surface is often computationally intractable. This problem seems to appear in previous MD simulations of thermal capillary waves using very long films but has not been pointed out and explained [111]. It may also not be negligible in experimental studies of thermal capillary waves using high-viscosity polymers, where the film length is at the microscale or macroscale [90].

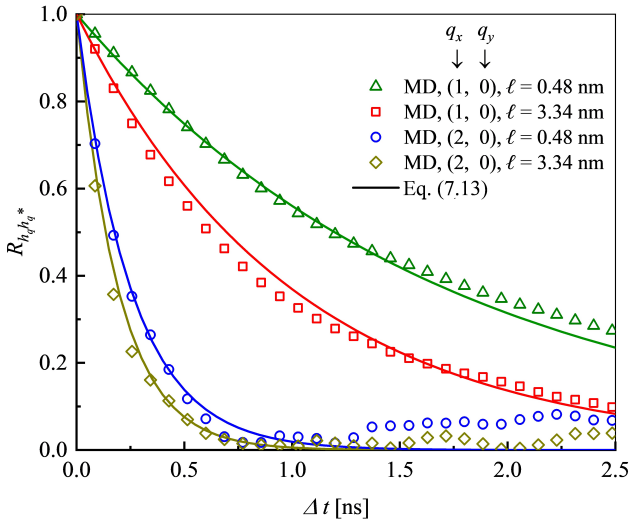

Figure 7.4: Effects of varying slip length on temporal correlations of thermal capillary waves. MD results (different symbols) are compared with the analytical solutions Eq. (7.13) (solid lines). Wave vectors are represented by $\boldsymbol{q} = (q_x, q_y) = \frac{2\pi}{L}(n_x, n_y)$, where (n_x, n_y) are pairwise integers, and without loss of generality, we consider waves in the x-direction due to the isotropy.

7.3.2 Relaxation of capillary wave correlations with varying slip

In this subsection, we explore the effect of different slip length on the relaxation of capillary wave correlations using the isotropic $\langle 100 \rangle$ surface. As shown earlier in Sec. 7.2, increased slip length is achieved by decreasing the liquid-solid interactions; case $C_{\langle 100 \rangle, 2}$ has slip length $\ell = 3.34$ nm, while case $C_{\langle 100 \rangle, 1}$ has slip length $\ell = 0.48$ nm. After the transition time of each case ($t_s = 1.7$ ns for case $C_{\langle 100 \rangle, 1}$ and $t_s = 1.0$ ns for case $C_{\langle 100 \rangle, 2}$), the 2D Fourier transform of the surface position at different times is performed and the temporal correlations calculated (averaged over 10000 times). Wave vectors are represented by $\boldsymbol{q} = (q_x, q_y) = \frac{2\pi}{L}(n_x, n_y)$ where (n_x, n_y) are pairwise integers, characterising the wave numbers. As the relaxation of capillary wave correlations on the $\langle 100 \rangle$ surface is expected to be radially symmetric (see further discussions in Sec. 7.3.3), only correlations in the x-direction ($q_y = 0$) are presented in Fig. 7.4, without loss of generality. In Fig. 7.4, for the same wave vector, it can be seen that larger slip length leads to faster decay of $R_{h_q h_q^*}$, from the MD results (olive triangles and red squares, for instance). On the other hand, given the same slip length, wave vectors with larger wavenumbers (the norm of a vector) decay faster (see olive triangles and blue circles, for instance). Both of these features, and the actual values, are well predicted by the Langevin equation results from Eq. (7.13) and Eq. (7.30), using the independently measured slip length.

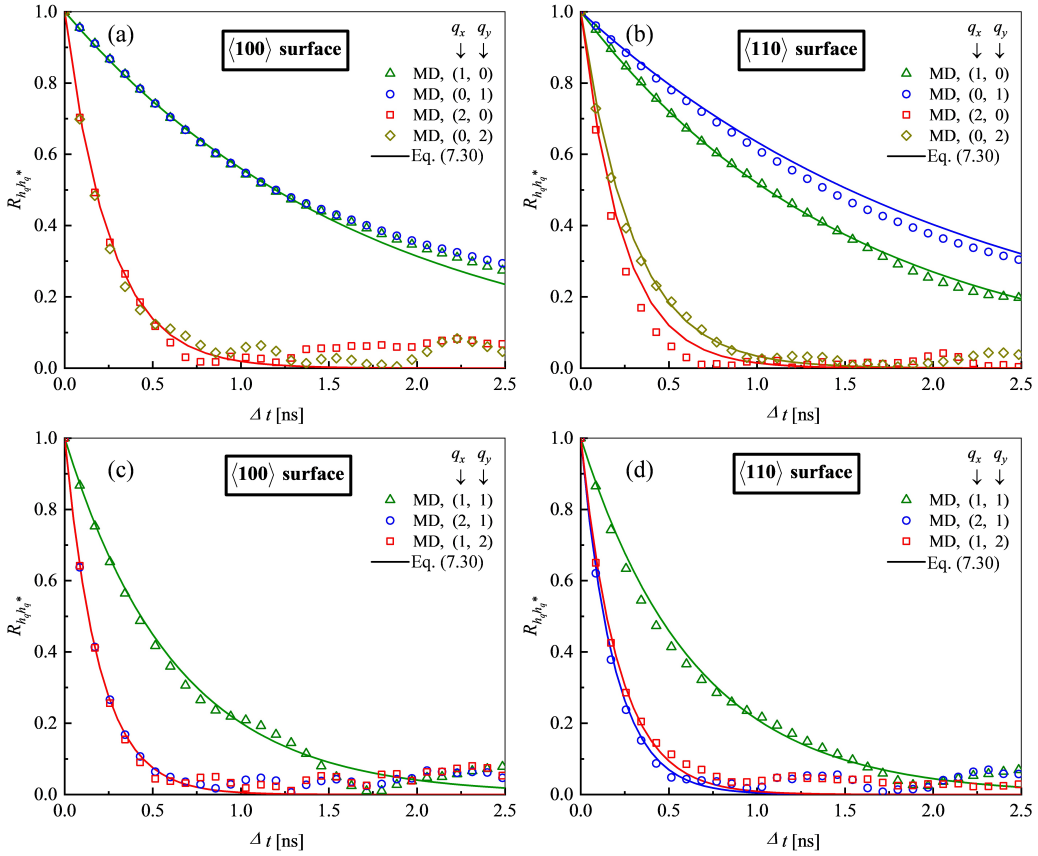

Figure 7.5: Effects of anisotropic slip on temporal correlations of thermal capillary waves. MD results (symbols) are compared with analytical solutions (solid lines). Figure (a) and (c) are for the ⟨100⟩ surface, and figure (b) and (d) are for the ⟨110⟩ surface. Wave vectors are represented by $(q_x, q_y) = \frac{2\pi}{L}(n_x, n_y)$ where (n_x, n_y) are pairwise integers.

7.3.3 Relaxation of capillary wave correlations with anisotropic slip

Consider now the effects of anisotropic slip on the relaxation of capillary wave correlations. Fig. 7.5 shows the comparison of wave correlations with different orientations for the case $C_{\langle 100\rangle,1}$ and case $C_{\langle 110\rangle}$. For the isotropic ⟨100⟩ surface, the relaxation of correlations of wave vectors at different directions for a given wavenumber are the same as shown in Figs. 7.5(a) and (c). For example, the relaxation of the correlation of a wave vector at the direction (1, 0) is the same as that of a wave vector at (0, 1), and the relaxation of the correlation of a wave vector at (1, 2) is the same as that of a wave vector at (2, 1). However, for the anisotropic ⟨110⟩ surface, as shown in Figs. 7.5 (b) and (d), the relaxation of correlations of waves for a given wavenumber varies with directions. For example, the correlation of the $(1, 0)$ wave

vector relaxes faster than that of the wave vector $(0, 1)$. The wave vector $(2, 1)$ also decays faster than the wave vector $(1, 2)$ in terms of correlations. Clearly, the anisotropic relaxation of capillary wave correlations is due to the anisotropic slip boundary conditions. A wave vector closer to the x-direction having a faster decay than a wave vector (with the same wavenumber) closer to the y-direction; this is also due to the larger slip length in the x-direction similar to the case in Sec. 7.3.1. However, the difference becomes smaller when the wavenumber is increased. This means that to infer the anisotropy of a substrate from measuring the correlations of capillary waves, it is better to measure the correlations of waves with smaller wavenumbers. Using the measured slip length at Sec. 7.2, and the derived new dispersion relation, the relaxation of capillary waves for $\langle 110 \rangle$ surface can be predicted well by Eq. (7.13) and Eq. (7.30) (see solid lines).

Now we consider the relaxation time t_R, which is equal to $1/\Omega$. We focus on the relaxation time of wave vectors along the x or y direction as the relaxation of those waves only depends on the slip length in that direction. Figure 7.6 shows the values of relaxation time obtained from MD simulations agree well with the analytical solutions. A simple asymptotic analysis of the dispersion shows that there are two scaling relations between the dispersion relation and non-dimensional wavenumber qh_0.

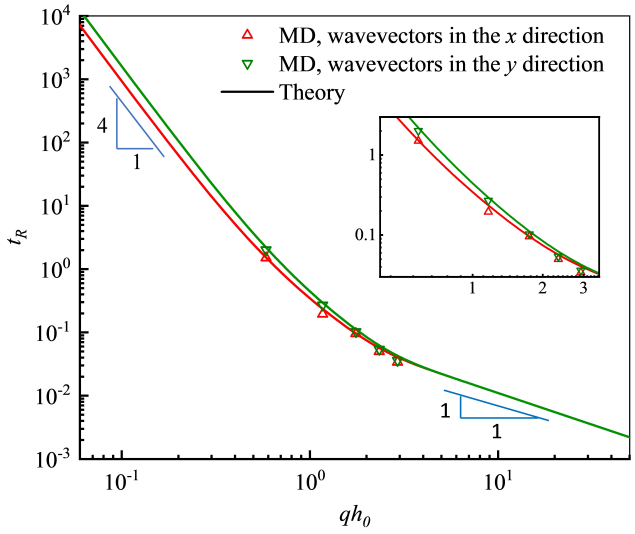

Figure 7.6: Relaxation time as a function of wavenumbers. MD results (symbols) are compared with analytical solutions (solid lines).

Firstly, for a very long film (or thin film) $qh_0 \ll 1$ with small slip $\ell_x \leq h_0$

and $\ell_y \leq h_0$, the dispersion relation Eq. (7.30) can be significantly simplified to

$$\Omega(q_x, q_y) \approx \frac{\gamma}{3\mu} q^4 h_0^2 \left[h_0 + 3\frac{\left(q_x^2 \ell_x + q_y^2 \ell_y\right)}{q^2} \right]. \tag{7.31}$$

Thus, the relaxation time t_R scales with q^{-4} for a wave vector along the x or y direction, which is supported by Fig. 7.6 when qh_0 goes to zero. This also means that the relaxation time for $q = 2\pi/L$ scales with L^4 so that it becomes experimentally measurable for long films (the relaxation time for a short film is a few nanoseconds in our MD simulations).

Secondly, in the opposite limit, if $qh_0 \gg 1$, the dispersion relation is simplified to

$$\Omega(q_x, q_y) \approx \frac{\gamma}{2\mu} q, \tag{7.32}$$

so that the relaxation time scales with q^{-1}, which is shown by Fig. 7.6 when qh_0 goes to infinity. Equation (7.32) also means that dispersion relation is independent of slip length and becomes isotropic so that we cannot use thermal capillary waves of thick films ($qh_0 \gg 1$) to measure slip length.

We note that if the slip length is very large $\ell \gg h_0$, there may be other scaling relations, as shown in [58] though the analysis there is for isotropic slip. The effects of disjoining pressure or gravity can be easily incorporated into Eq. (7.2) and Eq. (7.30) to extend the applicability of the theory.

7.4 Summary

In this work, the effects of anisotropic slip on the relaxation of correlations of thermal capillary waves are investigated both numerically and analytically. We perform molecular dynamics simulations of liquid films bounded by isotropic-slip substrates and anisotropic-slip substrates. The correlations of Fourier modes obtained from simulations compare well with a Langevin equation, where a new dispersion relation considering the anisotropic-slip boundary condition is derived. Our results show that the larger slip length leads to faster decay of the correlations, and the anisotropic-slip leads to anisotropic relaxations of capillary wave correlations.

Though the anisotropic surface used in our MD simulations is ideal, it may provide inspiration for making engineered surfaces that are anisotropic in slip, which may be useful in micro- or nano-fluidics to obtain a directional control on liquid transport. We also believe this work strengthens the applicability of using thermal capillary waves as a non-invasive method to infer slip length in future experiments

using existing isotropic or anisotropic-slip substrates. The temporal correlations can be directly obtained in experiments using x-ray techniques[55, 60] and they can be fitted with analytical solutions developed here to obtain slip lengths, which is the usual way to infer properties of interest using surface waves. Notably, this chapter provides guidance on the experimental setup, in particular showing that temporal correlations of capillary waves of thick films ($qh_0 \gg 1$) cannot be used to measure slip.

Chapter 8

Conclusion and future work

Due to the rapid progress in microfluidics and nanofluidics, there is a growing number of studies investigating the effects of thermal fluctuations on nanoscale flows. In this thesis, we focus on how thermal fluctuations and slip affect interfacial flows at the nanoscale.

In bulk flows, Fluctuating Hydrodynamics (FH) equations model thermal fluctuations by introducing an additional stochastic stress (white noise) into the conservation equations. However, FH equations cannot predict how or whether Navier's slip condition, at the liquid-solid interface, is modified by thermal fluctuations. Navier's slip condition phenomenologically describes the mechanical equilibrium between the shear stress at the boundary and the friction force from the wall. Thus, it is natural to extend the stochastic stress in the bulk to the boundary. In Chapter 3, it is found that the covariance of the stochastic stress at the boundary should be related to slip length, which is consistent with the Green-Kubo expression for the friction factor [69].

Direct solutions to FH either numerically or analytically in application to interfacial flows are very complicated. Instead, using a long-wave approximation to FH allows us to derive stochastic lubrication equations (SLE) for planar films and annular films, and perform analysis (see Chapter 3). This approach needs to carefully scale each component of the noise tensor and they are usually scaled as the same as the corresponding component of the hydrodynamic tensor.

We apply the SLE for planar films to study the dewetting of nanofilms in Chapter 5, where, conventionally, the dewetting is due to disjoining pressure. But we reveal that thermal fluctuations can overwhelm disjoining pressure and become the dominant cause of the dewetting of films of a few nanometres thickness. Importantly, we show that thermal fluctuations are critical to the nature of the instability

of nanoscale thin-film flows: they significantly intensify the amplitude of undulations, render the dominant wavenumber time-dependent, and decrease the critical wavelength.

Central to the derivation of the SLEs is the long-wave assumption, which means they cannot accurately predict dynamics of interfacial waves with wavelengths comparable to that of the film height. To derive the SLEs, we also assumed that the slip length is of the order of the film thickness, which limits their application to relatively small-slip systems. A Langevin model, beyond the current lubrication framework, is thus proposed (Chapter 3), to predict the dynamics of capillary waves (at the linear stage) in these more general cases. In the Langevin model, a Stokes-flow dispersion relation is adopted, and since it is derived for interfacial modes with any wavelength and any slip length, the Langevin model resolves the inherent problems of those SLEs in the prediction of capillary wave dynamics.

We apply the Langevin model to study the growth of thermal capillary waves (TCWs) in Chapter 6. We make interesting observations of surface roughening of planar films due to TCWs. It is found that the roughness can be described by a type of Universality Class, where the roughness grows as a power of time $W \sim t^{1/8}$ before saturation. A knowledge of the transient growth of TCWs allows us to predict the time for a flat surface to reach its thermal equilibrium (saturated roughness), which provides guidelines for the widely studied relaxation dynamics of TCW correlations, where thermal equilibrium has to be assumed.

At thermal equilibrium, the correlations of TCWs show a simple exponential decay and the decay rate is the dispersion relation, in which the liquid-solid slip can be included. Thus, measuring the correlations of TCWs seems to be a good method to infer slip, having the advantage of being non-invasive. With this motivation, we investigate the effects of slip on correlations of TCWs in Chapter 7. Unlike the usual consideration of isotropic-slip substrates, we consider slip to be anisotropic and it is found that anisotropic slip leads to the anisotropic relaxation of TCW correlations. These interesting relaxation dynamics of TCW correlations can also be predicted by our Langevin model, with a newly derived dispersion relation taking into account the anisotropic slip boundary.

Following on from the success of our current models, there are several extensions or improvements that could be made in future work.

Nonlinear dynamics of SLEs

The applications of the derived SLEs are linear, with a focus on the instability and growth of surface waves at early stages in their development. In the future, it will

be interesting, using the developed SLEs, to investigate how thermal fluctuations and slip influence the dynamics during the non-linear stages of film growth, such as rupture, the formation of droplets, and their coarsening process.

Solving the deterministic Planar-film LE has shown that the rupture due to disjoining pressure has similarity solutions and the film thickness decreases like $(t_r - t)^{1/5}$, where $t_r - t$ is the time remaining before rupture [120]. As for the solution to Jet SLE, where thermal fluctuations are shown to speed up the rupture of a slender thread and lead to a new similarity solution [45], thermal fluctuations may result in new similarity solutions of thin-film rupture described by the Planar-film SLE.

The influence of thermal fluctuations on droplet formation after film rupture was investigated by Nesic *et al.* [46] using numerical solutions to the Planar-film SLE without slip, and they show thermal fluctuations reduce the number of droplets but increase the variability in size and space distribution of droplets when compared to the deterministic counterparts. Our newly derived SLE with slip modelled allows the investigation of the combined effects of thermal fluctuations and slip on the droplet formation and coarsening. Though slip is expected to accelerate the rupture of a film, it is uncertain how slip influences the number of droplets and their distribution.

Inertial effects in nanoscale interfacial flows

Inertial effects are not considered in current SLEs or the Langevin model. In the literature, for free liquid films or bounded films with very large slip, plug flow is assumed and often inertial effects are accounted for in the derivation of LEs for both cases [66, 91]. Interestingly, the LE for a bounded film with infinite slip is the same as the LE for a free liquid film.

To develop new theories to consider inertial effects in stochastic modelling of interfacial flows, one may also use a long-wave approximation to FH equations to derive a new SLE to include inertial terms, but the process of the asymptotic expansion of FH may be different from what has been done in this thesis. In fact, to derive the deterministic LE for a free liquid film, one has to keep the second-order terms after the asymptotic expansion of the NS equations [91]. Therefore, it is expected that new scaling of the noise tensor in FH equations should be adopted in contrast to the one in this thesis, and a Free-film SLE may be derived.

To investigate whether inertial effects can be observed in MD simulations, a free liquid film or a bounded film with infinite slip can be simulated. Then the capillary spectra can be obtained from MD simulations and compared to current models assuming Stokes flows, to see whether inertial effects need to be considered.

Linear stability analysis of FH equations

The Langevin model for nanoscale interfacial flows in this thesis is a phenomenological model. Alternatively, one may perform linear stability analyses of the Stokes version of FH equations directly and get the evolving equation of film height.

In fact, this idea is not new at all. The Langevin equation describing the Brownian motion of a macroscopic particle in a fluctuating fluid is also quite phenomenological. Interestingly, research has shown that this Langevin equation for Brownian motion can be derived independently from FH equations, but only under certain conditions [121].

There are several works that have already investigated the possibility of obtaining the governing equation of the interfacial height of an infinite-depth film from FH equations in Fourier space [122, 123]. In order to accomplish this task, Green's-function identity was used to solve linearised FH equations with boundary conditions at the free surface in these works. The static spectrum can be recovered from the derived equation of motion for the free surface. However, the growth of capillary wave spectra or the relaxation of capillary wave correlations studied in this thesis are not obtained in these works [122, 123]. It is thus interesting to see whether the interfacial equation in these works [122, 123] agrees with the phenomenological model in this thesis in more detail.

On the other hand, it is much more difficult to obtain such interfacial equations for a finite-depth film from FH equations where the liquid-solid boundary condition is involved. This remains a great challenge to be investigated in the future.

Appendix A

Simplification of the stochastic integral

Here the method to simplify the stochastic integral in Eq. (3.29) for the planar film and in Eq. (3.56) for the annular film, is presented. The main result used, that we will derive in this appendix, is:

$$\int_{w_1}^{w_2} f(z)\mathcal{N}(z)dz = \left[\int_{w_1}^{w_2} f(z)^2 dz\right]^{1/2} N. \tag{A.1}$$

Here $\mathcal{N}$ is Gaussian white noise, with covariance $\langle \mathcal{N}(z)\mathcal{N}(z')\rangle = B\delta(z-z')$ (the $\delta(x-x')$ and $\delta(t-t')$ are transposed out the integral since the integral is performed only in z direction), and $f(z)$ is some function of z. The w_1 and w_2 are non-Gaussian random variables that are uncorrelated with $\mathcal{N}$ (but potentially correlated with each other). The N is a single Gaussian random number with the same variance as $\mathcal{N}$ (i.e. $\mathrm{var}(N) = B$). To verify Eq. (A.1) holds, we start by defining a simple transformation:

$$\alpha = \frac{z - w_1}{w_2 - w_1}, \tag{A.2}$$

such that

$$\int_{w1}^{w2} f(z)dz = (w_2 - w_1)\int_0^1 f(\alpha)d\alpha, \tag{A.3}$$

$$\int_{w1}^{w2} f(z)^2 dz = (w_2 - w_1)\int_0^1 f(\alpha)^2 d\alpha. \tag{A.4}$$

In discretised forms,

$$\int_{w1}^{w2} f(z)\mathcal{N}(z)dz = \sqrt{\frac{w_2 - w_1}{M}} \sum_{i=1}^{M} f(z_i)\mathcal{N}_i, \tag{A.5}$$

$$\int_{0}^{1} f(\alpha)\mathcal{N}(\alpha)d\alpha = \sqrt{\frac{1}{M}} \sum_{i=1}^{M} f(\alpha_i)\mathcal{N}_i. \tag{A.6}$$

where M is the number of grid points ($M \to \infty$) and $\langle \mathcal{N}_i \mathcal{N}_j \rangle = A\delta_{ij}$. Since $\sum_{i=1}^{M} f(z_i)\mathcal{N}_i$ and $\sum_{i=1}^{M} f(\alpha_i)\mathcal{N}_i$ are Gaussian, and from Eq. (A.4), one can show

$$\sum_{i=1}^{M} f(z_i)^2 = \sum_{i=1}^{M} f(\alpha_i)^2, \tag{A.7}$$

which means $\sum_{i=1}^{M} f(z_i)\mathcal{N}_i$ and $\sum_{i=1}^{M} f(\alpha_i)\mathcal{N}_i$ have the same variance and are thus equal. Therefore, it is found

$$\int_{w1}^{w2} f(z)\mathcal{N}(z)dz = \sqrt{w_2 - w_1} \int_{0}^{1} f(\alpha)\mathcal{N}(\alpha)d\alpha. \tag{A.8}$$

Due to the Gaussian property of $\sum_{i=1}^{M} f(z_i)\mathcal{N}_i$, it can also be shown that

$$\int_{0}^{1} f(\alpha)\mathcal{N}(\alpha)d\alpha = \left(\int_{0}^{1} f(\alpha)^2 d\alpha \right)^{1/2} N. \tag{A.9}$$

Essentially, Eq. (A.9) is a continuous form of Bienayme's formula. Finally, one can get

$$\begin{aligned} &\int_{w1}^{w2} f(z)\mathcal{N}(z)dz \\ &= \sqrt{w_2 - w_1} \int_{0}^{1} f(\alpha)\mathcal{N}(\alpha)d\alpha \\ &= \left[(w_2 - w_1) \int_{0}^{1} f(\alpha)^2 d\alpha \right]^{1/2} N \\ &= \left[\int_{w_1}^{w_2} f(z)^2 dz \right]^{1/2} N. \end{aligned} \tag{A.10}$$

Appendix B

Stokes dispersion relation for annular films with slip

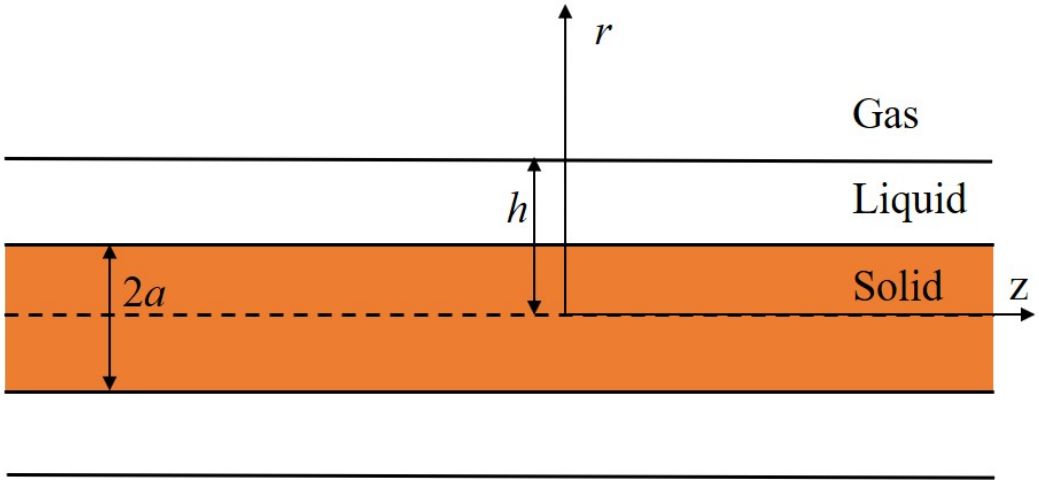

Figure B.1: Sketch of a liquid film on a fibre

For a liquid film flowing on a fibre, axisymmetric Stokes flow is assumed in the annular film. We use the method in [21] to calculate the dispersion relation analytically, but now assuming we have slip at the liquid-solid interface. The momentum equations are

$$\frac{\partial p}{\partial r} = \mu \left[\frac{\partial}{\partial r} \left(\frac{1}{r} \frac{\partial (ru)}{\partial r} \right) + \frac{\partial^2 u}{\partial x^2} \right], \tag{B.1}$$

$$\frac{\partial p}{\partial z} = \mu \left[\frac{1}{r} \frac{\partial}{\partial r} \left(r \frac{\partial w}{\partial r} \right) + \frac{\partial^2 w}{\partial z^2} \right]. \tag{B.2}$$

Here u, w and p are the radial velocity, axial velocity and pressure, respectively.

The mass conservation with incompressible assumption is

$$\frac{1}{r}\frac{\partial(ru)}{\partial r}+\frac{\partial w}{\partial z}=0. \tag{B.3}$$

In terms of the boundary conditions, we have the slip boundary condition and no-penetration condition at the fibre surface $r=a$ such that

$$w=\ell\frac{\partial w}{\partial r}, \tag{B.4}$$

$$u=0. \tag{B.5}$$

At the free surface $r=h$, the no-shear boundary condition, for small surface perturbations, is

$$\frac{\partial w}{\partial r}+\frac{\partial u}{\partial z}=0, \tag{B.6}$$

and the normal force balance requires (for small surface perturbations)

$$-p+2\mu\frac{\partial u}{\partial r}=\gamma\left\{\frac{\partial^2 h/\partial z^2}{\left[(\partial h/\partial z)^2+1\right]^{3/2}}-\frac{1}{h\left[(\partial h/\partial z)^2+1\right]^{1/2}}\right\}. \tag{B.7}$$

Meanwhile, the kinematic condition is

$$\frac{\partial h}{\partial t}+w\frac{\partial h}{\partial z}=u. \tag{B.8}$$

The linear stability analysis of the above equations (B.1-B.8) is performed using $u=\tilde{u}e^{\Omega t+iqz}$, $w=\tilde{w}e^{\Omega t+iqz}$, $p=p_0+\tilde{p}e^{\Omega t+iqx}$, and $h=h_0+\tilde{h}e^{\Omega t+iqz}$. The linearisation of the momentum equations leads to

$$\mu\left[\frac{d}{dr}\left(\frac{1}{r}\frac{d(r\tilde{u})}{dr}\right)-q^2\tilde{u}\right]=\frac{d\tilde{p}}{dr}, \tag{B.9}$$

$$\mu\left[\frac{1}{r}\frac{d}{dr}\left(r\frac{d\tilde{w}}{dr}\right)-q^2\tilde{w}\right]=iq\tilde{p}. \tag{B.10}$$

For the equation of mass conservation, we have

$$\frac{1}{r}\frac{d(r\tilde{u})}{dr}+iq\tilde{w}=0. \tag{B.11}$$

Using (B.9-B.11), the elimination of $\tilde{w}$ and $\tilde{p}$ leads to a fourth-order ordinary

partial differential equation for $\tilde{u}$

$$\frac{d}{dr}\frac{1}{r}\frac{d}{dr}\left\{r\frac{d}{dr}\left[\frac{1}{r}\frac{d(r\tilde{u})}{dr}\right]\right\} - 2q^2\frac{d}{dr}\left[\frac{1}{r}\frac{d(r\tilde{u})}{dr}\right] + q^4\tilde{u} = 0. \tag{B.12}$$

The general solution of this equation is [21]

$$\tilde{u} = C_1 r K_0[qr] + C_2 K_1[qr] + C_3 r I_0[qr] + C_4 I_1[qr], \tag{B.13}$$

where $K_0(K_1)$ and $I_0(I_1)$ are zeroth (first) order modified Bessel function of second and first kind. We can also get the expressions for $\tilde{w}$ and $\tilde{p}$ which are

$$\begin{aligned}\tilde{w} = &-\frac{1}{iq}\left\{C_1\left[2K_0(qr) - qrK_1(qr)\right] - C_2 qK_0(qr)\right. \\ &\left. + C_3\left[2I_0(qr) + qrI_1(qr)\right] + C_4 qI_0(qr)\right\}, \end{aligned}\tag{B.14}$$

$$\tilde{p} = 2\mu\left[C_1 K_0(qr) + C_3 I_0(qr)\right]. \tag{B.15}$$

The four coefficients (C_1-C_4) are determined by the boundary conditions (B.4-B.8). For boundary conditions (B.4) and (B.5) at $r = a$, their linearised form are

$$\tilde{w} = \ell\frac{d\tilde{w}}{dr}, \tag{B.16}$$

$$\tilde{u} = 0. \tag{B.17}$$

And for boundary conditions (B.6-B.8) at $r = h_0$, their linearisation gives

$$\frac{d\tilde{w}}{dr} + iq\tilde{u} = 0, \tag{B.18}$$

$$-\tilde{p} + 2\mu\frac{d\tilde{u}}{dr} = (-\gamma q^2 + \gamma\frac{1}{h_0^2})\tilde{h}, \tag{B.19}$$

$$\Omega = \frac{\tilde{u}}{\tilde{h}}. \tag{B.20}$$

A substitution of (B.13-B.15) into linearised boundary conditions (B.16-B.20) leads to a set of four homogeneous equations, which is

$$\begin{pmatrix} m_{11} & m_{12} & m_{13} & m_{14} \\ aK_0(qa) & K_1(qa) & aI_0(qa) & I_1(qa) \\ -K_1(qh_0) + qh_0K_0(qh_0) & qK_1(qh_0) & qh_0I_0(qh_0) + I_1(qh_0) & qI_1(qh_0) \\ m_{41} & m_{42} & m_{43} & m_{44} \end{pmatrix}\begin{pmatrix} C_1 \\ C_2 \\ C_3 \\ C_4 \end{pmatrix} = 0, \tag{B.21}$$

where the elements of first row are given by

$$
\begin{aligned}
m_{11} &= q(2\ell - a)K_1(qa) - (\ell a q^2 - 2)K_0(qa), \\
m_{12} &= -qK_0(qa) - \ell q^2 K_1(qa), \\
m_{13} &= -(\ell a q^2 - 2)I_0(qa) - q(2\ell - a)I_1(qa), \\
m_{14} &= qI_0(qa) - \ell q^2 I_1(qa).
\end{aligned} \tag{B.22}
$$

The elements of fourth row are given by

$$
\begin{aligned}
m_{41} &= 2\mu q h_0 K_1(qh_0) - Dh_0 K_0(qh_0)/\Omega, \\
m_{42} &= 2\mu \left[qK_0(qh_0) + K_1(qh_0)/h_0\right] - DK_1(qh_0)/\Omega, \\
m_{43} &= -2\mu q h_0 I_1(qh_0) - Dh_0 I_0(qh_0)/\Omega, \\
m_{44} &= -2\mu \left[qI_0(qh_0) - I_1(qh_0)/h_0\right] - DI_1(qh_0)/\Omega.
\end{aligned} \tag{B.23}
$$

Here D is the driving force $D = \gamma(q^2 - 1/h^2)$. The vanishing of the determinant of 4×4 matrix gives the dispersion relation $\Omega = \Omega(q)$. Numerically, we use Matlab to solve the determinant of the matrix.

Appendix C

Anisotropic dispersion relation for planar films

In this appendix, we show the details of derivation of the dispersion relation Eq. (7.30) using the anisotropic-slip boundary conditions. Equations (7.14-7.24) are linearised using normal modes

$$\begin{aligned} u_x &= \tilde{u}_x e^{\Omega t + iq_x x + iq_y y}, \\ u_y &= \tilde{u}_y e^{\Omega t + iq_x x + iq_y y}, \\ u_z &= \tilde{u}_z e^{\Omega t + iq_x x + iq_y y}, \\ p &= p_0 + \tilde{p} e^{\Omega t + iq_x x + iq_y y}, \\ h &= h_0 + \tilde{h} e^{\Omega t + iq_x x + iq_y y}. \end{aligned} \tag{C.1}$$

With those, the linearised forms of Eqs. (7.14-7.15) are

$$iq_x \tilde{u}_x + iq_y \tilde{u}_y + \frac{d\tilde{w}_z}{dz} = 0, \tag{C.2}$$

$$\mu \left(-q_x^2 \tilde{u}_x - q_y^2 \tilde{u}_x + \frac{d^2 \tilde{u}_x}{dz^2} \right) = iq_x \tilde{p}, \tag{C.3}$$

$$\mu \left(-q_x^2 \tilde{u}_y - q_y^2 \tilde{u}_y + \frac{d^2 \tilde{u}_y}{dz^2} \right) = iq_y \tilde{p}. \tag{C.4}$$

The expression for the single variable $\tilde{u}_z$ can be obtained from Eqs. (C.2-C.4) as:

$$\frac{d^4 \tilde{u}_z}{dz^4} - 2q^2 \frac{d^2 \tilde{u}_z}{dz^2} + q^4 \tilde{u}_z = 0. \tag{C.5}$$

The general solution for $\tilde{u}_z$ is thus [58, 117]

$$\tilde{u}_z = C_1 \cosh(qz) + C_2 \sinh(qz) + C_3 qz \cosh(qz) + C_4 qz \sinh(qz), \tag{C.6}$$

and one can also obtain the solution for $\tilde{u}_x$, $\tilde{u}_y$, and $\tilde{p}$:

$$\tilde{u}_x = \frac{1}{q^2}\left\{ iq_x \frac{d\tilde{w}}{dz} + iq_y \left[D_1 \cosh(qz) + D_2 \sinh(qz) \right] \right\}, \tag{C.7}$$

$$\tilde{u}_y = \frac{1}{q^2}\left\{ iq_y \frac{d\tilde{w}}{dz} - iq_x \left[D_1 \cosh(qz) + D_2 \sinh(qz) \right] \right\}, \tag{C.8}$$

$$\tilde{p} = 2\mu q \left[C_3 \cosh(qz) + C_4 \sinh(qz) \right]. \tag{C.9}$$

Here, $C_1 - C_4$, D_1 and D_2 are six coefficients to be determined by the boundary conditions Eq. (7.18-7.24), whose linearised forms are

$$\tilde{u}_z = 0, \tag{C.10}$$

$$\tilde{u}_x = \ell_x \frac{d\tilde{u}_x}{dz}, \tag{C.11}$$

$$\tilde{u}_y = \ell_y \frac{d\tilde{u}_y}{dz}, \tag{C.12}$$

for those at the free surface $z = 0$ respectively, and

$$-\tilde{p} + 2\frac{d\tilde{w}}{dz} = -\gamma \left(q_x^2 + q_y^2 \right) \tilde{h}, \tag{C.13}$$

$$\frac{d\tilde{u}_x}{dz} + iq_x \tilde{u}_z = 0, \tag{C.14}$$

$$\frac{d\tilde{u}_y}{dz} + iq_y \tilde{u}_z = 0, \tag{C.15}$$

$$\Omega = \frac{\tilde{u}_z}{\tilde{h}}. \tag{C.16}$$

for those at the solid surface $z = h_0$ respectively.

Substituting Eqs. (C.6-C.9) into Eqs. (C.10-C.12) leads to

$$C_1 = 0, \tag{C.17}$$

$$q_y D_1 + q_x q \left(C_2 + C_3 \right) - \ell_x \left[q_x q^2 (C_1 + 2C_4) + D_2 q q_y \right] = 0, \tag{C.18}$$

$$-q_x D_1 + q_y q (C_2 + C_3) - \ell_y \left[q_y q^2 (C_1 + 2C_4) - D_2 q q_x \right] = 0, \tag{C.19}$$

and substituting Eqs. (C.6-C.9) into Eqs. (C.13-C.15) leads to

$$2\mu q[\sinh(qh_0)C_1+\cosh(qh_0)C_2+qh\sin(qh_0)C_3+qh\cosh(qh_0)C_4]=-\gamma q^2\tilde{h}, \tag{C.20}$$

$$\begin{aligned}&2q^2\{\cosh(qh_0)C_1+\sinh(qh_0)C_2+[\sinh(qh_0)+qh\cosh(qh_0)]C_3\\&+[\cosh(qh_0)+qh\sinh(qh_0)]C_4\}+\frac{q_y}{q_x}q\sinh(qh_0)D_1+\frac{q_y}{q_x}q\cosh(qh_0)D_2=0,\end{aligned} \tag{C.21}$$

$$\begin{aligned}&2q^2\{\cosh(qh_0)C_1+\sinh(qh_0)C_2+[\sinh(qh_0)+qh\cosh(qh_0)]C_3\\&+[\cosh(qh_0)+qh\sinh(qh_0)]C_4\}-\frac{q_x}{q_y}q\sinh(qh_0)D_1-\frac{q_x}{q_y}q\cosh(qh_0)D_2=0.\end{aligned} \tag{C.22}$$

Using Eqs. (C.6-C.9), Eq. (C.16) and Eq. (C.17), the dispersion relation is given by:

$$\Omega=\frac{-\gamma q^2\tilde{w}}{-\tilde{p}+2\mu\frac{d\tilde{w}}{dz}}=\frac{-\gamma q^2}{2\mu q}\frac{\sinh(qh)C_2+qh\cosh(qh)C_3+qh\sin(qh)C_4}{\cosh(qh)C_2+qh\sinh(qh)C_3+qh\cos(qh)C_4}. \tag{C.23}$$

The remaining task is writing C_2 and C_3 as a function of C_4. Using Eqs. (C.17-C.22), we can obtain:

$$\begin{aligned}&D_1=MD_2, M=-\frac{\cosh(qh_0)}{\sinh(qh_0)},\\&D_2=\frac{2(\ell_x-\ell_y)q^2q_xq_y}{q_y^2(M-\ell_xq)+q_x^2(M-\ell_yq)}C_4,\\&C_2=-C_3+JC_4, J=2\ell_xq-\frac{2(\ell_x-\ell_y)qq_y^2(M-\ell_xq)}{q_y^2(M-\ell_xq)+q_x^2(M-\ell_yq)},\\&C_3=-\frac{\sinh(qh_0)J+\cosh(qh_0)+qh\sinh(qh_0)}{qh\cosh(qh_0)}C_4.\end{aligned} \tag{C.24}$$

Substituting Eq. (C.24) into Eq. (C.23) and eliminating C_4 lead to the anisotropic dispersion relation

$$\begin{aligned}&\Omega(q_x,q_y)=\frac{\gamma q}{4\mu}\frac{\sinh(2qh_0)-2qh_0+4J\sinh^2(qh_0)}{q^2h_0^2+\cosh^2(qh_0)+J[2qh_0+\sinh(2qh_0)]},\\&J=q\ell_x-q\frac{\ell_x-\ell_y}{1+\frac{q_x^2[q\ell_y\sinh(qh_0)+\cosh(qh_0)]}{q_y^2[q\ell_x\sinh(qh_0)+\cosh(qh_0)]}}.\end{aligned} \tag{C.25}$$

Bibliography

[1] JC Fernández-Toledano, TD Blake, and J De Coninck. Contact-line fluctuations and dynamic wetting. *J. Colloid Interface Sci.*, 540:322–329, 2019.

[2] Dirk GAL Aarts, Matthias Schmidt, and Henk NW Lekkerkerker. Direct visual observation of thermal capillary waves. *Science*, 304(5672):847–850, 2004.

[3] Michael Moseler and Uzi Landman. Formation, stability, and breakup of nanojets. *Science*, 289(5482):1165–1169, 2000.

[4] Jürgen Becker, Günther Grün, Ralf Seemann, Hubert Mantz, Karin Jacobs, Klaus R Mecke, and Ralf Blossey. Complex dewetting scenarios captured by thin-film models. *Nat. Mater.*, 2(1):59, 2003.

[5] Günther Grün, Klaus Mecke, and Markus Rauscher. Thin-film flow influenced by thermal noise. *J. Stat. Phys.*, 122(6):1261–1291, 2006.

[6] Amrit Kalra, Shekhar Garde, and Gerhard Hummer. Osmotic water transport through carbon nanotube membranes. *Proc. Natl. Acad. Sci. U. S. A.*, 100(18):10175–10180, 2003.

[7] Shuo Guo, Min Gao, Xiaomin Xiong, Yong Jian Wang, Xiaoping Wang, Ping Sheng, and Penger Tong. Direct measurement of friction of a fluctuating contact line. *Phys. Rev. Lett.*, 111(2):026101, 2013.

[8] ER Smith, EA Müller, RV Craster, and OK Matar. A langevin model for fluctuating contact angle behaviour parametrised using molecular dynamics. *Soft Matter*, 12(48):9604–9615, 2016.

[9] LD Landau and EM Lifshitz. *Course of Theoretical Physics. vol. 6: Fluid mechanics*. London, 1959.

[10] M Malek Mansour, Alejandro L Garcia, George C Lie, and Enrico Clementi. Fluctuating hydrodynamics in a dilute gas. *Phys. Rev. Lett.*, 58(9):874, 1987.

[11] Florencio Balboa, John B Bell, Rafael Delgado-Buscalioni, Aleksandar Donev, Thomas G Fai, Boyce E Griffith, and Charles S Peskin. Staggered schemes for fluctuating hydrodynamics. *Multiscale Model. Simul.*, 10(4):1369–1408, 2012.

[12] Kerstin Falk, Felix Sedlmeier, Laurent Joly, Roland R Netz, and Lydéric Bocquet. Molecular origin of fast water transport in carbon nanotube membranes: superlubricity versus curvature dependent friction. *Nano Lett.*, 10(10):4067–4073, 2010.

[13] Matthew K Borg, Duncan A Lockerby, Konstantinos Ritos, and Jason M Reese. Multiscale simulation of water flow through laboratory-scale nanotube membranes. *J. Membr. Sci.*, 567:115–126, 2018.

[14] Rasel Das, Md Eaqub Ali, Sharifah Bee Abd Hamid, Seeram Ramakrishna, and Zaira Zaman Chowdhury. Carbon nanotube membranes for water purification: a bright future in water desalination. *Desalination*, 336:97–109, 2014.

[15] Detlef Lohse, Xuehua Zhang, et al. Surface nanobubbles and nanodroplets. *Rev. Mod. Phys.*, 87(3):981, 2015.

[16] M Serdar Onses, Erick Sutanto, Placid M Ferreira, Andrew G Alleyne, and John A Rogers. Mechanisms, capabilities, and applications of high-resolution electrohydrodynamic jet printing. *Small*, 11(34):4237–4266, 2015.

[17] Alexander Oron, Stephen H Davis, and S George Bankoff. Long-scale evolution of thin liquid films. *Rev. Mod. Phys.*, 69(3):931, 1997.

[18] Jens Eggers and Todd F Dupont. Drop formation in a one-dimensional approximation of the navier–stokes equation. *J. Fluid Mech.*, 262:205–221, 1994.

[19] Malcolm B Williams and Stephen H Davis. Nonlinear theory of film rupture. *J. Colloid Interf. Sci.*, 90(1):220–228, 1982.

[20] IL Kliakhandler, Stephen H Davis, and SG Bankoff. Viscous beads on vertical fibre. *J. Fluid Mech.*, 429:381–390, 2001.

[21] RV Craster and OK Matar. On viscous beads flowing down a vertical fibre. *J. Fluid Mech.*, 553:85–105, 2006.

[22] V Anoop Kishore and Dipankar Bandyopadhyay. Electric field induced patterning of thin coatings on fiber surfaces. *J. Phys. Chem. C*, 116(10):6215–6221, 2012.

[23] Alejandro G Gonzalez, Javier A Diez, Roberto Gratton, Diego M Campana, and Fernando A Saita. Instability of a viscous liquid coating a cylindrical fibre. *J. Fluid Mech.*, 651:117–143, 2010.

[24] Zijing Ding, Jinlong Xie, Teck Neng Wong, and Rong Liu. Dynamics of liquid films on vertical fibres in a radial electric field. *J. Fluid Mech.*, 752:66–89, 2014.

[25] Demetrios T Papageorgiou. Film flows in the presence of electric fields. *Annu. Rev. Fluid Mech.*, 51:155–187, 2019.

[26] Alexander Oron. Three-dimensional nonlinear dynamics of thin liquid films. *Phys. Rev. Lett.*, 85(10):2108, 2000.

[27] Zijing Ding and Teck Neng Wong. Three-dimensional dynamics of thin liquid films on vertical cylinders with marangoni effect. *Phys. Fluids*, 29(1):011701, 2017.

[28] Oleg E Shklyaev and Eliot Fried. Stability of an evaporating thin liquid film. *J. Fluid Mech.*, 584:157–183, 2007.

[29] Lingzhi Cai, Joel Marthelot, and P-T Brun. An unbounded approach to microfluidics using the rayleigh–plateau instability of viscous threads directly drawn in a bath. *Proc. Natl. Acad. Sci. U. S. A.*, 116(46):22966–22971, 2019.

[30] Alain De Ryck and David Quéré. Gravity and inertia effects in plate coating. *J. Colloid Interf. Sci.*, 203(2):278–285, 1998.

[31] David Quéré. Fluid coating on a fiber. *Annu. Rev. Fluid Mech.*, 31(1):347–384, 1999.

[32] Myung S Jhon, David M Phillips, Stephen J Vinay, and Christopher T Messer. The dynamic behavior of thin-film lubricants. *IEEE T Magn.*, 35(5):2334–2337, 1999.

[33] Francesco Naso, Francesco Babudri, Donato Colangiuli, Gianluca M Farinola, Fabio Quaranta, Roberto Rella, Raffaele Tafuro, and Ludovico Valli. Thin film construction and characterization and gas-sensing performances of a tailored phenylene- thienylene copolymer. *J. Am. Chem. Soc.*, 125(30):9055–9061, 2003.

[34] Jian Yu Huang, Yu-Chieh Lo, Jun Jie Niu, Akihiro Kushima, Xiaofeng Qian, Li Zhong, Scott X Mao, and Ju Li. Nanowire liquid pumps. *Nat. Nanotechnol.*, 8(4):277, 2013.

[35] R Xie, Alamgir Karim, Jack F Douglas, Charles C Han, and Robert A Weiss. Spinodal dewetting of thin polymer films. *Phys. Rev. Lett.*, 81(6):1251, 1998.

[36] Uwe Thiele, Michael Mertig, and Wolfgang Pompe. Dewetting of an evaporating thin liquid film: Heterogeneous nucleation and surface instability. *Phys. Rev. Lett.*, 80(13):2869, 1998.

[37] Rajesh Khanna and Ashutosh Sharma. Pattern formation in spontaneous dewetting of thin apolar films. *J. Colloid Interf. Sci.*, 195(1):42–50, 1997.

[38] Ashutosh Sharma and Rajesh Khanna. Pattern formation in unstable thin liquid films. *Phys. Rev. Lett.*, 81(16):3463, 1998.

[39] Matthias Lessel, Joshua D McGraw, Oliver Bäumchen, and Karin Jacobs. Nucleated dewetting in supported ultra-thin liquid films with hydrodynamic slip. *Soft Matter*, 13(27):4756–4760, 2017.

[40] Alejandro G Gonzalez, Javier A Diez, Yueying Wu, Jason D Fowlkes, Philip D Rack, and Lou Kondic. Instability of liquid cu films on a sio2 substrate. *Langmuir*, 29(30):9378–9387, 2013.

[41] Rabibrata Mukherjee and Ashutosh Sharma. Instability, self-organization and pattern formation in thin soft films. *Soft Matter*, 11(45):8717–8740, 2015.

[42] Trung Dac Nguyen, Miguel Fuentes-Cabrera, Jason D Fowlkes, and Philip D Rack. Coexistence of spinodal instability and thermal nucleation in thin-film rupture: Insights from molecular levels. *Phys. Rev. E*, 89(3):032403, 2014.

[43] Ralf Seemann, Stephan Herminghaus, and Karin Jacobs. Dewetting patterns and molecular forces: A reconciliation. *Phys. Rev. Let.*, 86(24):5534, 2001.

[44] Karin Jacobs, Ralf Seemann, and Stephan Herminghaus. Stability and dewetting of thin liquid films. In *Polymer thin films*, pages 243–265. World Scientific, 2008.

[45] Jens Eggers. Dynamics of liquid nanojets. *Phys. Rev. Lett.*, 89(8):084502, 2002.

[46] S Nesic, R Cuerno, E Moro, and L Kondic. Fully nonlinear dynamics of stochastic thin-film dewetting. *Phys. Rev. E*, 92(6):061002, 2015.

[47] Benny Davidovitch, Esteban Moro, and Howard A Stone. Spreading of viscous fluid drops on a solid substrate assisted by thermal fluctuations. *Phys. Rev. Lett.*, 95(24):244505, 2005.

[48] Javier A Diez, Alejandro G Gonzalez, and Roberto Fernández. Metallic-thin-film instability with spatially correlated thermal noise. *Phys. Rev. E*, 93(1):013120, 2016.

[49] Miguel A Durán-Olivencia, Rishabh S Gvalani, Serafim Kalliadasis, and Grigorios A Pavliotis. Instability, rupture and fluctuations in thin liquid films: Theory and computations. *J. Stat. Phys.*, 174(3):579–604, 2019.

[50] Maulik S Shah, Volkert van Steijn, Chris R Kleijn, and Michiel T Kreutzer. Thermal fluctuations in capillary thinning of thin liquid films. *J. Fluid Mech.*, 876:1090–1107, 2019.

[51] Klaus Mecke and Markus Rauscher. On thermal fluctuations in thin film flow. *J. Stat. Phys.*, 17(45):S3515, 2005.

[52] Renate Fetzer, M Rauscher, R Seemann, Karin Jacobs, and Klaus Mecke. Thermal noise influences fluid flow in thin films during spinodal dewetting. *Phys. Rev. Lett.*, 99(11):114503, 2007.

[53] Chengxi Zhao, James E Sprittles, and Duncan A Lockerby. Revisiting the rayleigh–plateau instability for the nanoscale. *J. Fluid Mechan.*, 861, 2019.

[54] Bruno Bresson, Coralie Brun, Xavier Buet, Yong Chen, Matteo Ciccotti, Jérôme Gâteau, Greg Jasion, Marco N Petrovich, Francesco Poletti, David J Richardson, et al. Anisotropic superattenuation of capillary waves on driven glass interfaces. *Phys. Rev. Lett.*, 119(23):235501, 2017.

[55] Hyunjung Kim, A Rühm, L. B Lurio, J. K Basu, J Lal, D Lumma, S. G. J Mochrie, and S. K Sinha. Surface dynamics of polymer films. *Phys. Rev. Lett.*, 90(6):068302, 2003.

[56] Luis G MacDowell, Jorge Benet, and Nebil A Katcho. Capillary fluctuations and film-height-dependent surface tension of an adsorbed liquid film. *Phys. Rev. Lett.*, 111(4):047802, 2013.

[57] R Evans. The role of capillary wave fluctuations in determining the liquid-vapour interface: Analysis of the van der waals model. *Mol. Phys.*, 42(5):1169–1196, 1981.

[58] Mark L Henle and Alex J Levine. Capillary wave dynamics on supported viscoelastic films: single and double layers. *Phys. Rev. E*, 75(2):021604, 2007.

[59] Zhang Jiang, Hyunjung Kim, X Jiao, HLYJ Lee, Y-J Lee, Y Byun, S Song, D Eom, C Li, MH Rafailovich, et al. Evidence for viscoelastic effects in surface capillary waves of molten polymer films. *Phys. Rev. Lett.*, 98(22):227801, 2007.

[60] Basile Pottier, Christian Frétigny, and L Talini. Boundary condition in liquid thin films revealed through the thermal fluctuations of their free surfaces. *Phys. Rev. Lett.*, 114(22):227801, 2015.

[61] Kyle J Alvine, Yeling Dai, Hyun W Ro, Suresh Narayanan, A. R Sandy, Christopher L Soles, and Oleg G Shpyrko. Capillary wave dynamics of thin polymer films over submerged nanostructures. *Phys. Rev. Lett.*, 109(20):207801, 2012.

[62] Mehran Kardar, Giorgio Parisi, and Yi-Cheng Zhang. Dynamic scaling of growing interfaces. *Phys. Rev. Lett.*, 56(9):889, 1986.

[63] A-L Barabási and Harry Eugene Stanley. *Fractal Concepts in Surface Growth*. Cambridge University Press, 1995.

[64] Yixin Zhang, James E Sprittles, and Duncan A Lockerby. Molecular simulation of thin liquid films: Thermal fluctuations and instability. *Phys. Rev. E*, 100(2):023108, 2019.

[65] Shuyu Chen, Han Wang, Tiezheng Qian, and Ping Sheng. Determining hydrodynamic boundary conditions from equilibrium fluctuations. *Phys. Rev. E*, 92(4):043007, 2015.

[66] Andreas Münch, BA Wagner, and Thomas P Witelski. Lubrication models with small to large slip lengths. *J. Eng. Math.*, 53(3-4):359–383, 2005.

[67] David M Huang, Christian Sendner, Dominik Horinek, Roland R Netz, and Lydéric Bocquet. Water slippage versus contact angle: A quasiuniversal relationship. *Phys. Rev. Lett.*, 101(22):226101, 2008.

[68] Peter A Thompson and Sandra M Troian. A general boundary condition for liquid flow at solid surfaces. *Nature*, 389(6649):360–362, 1997.

[69] Lydéric Bocquet and Jean-Louis Barrat. Hydrodynamic boundary conditions, correlation functions, and kubo relations for confined fluids. *Phys. Rev. E*, 49(4):3079, 1994.

[70] Bladimir Ramos-Alvarado, Satish Kumar, and GP Peterson. Hydrodynamic slip length as a surface property. *Phys. Rev. E*, 93(2):023101, 2016.

[71] Eric Lauga, Michael P Brenner, and Howard A Stone. Microfluidics: the no-slip boundary condition. *arXiv preprint cond-mat/0501557*, 2005.

[72] J-T Cheng and N Giordano. Fluid flow through nanometer-scale channels. *Phys. Rev. E*, 65(3):031206, 2002.

[73] Derek YC Chan and RG Horn. The drainage of thin liquid films between solid surfaces. *J. Chem. Phys.*, 83(10):5311–5324, 1985.

[74] Yingxi Zhu and Steve Granick. No-slip boundary condition switches to partial slip when fluid contains surfactant. *Langmuir*, 18(26):10058–10063, 2002.

[75] Vincent SJ Craig, Chiara Neto, and David RM Williams. Shear-dependent boundary slip in an aqueous newtonian liquid. *Phys. Rev. Lett.*, 87(5):054504, 2001.

[76] Pierre Joseph and Patrick Tabeling. Direct measurement of the apparent slip length. *Phys. Rev. E*, 71(3):035303, 2005.

[77] R Pit, H Hervet, and L Leger. Direct experimental evidence of slip in hexadecane: solid interfaces. *Phys. Rev. Lett.*, 85(5):980, 2000.

[78] L Joly, C Ybert, and Lyderic Bocquet. Probing the nanohydrodynamics at liquid-solid interfaces using thermal motion. *Phys. Rev. Lett.*, 96(4):046101, 2006.

[79] A Busse and ND Sandham. Influence of an anisotropic slip-length boundary condition on turbulent channel flow. *Phys. Fluids*, 24(5):055111, 2012.

[80] B Woolford, J Prince, D Maynes, and BW Webb. Particle image velocimetry characterization of turbulent channel flow with rib patterned superhydrophobic walls. *Phys. Fluids*, 21(8):085106, 2009.

[81] Koji Fukagata, Nobuhide Kasagi, and Petros Koumoutsakos. A theoretical prediction of friction drag reduction in turbulent flow by superhydrophobic surfaces. *Phys. Fluids*, 18(5):051703, 2006.

[82] Jose M Ortiz De Zarate and Jan V Sengers. *Hydrodynamic fluctuations in fluids and fluid mixtures*. Elsevier, 2006.

[83] D Bedeaux, AM Albano, and P Mazur. Brownian motion and fluctuating hydrodynamics ii; a fluctuation-dissipation theorem for the slip coefficient. *Physica A*, 88(3):574–582, 1977.

[84] Svetozar Nesic, Rodolfo Cuerno, Esteban Moro, and Lou Kondic. Dynamics of thin fluid films controlled by thermal fluctuations. *Eur. Phys. J. Spec. Top.*, 224(2):379–387, 2015.

[85] Yu L Klimontovich. Ito, stratonovich and kinetic forms of stochastic equations. *Physica A*, 163(2):515–532, 1990.

[86] Markus Hütter and Hans Christian Öttinger. Fluctuation-dissipation theorem, kinetic stochastic integral and efficient simulations. *J. Chem. Soc., Faraday Trans.*, 94(10):1403–1405, 1998.

[87] Bernt Oksendal. *Stochastic differential equations: an introduction with applications*. Springer Science & Business Media, 2013.

[88] Scott W Sides, Gary S Grest, and Martin-D Lacasse. Capillary waves at liquid-vapor interfaces: A molecular dynamics simulation. *Phys. Rev. E*, 60(6):6708, 1999.

[89] Luis G MacDowell. Capillary wave theory of adsorbed liquid films and the structure of the liquid-vapor interface. *Phys. Rev. E*, 96(2):022801, 2017.

[90] Yixin Zhang, James E Sprittles, and Duncan A Lockerby. Nanoscale thin-film flows with thermal fluctuations and slip. *Phys. Rev. E*, 102(5):053105, 2020.

[91] Thomas Erneux and Stephen H Davis. Nonlinear rupture of free films. *Phys. Fluids*, 5(5):1117–1122, 1993.

[92] Michael P Allen and Dominic J Tildesley. *Computer simulation of liquids*. Oxford university press, 2017.

[93] Dennis C Rapaport. *The art of molecular dynamics simulation*. Cambridge university press, 2004.

[94] Steve Plimpton. Fast parallel algorithms for short-range molecular dynamics. *J. Comput. Phys.*, 117(1):1–19, 1995.

[95] Andrij Trokhymchuk and José Alejandre. Computer simulations of liquid/vapor interface in lennard-jones fluids: Some questions and answers. *J. Chem. Phys.*, 111(18):8510–8523, 1999.

[96] Hans C Andersen. Molecular dynamics simulations at constant pressure and/or temperature. *J. Chem. Phys.*, 72(4):2384–2393, 1980.

[97] Herman JC Berendsen, JPM van Postma, Wilfred F van Gunsteren, ARHJ DiNola, and Jan R Haak. Molecular dynamics with coupling to an external bath. *J. Chem. Phys.*, 81(8):3684–3690, 1984.

[98] Shuichi Nosé. A unified formulation of the constant temperature molecular dynamics methods. *J. Chem. Phys.*, 81(1):511–519, 1984.

[99] William G Hoover. Canonical dynamics: Equilibrium phase-space distributions. *Physical review A*, 31(3):1695, 1985.

[100] Berk Hess. Determining the shear viscosity of model liquids from molecular dynamics simulations. *J. Chem. Phys.*, 116(1):209–217, 2002.

[101] Andrij Trokhymchuk and José Alejandre. Computer simulations of liquid/vapor interface in lennard-jones fluids: Some questions and answers. *J. Chem. Phys.*, 111(18):8510–8523, 1999.

[102] CY Soong, TH Yen, and PY Tzeng. Molecular dynamics simulation of nanochannel flows with effects of wall lattice-fluid interactions. *Phys. Rev. E*, 76(3):036303, 2007.

[103] Jacob N Israelachvili. *Intermolecular and Surface Forces*. Academic press, 2011.

[104] Thomas P Witelski and Andrew J Bernoff. Dynamics of three-dimensional thin film rupture. *Physica D*, 147(1-2):155–176, 2000.

[105] Hangjie Ji and Thomas P Witelski. Finite-time thin film rupture driven by modified evaporative loss. *Physica D*, 342:1–15, 2017.

[106] Eli Ruckenstein and Rakesh K Jain. Spontaneous rupture of thin liquid films. *J. Chem. Soc. Faraday Trans.*, 70:132–147, 1974.

[107] Joel Koplik and Jayanth R Banavar. Molecular simulations of dewetting. *Phys. Rev. Lett.*, 84(19):4401, 2000.

[108] Yutaka Yamada, Kanoko Taguchi, Tatsuya Ikuta, Akihiko Horibe, and Koji Takahashi. Meniscus motion and void generation inside carbon nanotubes. *J. Phy. Chem. C*, 122(38):21910–21918, 2018.

[109] Adi Constantinescu, Leonardo Golubović, and Artem Levandovsky. Beyond the young-laplace model for cluster growth during dewetting of thin films: Effective coarsening exponents and the role of long range dewetting interactions. *Phys. Rev. E*, 88(3):032113, 2013.

[110] Karl B Glasner and Thomas P Witelski. Coarsening dynamics of dewetting films. *Phys. Rev. E*, 67(1):016302, 2003.

[111] AM Willis and JB Freund. Thermal capillary waves relaxing on atomically thin liquid films. *Phys. Fluids*, 22(2):022002, 2010.

[112] Eirik G Flekkøy and Daniel H Rothman. Fluctuating fluid interfaces. *Phys. Rev. Lett.*, 75(2):260, 1995.

[113] Renate Fetzer, K Jacobs, A Münch, B Wagner, and T. P Witelski. New slip regimes and the shape of dewetting thin liquid films. *Phys. Rev. Lett*, 95(12):127801, 2005.

[114] Oliver Bäumchen, Ludovic Marquant, Ralf Blossey, Andreas Münch, Barbara Wagner, and Karin Jacobs. Influence of slip on the rayleigh-plateau rim instability in dewetting viscous films. *Phys. Rev. Lett.*, 113(1):014501, 2014.

[115] A Vrij and J Th G Overbeek. Rupture of thin liquid films due to spontaneous fluctuations in thickness. *J. Am. Chem. Soc.*, 90(12):3074–3078, 1968.

[116] Sridhar Kumar Kannam, BD Todd, Jesper Schmidt Hansen, and Peter J Daivis. Slip length of water on graphene: Limitations of non-equilibrium molecular dynamics simulations. *J. Chem. Phys.*, 136(2):024705, 2012.

[117] Olivier Pierre-Louis. Thermal fluctuations of a liquid film on a heterogeneous solid substrate. *Phys. Rev. E*, 94(3):032802, 2016.

[118] Kajari Kargupta, Ashutosh Sharma, and Rajesh Khanna. Instability, dynamics, and morphology of thin slipping films. *Langmuir*, 20(1):244–253, 2004.

[119] Chengxi Zhao, Duncan A Lockerby, and James E Sprittles. Dynamics of liquid nanothreads: Fluctuation-driven instability and rupture. *Phys. Rev. Fluids*, 5(4):044201, 2020.

[120] Wendy W Zhang and John R Lister. Similarity solutions for van der waals rupture of a thin film on a solid substrate. *Phys. Fluids*, 11(9):2454–2462, 1999.

[121] EH Hauge and A Martin-Löf. Fluctuating hydrodynamics and brownian motion. *J. Stat. Phys.*, 7(3):259–281, 1973.

[122] Marine Thiébaud and Thomas Bickel. Nonequilibrium fluctuations of an interface under shear. *Phys. Rev. E*, 81(3):031602, 2010.

[123] Martin Grant and Rashmi C Desai. Fluctuating hydrodynamics and capillary waves. *Phys. Rev. A*, 27(5):2577, 1983.